USGS
science for a changing world

Infiltration and Runoff Measurements on Steep Burned Hillslopes Using a Rainfall Simulator with Variable Rain Intensities

Scientific Investigations Report 2007–5211

U.S. Department of the Interior
U.S. Geological Survey

Infiltration and Runoff Measurements on Steep Burned Hillslopes Using a Rainfall Simulator with Variable Rain Intensities

By David A. Kinner and John A. Moody

Scientific Investigations Report 2007–5211

U.S. Department of the Interior
U.S. Geological Survey

U.S. Department of the Interior
DIRK KEMPTHORNE, Secretary

U.S. Geological Survey
Mark D. Myers, Director

U.S. Geological Survey, Reston, Virginia: 2008

About USGS Products

For product and ordering information:
World Wide Web: http://www.usgs.gov/pubprod
Telephone: 1-888-ASK-USGS

For more information on the USGS—the Federal source for science about the Earth, its natural and living resources, natural hazards, and the environment:
World Wide Web: http://www.usgs.gov
Telephone: 1-888-ASK-USGS

About this Product

For more information concerning this publication, contact:
Team Chief Scientist, USGS Central Region Geologic Hazards Team
Box 25046
Denver Federal Center
MS 966
Denver, CO 80225-0046
(303) 273-8579
Or visit the Central Region Geologic Hazards Team Web site at:
http://geohazards.cr.usgs.gov

This publication is available online at:
http://pubs.usgs.gov/sir/2007/5211/

Publishing support provided by:
Denver Publishing Service Center, Denver, Colorado
Manuscript approved for publication, August 2007
Edited by Mary Kidd
Layout by Margo VanAlstine

Suggested citation:
Kinner, D.A., and Moody, J.A., 2008, Infiltration and runoff measurements on steep burned hillslopes using a rainfall simulator with variable rain intensities: U.S. Geological Survey Scientific Investigations Report 2007–5211, 64 p.; available online only.

Contents

Figures

Tables

Conversion Factors

Multiply	By	To obtain
	Length	
centimeter (cm)	0.3937	inch (in.)
millimeter (mm)	0.03937	inch (in.)
meter (m)	3.281	foot (ft)
kilometer (km)	0.6214	mile (mi)
	Area	
hectare (ha)	2.471	acre
square meter (m^2)	10.76	square foot (ft^2)
square kilometer (km^2)	0.3861	square mile (mi^2)
	Volume	
liter (L)	0.2642	gallon (gal)
cubic centimeter (cm^3)	0.06102	cubic inch (in^3)
	Flow rate	
meter per second (m/s)	3.281	foot per second (ft/s)
liter per minute (L/m)	15.85	gallon per minute (gal/min) (GPM)
millimeter per hour (mm/h)	0.03937	inch per year (in/hr)
	Mass	
gram (g)	0.03527	ounce, avoirdupois (oz)
	Pressure	
kilopascal (kPa)	0.1450	pound per square inch (psi)
	Density	
kilogram per cubic meter (kg/m^3)	0.06242	pound per cubic foot (lb/ft^3)
gram per cubic centimeter (g/cm^3)	62.4220	pound per cubic foot (lb/ft^3)
	Energy	
joule (J)	0.0000002	kilowatthour (kWh)
	Energy per unit rainfall	
Megajoules per hectare per millimeter (MJ/ha/mm)	0.8921	foot ton-foot per acre per inch [(ft ton-foot/acre)/m]

Temperature in degrees Celsius (°C) may be converted to degrees Fahrenheit (°F) as follows:

$$°F=(1.8×°C)+32$$

Temperature in degrees Fahrenheit (°F) may be converted to degrees Celsius (°C) as follows:

$$°C=(°F–32)/1.8$$

Vertical coordinate information is referenced to the North American Vertical Datum of 1988 (NAVD 88).

Horizontal coordinate information is referenced to North American Datum of 1927 (NAD 27).

Altitude, as used in this report, refers to distance above the vertical datum.

Symbols, Abbreviations, and Acronyms

2DVD	two-dimensional video disdrometer
a	major axis length for an ellipsoid (m)
b	minor axis length for ellipsoid (m)
c	empirical constant for unit rainfall energy

C_{apron}	correction coefficient for collecting apron
CV	coefficient of variation (1 standard deviation)
CV_K	coefficient of variation of hydraulic conductivity
D	equivolumetric spherical diameter (m)
DEM	digital elevation model
DQ/dt	change in runoff with time
e	unit rainfall energy (MJ/ha/mm)
E_k	kinetic energy (MJ)
GG	FullJet® nozzle designation
GPM	gallons per minute
HP	horsepower
I	rainfall intensity (mm/h)
I*	normalized rain rate,
I_{BL}	rainfall intensity in the bottom left-hand small rain gage (mm/h)
I_{BR}	rainfall intensity in the bottom right-hand small rain gage (mm/h)
J	joules (kg ([m^2/sec^2])
K_e	effective hydraulic conductivity (mm/h)
LOI	lost on ignition (percent)
m_r	mass of raindrop (kg)
m_d	oven-dry soil mass (kg)
m_w	wet soil mass (kg)
N13	plot number, north side
p	empirical shape parameter in logarithmic distribution equation
R^2	correlation coefficient
S13	plot number, south side
SM	soil moisture (m^3/m^3)
v	velocity (m/s)
V	volume (m^3)
x	translated plot coordinate (m) to match those defined by plot boundaries
y	translated plot coordinate (m) to match those defined by plot boundaries
y_{min}	minimum y-coordinate for each plot (m)
z	elevation above the lowest point in the plot (m)
X, Y	rotated plot coordinate, which has the same orientation as the plot boundaries
X',Y'	plot coordinate measure by an electronic survey instrument in an arbitrary coordinate system
Z	elevation in the arbitrary coordinate system
α	statistical significance level
ρ_w	density of water (kg/m^3)
π	constant pi
ε_K	expected or mean saturated hydraulic conductivity (mm/h)
λ	empirical constant for unit rainfall energy (h/mm)

Infiltration and Runoff Measurements on Steep Burned Hillslopes Using a Rainfall Simulator with Variable Rain Intensities

By David A. Kinner and John A. Moody

Abstract

Multiple rainfall intensities were used in rainfall-simulation experiments designed to investigate the infiltration and runoff from 1-square-meter plots on burned hillslopes covered by an ash layer of varying thickness. The 1-square-meter plots were on north- and south-facing hillslopes in an area burned by the Overland fire northwest of Boulder near Jamestown on the Front Range of Colorado. A single-nozzle, wide-angle, multi-intensity rain simulator was developed to investigate the infiltration and runoff on steep (30- to 40-percent gradient) burned hillslopes covered with ash. The simulated rainfall was evaluated for spatial variability, drop size, and kinetic energy. Fourteen rainfall simulations, at three intensities (about 20 millimeters per hour [mm/h], 35 mm/h, and 50 mm/h), were conducted on four plots. Measurements during and after the simulations included runoff, rainfall, suspended-sediment concentrations, surface ash layer thickness, soil moisture, soil grain size, soil lost on ignition, and plot topography.

Runoff discharge reached a steady state within 7 to 26 minutes. Steady infiltration rates with the 50-mm/h application rainfall intensity approached 20–35 mm/h. If these rates are projected to rainfall application intensities used in many studies of burned area runoff production (about 80 mm/h), the steady discharge rates are on the lower end of measurements from other studies. Experiments using multiple rainfall intensities (three) suggest that runoff begins at rainfall intensities around 20 mm/h at the 1-square-meter scale, an observation consistent with a 10-mm/h rainfall intensity threshold needed for runoff initiation that has been reported in the literature.

Introduction

Runoff from Burned Watersheds

Several postfire hazards can result from burning forests and grasslands in the Western United States. These include floods (Krammes and Rice, 1963; Bolin and Ward, 1987; Moody and Martin, 2001a,b; Veenhuis, 2002), erosion (Moody and Martin, 2001a,b), increased sediment transport (Moody and Martin, 2001a,b); and debris flows (Eaton, 1935; Wohl and Pearthree, 1991; Parrett, 1987; Cannon, 2001; Parrett and others, 2003; Cannon and Gartner, 2005) at the basin scale. These basin-scale hazards (Cannon and others, 2003) integrate several hillslope-scale hydrologic processes including canopy interception, storage of rainfall in the litter and duff, infiltration, and overland flow. Thus, to adequately predict these hazards at larger scales in physical models, the processes must be examined at the hillslope scale to identify the essential variables and the relative magnitude of each runoff generation process. Some of the possible variables are the rainfall characteristics such as intensity, kinetic energy, and hydrologic thresholds that must be exceeded to generate a runoff response. Additional variables are the hillslope aspect and the thickness and hydraulic properties of the ash layer left after a fire.

A rainfall intensity threshold appears to control runoff generation in burned areas. Peak discharges and runoff totals increase more rapidly when the 30-minute maximum rainfall intensities exceed a threshold of about 10 mm/h. This threshold appears to be applicable to several sites (Moody and Martin, 2001a; Kunze and Stednick, 2006) so that the question is whether the threshold is related to the variability in infiltration excess overland-flow production on hillslopes or related to the establishment of networks of flow paths along hillslope. Many postfire experiments (Cerdà, 1998; Robichaud, 2000; Pierson and others, 2001; Benavides-Solorio and MacDonald, 2001) on burned plots used one rainfall intensity on the order of 80 mm/h and therefore results could not be used to determine runoff initiation thresholds. Moreover, Dunne and Dietrich (1980) emphasize that several rainfall intensities are necessary to verify the partial contributing area concept of Betson (1964).

Hillslope aspect determines major difference in soil development between different aspects (Birkeland and others, 2003). Clay-rich horizons can develop on north-facing slopes (Birkeland and others, 2003, their figure 7) and these

generally have deeper soils and are wetter later into the spring than south-facing slopes. However, south-facing slopes commonly produce more runoff from snowmelt and undergo more freeze/thaw weathering cycles during the winter than north-facing slopes.

The presence of an ash layer is an additional variable in postfire runoff generation. Ash is used colloquially throughout this report to mean the burned organic matter of varied sizes that can include charred material, charcoal, and mineral material. Mineral fragments may be incorporated into the burned organic matter by winds driving a fire and winds generated by the fire itself. Some of these ash particles may contribute to surface sealing if rainfall kinetic energy is sufficient to force ash and soil into soil pores (Rowe, 1948; Imeson and others, 1992; Neary and others, 1999). Surface sealing has been documented for fine soils in agricultural regions (Dunne and Dietrich, 1980; Römkens and others, 1990; Sumner and Stewart, 1992) but has not been identified specifically in burned areas. Moreover, the ash layer overlying a coarse soil may form a capillary barrier (Ross, 1990; Lu and Likos, 2004) that keeps the underlying soil from wetting during rain and snowstorms (Jonathan Godt, U.S. Geological Survey, written commun., 2004).

Purpose and Scope of Study

Experiments were designed to determine the effects of four different variables on rainfall-runoff relations for 1-m^2 plot on burned hillslopes. The four different variables are (1) hillslope aspects, (2) ash thickness, (3) ash texture, and (4) flow-path structure. We describe a rainfall simulator that was designed to control the rainfall intensity (20 to 50 mm/h) applied to the plots in order to investigate the effect of the different variables on infiltration and runoff from burned hillslopes. Data collected from 14 rainfall simulation experiments are presented and discussed in this report. Additional hillslope characteristics were measured so that the results can be generalized to larger areas. The experiments were completed during the summer and fall of 2004 in an area that was classified as having burned at medium to high intensity during the 2003 Overland fire near Jamestown, Colorado.

Research Site

The Overland fire burned 15,566 ha during a single day in the fall of 2003. It started on October 29, 2003, in Jamestown, Colorado, and, spurred by winds, moved eastward about 10 km. A rain-snow storm extinguished the fire by the second day, and the storm essentially preserved the ash layer. This permitted a unique situation where rainfall experiments could be carried out under conditions equivalent to the first postfire rainfall. Postfire qualitative assessments by the USDA Forest Service indicated that the burned area was a mosaic pattern with low to high soil-burn severity (Eric Schroder, USDA Forest Service, written commun., 2004; fig. 1).

The location of the research site was based on three criteria. First, the site was within a burned area that was designated as high to moderate soil-burn severity (fig. 1). This criterion was designed to control the soil-burn-severity variable and to understand the infiltration and runoff processes under the most severe change in soil properties. Second, the ash layer needed to be present at the soil surface so we could examine its effect on the infiltration. This ash layer, unlike ash layers that are produced during many summer fires, was preserved during the winter by the snow cover and freezing temperatures that followed the fire. Some wind transport of the ash was observed in the spring, but tarps were placed over the prospective plots, and water was diverted from flowing across the plots to preserve the immediate postfire conditions. Third, the experimental plots needed to be near a road (about 100 m), so we could use the rainfall simulator.

The selected site had both north- and south-facing slopes. It was adjacent to Forest Service road 284.1 in the Roosevelt National Forest (southwest quarter of sec. 17, T. 2 N., R. 71 W.) and at elevations ranging from 2,320 to 2,380 m (fig. 1). Vegetation varied on the north-facing slope from aspens (*Populus tremuloides*) at the base of the slope to Douglas firs (*Pseudotsuga menziesii*) nearer to the ridge crest, and ponderosa pine (*Pinus ponderosa*) was predominant on the south-facing slope. The geology was Precambrian pegmatite on ridges, Silver Plume Quartz Monzonite on side slopes, and colluvium in the stream valleys (Brandt and others, 2003). Areas near the site had been mined historically, but no mine disturbance was visible on either the north- or south-facing study areas. Evidence of historical mining appeared at the ridge just above and outside of the north-facing study area, but drainage from this disturbed area had been diverted around the north-facing plot boundaries. The south-facing slope also had a large rock outcrop that acted as a source area for overland flow and rill initiation.

Methods

Types of Rainfall Simulators

Rainfall simulators can be classified as either a nozzle-type or a drip-type system. In a drip-type system, drop formers (or capillaries) and a reservoir pressure head generate drops (McQueen, 1963; Kamphorst, 1987). The drip-type system described by McQueen (1963) included unique, custom-built components. The drip-type system is limited by the constant raindrop size, drops hitting the same location of the soil surface, and a small infiltration area (0.017 m^2). In a nozzle-type system, a pump pushes water through a nozzle or a series of nozzles to form a spray. Some nozzle-type systems have a single nozzle and a pump (Cerdà and others, 1997; Wilcox and others, 1986), some use multiple nozzles (Dunne and

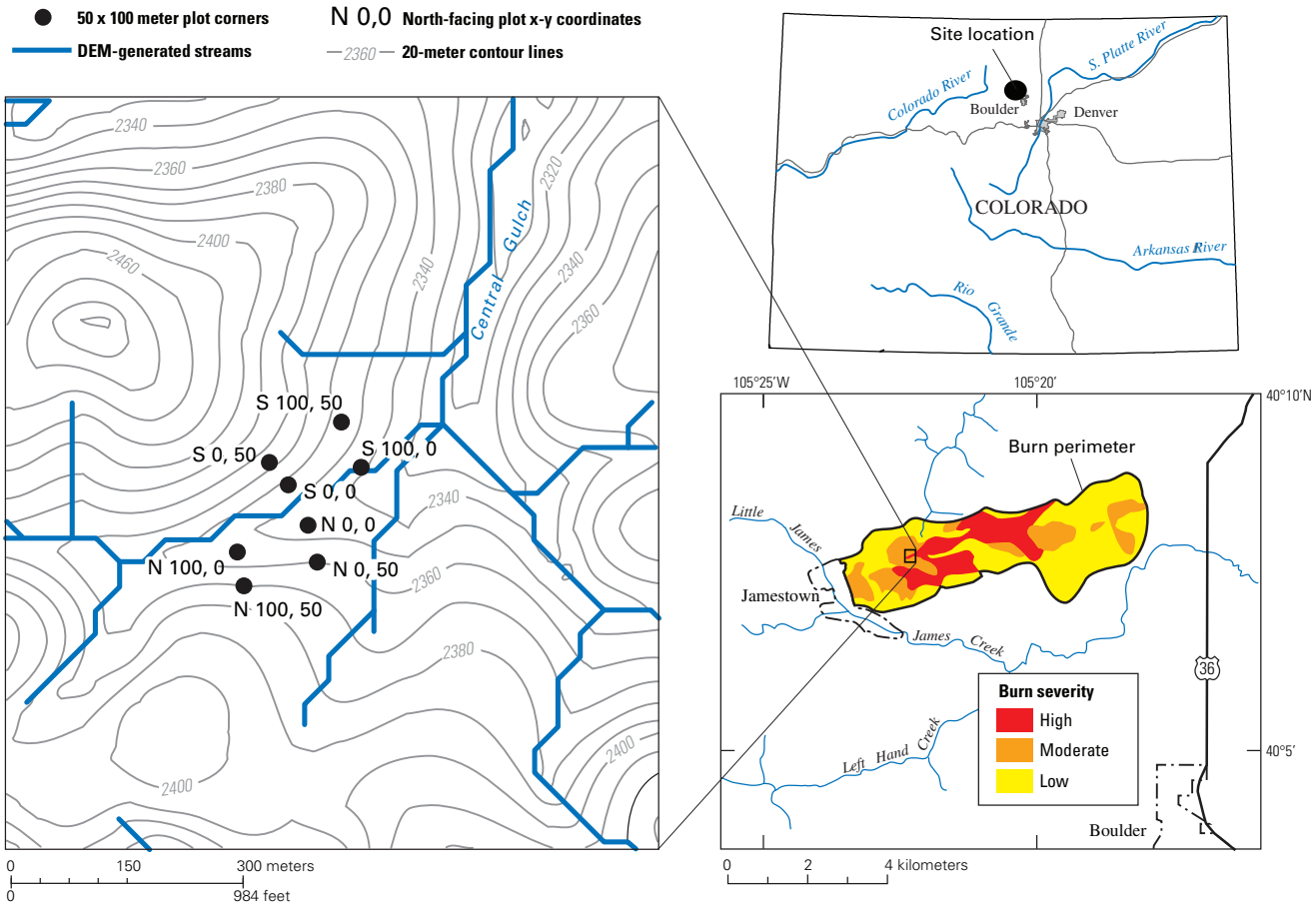

Figure 1. Site showing location of major drainages, and qualitative burn severity of the 2003 Overland fire as defined by the USDA Forest Service. DEM, digital elevation model.

others, 1991), and some use oscillating and programmable nozzles (Paige and others, 2003; Niebling and others, 1981). The single-nozzle type of rainfall simulator typically applies a continuous spray on a plot and has very few movable parts. The oscillating type can produce desired rainfall intensities by altering the amount of time a constant flux of water is actually applied to the soil surface (Meyer and Harmon, 1979). Many rainfall simulators have been used to assess runoff and erosion on rangeland (Ward and Bolton, 1991; Wilcox and others, 1986), agricultural lands (Meyer and Harmon, 1979; Niebling and others, 1981), and burned watersheds (Cerdà, 1998; Robichaud, 2000; Martin and Moody, 2001; Pierson and others, 2001; Benavides-Solorio and MacDonald, 2001).

Rainfall Simulator Design

The rainfall simulator was designed to meet five criteria. The first criterion was that it be possible to transport the simulator up to 100 m from a vehicle, in steep terrain, and maintain flow pressure over that distance and elevation. Second, the height of the nozzle had to be adjustable. Third, the simulator should have a windscreen. Fourth, it should be portable because many of the roads that we planned to use for site access were rugged and passable only by a relatively small vehicle that also would be transporting water needed for the simulations. Fifth, and most important, the simulator should be capable of producing multiple rainfall intensities. As Dunne and Dietrich (1980) and Paige and others (2003) have pointed out, changing the rainfall intensity alters the area contributing to plot runoff because contributing area can increase with increasing rainfall intensity. The relation between contributing area and runoff is critical for understanding hydraulic variability in the field (Smith and Goodrich, 2000) and likely leads to nonlinear runoff responses to rainfall at watershed scale (Betson, 1964; Smith and Goodrich, 2000).

The rain simulator had a tripod frame to hold different nozzles at a fixed height above the soil surface. The design (fig. 2) had fewer parts to assemble in the field than would a programmable simulator. The water-supply system provided a constant flux of water at pressures from 35 to 275 kPa (5 to 40 psi) up steep hillslopes, thus providing constant rainfall intensity. A 195-gallon polyethylene tank was mounted on a pickup truck with a submersible well pump (Red Jacket Enduro, 12 gallons per minute, 0.5 horsepower). The pump was powered by a generator (5,500-watt Honda) and had a low-water shut-off switch. A valve shunt at the pump (fig. 2)

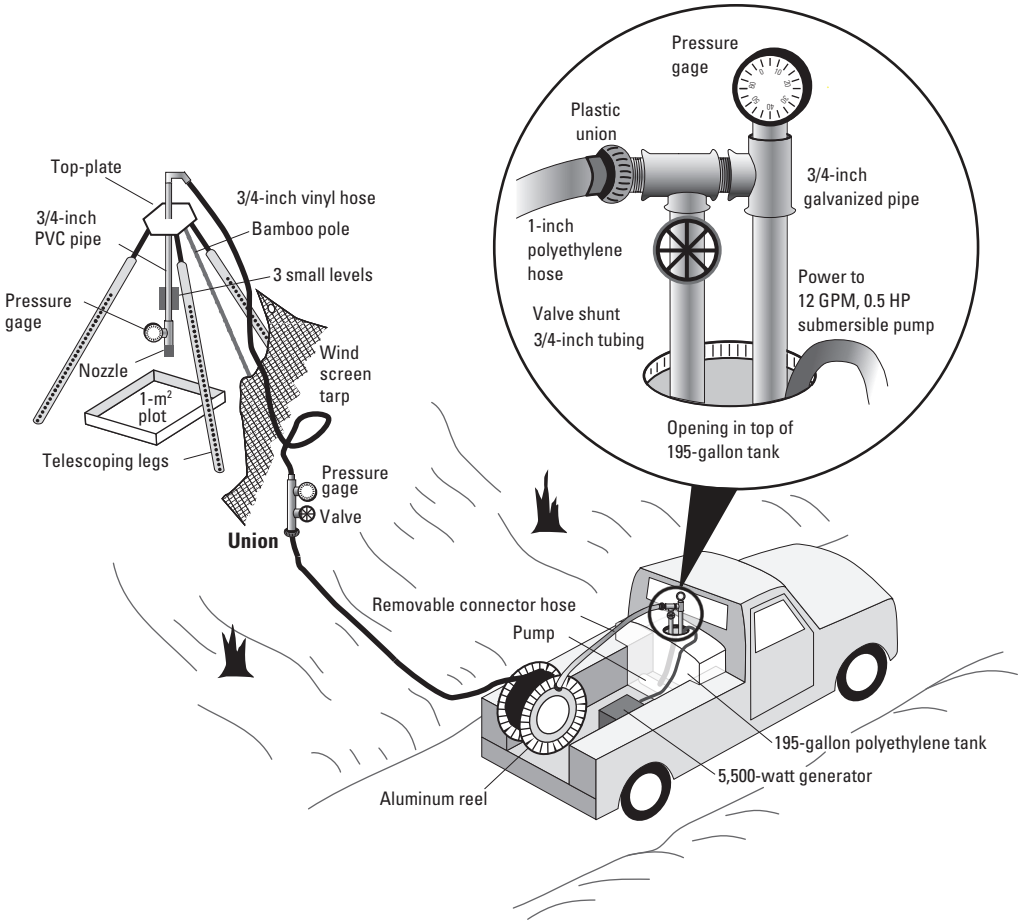

Figure 2. Schematic diagram of the setup of the rainfall simulator described in this report. GPM, gallons per minute; PVC, polyvinyl chloride; m^2, square meter; HP, horsepower.

could be adjusted to reduce the pressure by diverting more water back into the tank. The pump was attached to the hose on an aluminum reel by a removable connector hose with unions. The aluminum reel held nearly 100 m of 1-inch polyethylene hose, which had little friction loss such that most of the pressure loss was due to head loss between the vehicle and the nozzle. Pressures were measured at the tank on the truck, at the tripod where the polyethylene hose was attached to a more flexible vinyl hose, and at the nozzle.

Several nozzles produced variable combinations of rainfall intensity and kinetic energy. Each nozzle was mounted in a ¾-inch T-fitting (with pressure gage) attached to the bottom of ¾-inch PVC (polyvinyl chloride) pipe that hung vertically from the center of a hexagonal aluminum top-plate of the tripod (fig. 2). The top of the PVC pipe had fittings that connected the pipe to a 25-foot-long, ¾-inch-diameter vinyl hose. The PVC pipe could be raised or lowered to the desired height above the plot and was held vertically by three adjustable lines running from just above the nozzle to each of the tripod legs. Three levels were mounted on the PVC pipe just above the nozzle to aid in plumbing the PVC pipe. The tripod had telescoping legs attached to the hexagonal top-plate to facilitate positioning the nozzle vertically over the center of the plot on irregularly steep hillslope. The hexagonal top-plate had notches on the sides between the telescoping legs for bamboo poles that helped to support a tarp, which enclosed the tripod and acted as a windscreen. The nozzles were Spraying System FullJet® nozzles. Similar nozzles have been used in western Colorado (John Elliott, U.S. Geological Survey, oral commun., 2004) and in New Mexico (Wilcox and others, 1986).

Simulated Rainfall Calibration and Evaluation

Four procedures were used in the laboratory and in the field to evaluate the rainfall simulator. Two procedures in the laboratory measured (1) the temporally averaged rainfall intensity and the spatial variability of these intensities on a level surface, and (2) the velocities and drop sizes for different nozzle and pressure combinations using a two-dimensional video disdrometer (2DVD). Two procedures in the field measured (1) the temporally averaged spatial variability of the rainfall on a sloping surface, and (2) the temporal variability of the rainfall. This section describes these procedures.

The first laboratory procedure used an x-shaped array of 45 small rain gages (opening 2.2 mm by 4.0 mm) to measure temporally averaged rainfall intensity and spatial variability of the rainfall intensity on a level surface. The array (fig. 3) was centered 1.4 m directly beneath the nozzle and was run for at least one-half hour or until one of the small rain gages appeared full (about 120 mm). We tested a set of Spraying Systems FullJet® nozzles to identify those that could be used in the field.

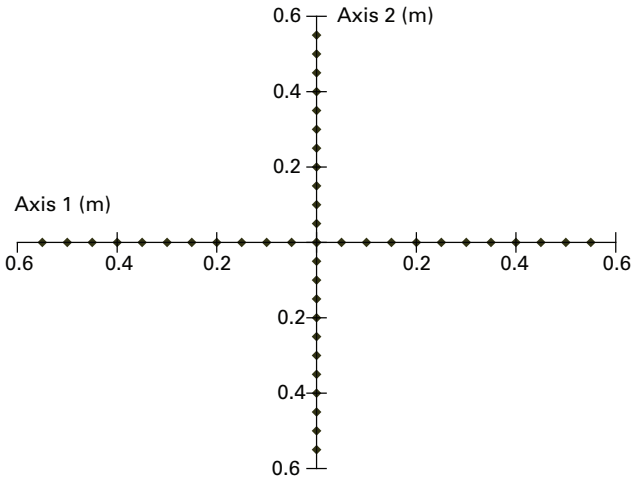

Figure 3. Diagram of the rain-gage sampling array used to test spatial variability of rainfall on a level surface. m, meter.

The second laboratory procedure used a two-dimensional video disdrometer (2DVD) to measure drop sizes and drop velocities. The disdrometer consists of two cameras mounted 6.2 mm apart vertically and oriented orthogonally, allowing the measurement of the three-dimensional raindrop geometry (Kruger and Krajewski, 2002). Because the cameras have a vertical offset, they also provide a measurement of the vertical velocity. The cameras also can be used to estimate raindrop oblateness (ratio of height to width of a raindrop) and the equivolumetric spherical diameter, D, of a raindrop (Kruger and Krajewski, 2002). Assuming that the shape of a raindrop is an oblate spheroid (ellipse of revolution) and its density, ρ_w, is that of water (1,000 kg/m^3) then the mass, m_r (kg), of a raindrop can be calculated from the volume, V (m^3) of an oblate spheroid:

$$m_r = \rho_w V = \rho_w \frac{4}{3} \pi(\frac{D}{2})^3 = \rho_w \frac{4}{3} \pi a^2 b \quad (1)$$

where a (cm) and b (cm) are the major and minor semiaxes of an ellipse and correspond respectively to one-half the width and height of a raindrop so that the oblateness is b/a and the equivolumetric diameter is

$$D = 2(a^2 b)^{1/3} \quad (2)$$

For a sphere, a equals b so that $D=2a=2b$ and the oblateness is 1. Measured disdrometer velocities and the computed masses can then be used to compute the kinetic energy, E_K, of rainfall in joules (J) with:

$$E_K = 0.5mv^2 \quad (3)$$

where v is raindrop velocity (m/s). Given a rainfall intensity, empirical equations have been used to estimate the unit rainfall energy, e (MJ/ha/mm), which is the kinetic energy per unit surface area per unit depth of rainfall. Brown and Foster (1987) present such an equation:

$$e = e_m(1 - ce^{(-\lambda * I)}) \quad (4)$$

where $e_m = 0.9$ MJ/ha/mm is the maximum unit rainfall energy as the intensity approaches infinity, I is the rainfall intensity in millimters per hour, and the empirical coefficients are $c = 0.72$ and $\lambda = 0.05$ h/mm. The disdrometer was placed 1.4 m below the center of the nozzle and offset by 0.5 m from this point. The offset was used to measure the variability caused by nozzle position relative to plot location.

The third procedure measured the rainfall intensities during a series of the 14 field experiments and during some special calibration experiments. Recording tipping-bucket rain gages (either one or three Onset Model SR–2 gages) were placed outside the y-axis of the plot (fig. 4). Special calibration experiments in the field measured the rainfall intensities on the plots. During these four special sheet calibration experiments on plot N15 (1 experiment per nozzle and pressure combination), a plastic sheet (zero infiltration) covered the entire plot surface, so runoff from the sheet represents integrated rainfall-intensity over a single 1-m^2 plot. Runoff was collected from this "zero-infiltration" plot at 0.5- or 1-minute intervals until steady-state runoff was reached and then for an additional 7 to 8 minutes. The average runoff per minute was converted to integrated rainfall intensity on a horizontal surface by dividing by the cosine of the slope of the plot. Simultane-

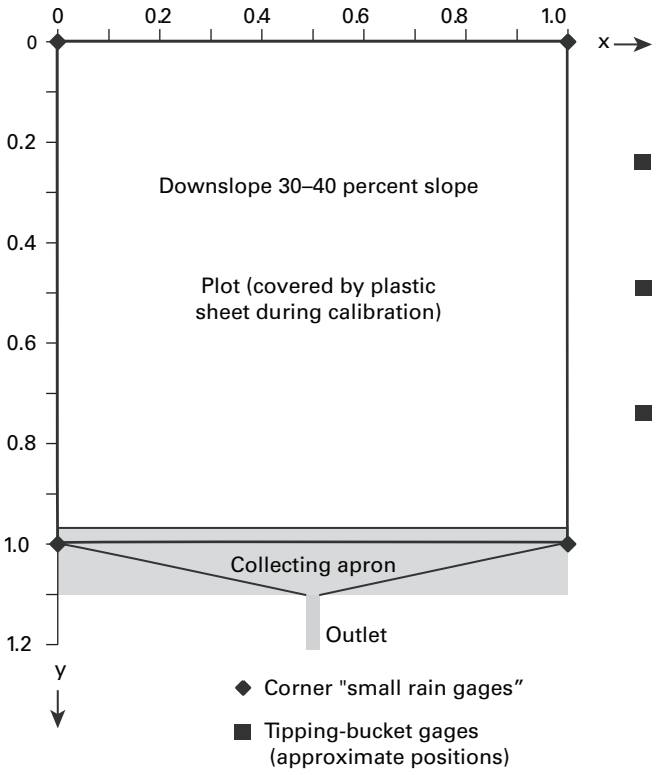

Figure 4. Diagram of plot layout on slopes showing the position of tipping-bucket and small rain gages.

ously, variable rain intensities were measured by the array of tipping-bucket rain gages at the edge of the plot (fig. 4). These measurements permitted the integrated rainfall intensity on the plot to be compared to the rainfall measured by the tipping-bucket rain gages outside the plot.

The fourth procedure measured the temporal variability of rainfall intensity. The 14 rainfall simulation experiments used the array of tipping buckets along one edge of the plot to record time-variable rainfall intensities and four small rain gages in the plot corners to measure the rainfall totals (fig. 4). For experiments 1–6, a single tipping-bucket rain gage was installed on the plot edge, but three tipping-bucket rain gages were deployed for experiments 7–14 after we realized the importance of spatial rainfall variability on a sloping surface. For the experiments with three tipping-bucket rain gages (7–14), the totals for each 2-minute interval were averaged. Then, least-linear-square regression techniques and F-tests determined if tipping-bucket data aggregated at 2-minute intervals changed significantly during each of the 14 experiments.

A second analysis of the temporal variability used the 2DVD disdrometer to measure the variability in the rainfall intensity over short times (15-second intervals) and over a small area (an approximately 0.01 m by 0.01 m window). We used a similar least-linear-square technique to analyze these data.

Study Area Characteristics

We surveyed two hillslope study areas, one on the north-facing slope and one on the south-facing slope. These areas were 100 m by 50 m, had grid lines spaced 10 m apart, and defined 66 potential sampling points at the intersection of the grid lines (corners of these study areas are shown in fig. 2). Topographic measurements made along each of the six grid lines running across the hillslope defined the general slope and relief of the study areas (fig. 5). Soil samples collected at the intersection points of the grid lines (66 samples) on the north- and south-facing study areas were analyzed to define the large-

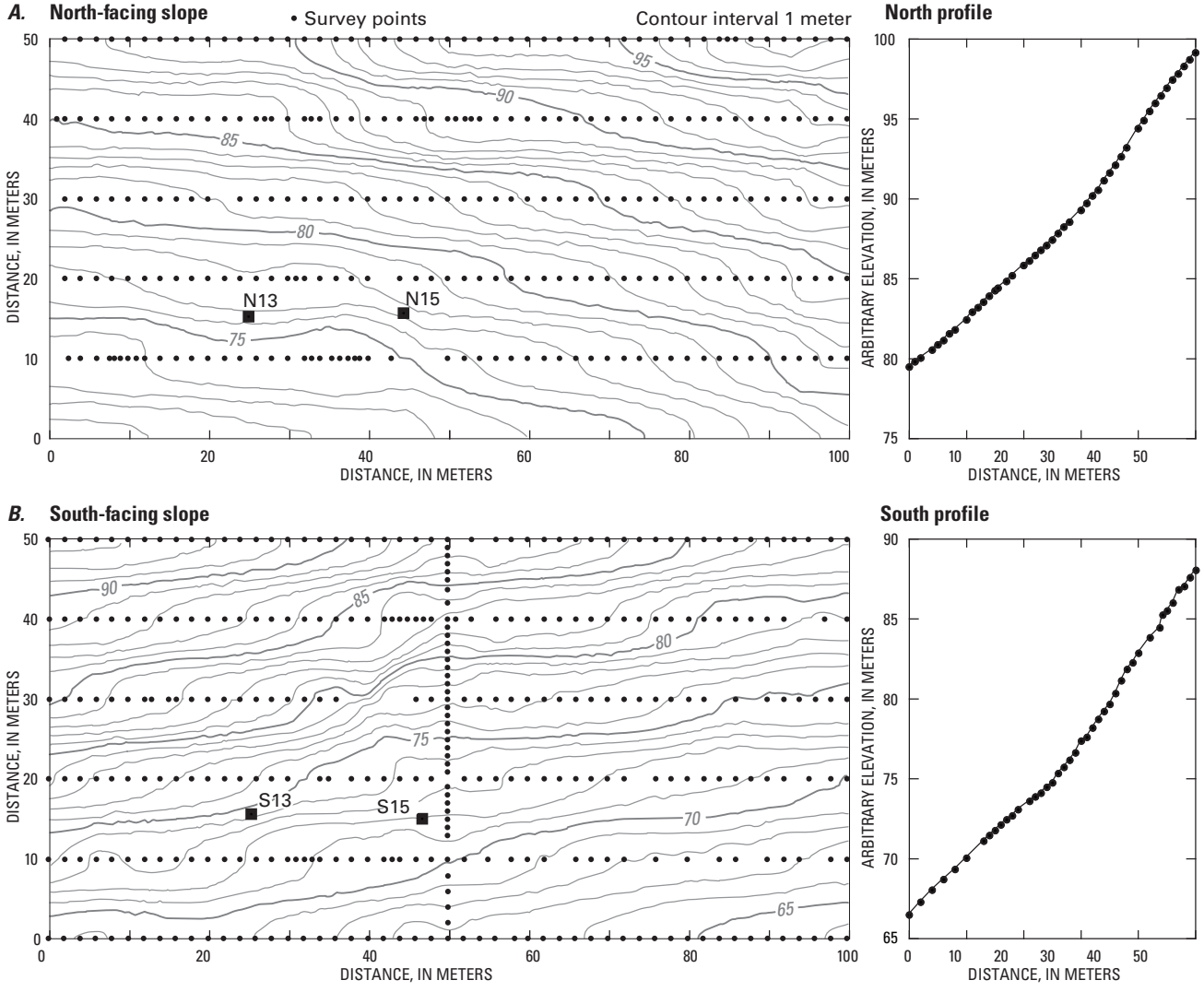

Figure 5. Contour map of (*A*) north- and (*B*) south-facing hillslopes and experimental plot locations.

scale (100 m^2) variability of soil properties. These soil samples were collected by using a 0.03-m-diameter soil core that was 0.03 m long. In some cases, soil samples were not collected because of bedrock outcrops at the intersection point. The particle-size distribution was determined for each sample (see methods described in "Plot Topography and Stratigraphy"), and the bulk density was measured for a subset of the samples. At each location, two observers estimated the percentage of bedrock (rocks larger than 0.05 m) within a 1-m^2 area centered at the intersection point. The reported value was the average of the two visual estimates. Additionally, at each intersection point, the thickness of the ash and thickness of any remaining litter and duff layer were measured.

Plot Experiments

Field runoff plots were randomly selected on north- and south-facing study areas in the spring of 2004. To maintain these conditions for later rainfall-simulation experiments, all the plots were covered with tarps, and metal edging was installed upslope from the plots to divert flow away from the plot. At the time of the installation, one major rainstorm on June 27, 2004, with a total rainfall of 19 mm (Colleen Williams, oral commun., 2005) generated overland flow and transported some sediment, so rills (about 0.10 m wide by about 0.05 m deep) were present on the south-facing slope. At that time, ash covered the surfaces. Plots S13 and S15 were 2 of 10 randomly chosen plot sites on the south-facing hillslope, and plots N13 and N15 were similar plots on the north-facing hillslope (fig. 5). These four plots were selected from a list of random plot sites on the basis of logistics and an attempt to identify plots that were representative of the hillslopes. An aluminum frame (about 0.1 m high) was installed on three sides of a plot, and the collecting apron was attached between the two downhill ends of the frame. The lip of the collecting apron protruded 0.0254 m into the plot, and silicon seal was used on the underside of this lip to connect the collecting apron to the soil and to prevent runoff from going under the collecting apron. A tarp was placed over the frame and collecting apron and was removed only when the steady rainfall intensity had been established.

Plot Topography and Stratigraphy

The plot topography and stratigraphy were measured after all the rainfall-simulation experiments were complete so that the surface was not disturbed. The plots were 0.975 m^2 in size (1 m^2 minus the area of the collecting apron lip), but because of the slope (N13=31 percent; N15=37 percent; S13=41 percent; S15=36 percent), the projected area on a horizontal surface intercepting incident rainfall was smaller than 0.975 m^2 (N13=0.93 m^2; N15=0.91 m^2; S13=0.90 m^2; S15=0.92 m^2). The origin of the coordinate system for each plot was in the upper-left corner of the plot with the positive x-axis running from left to right across the plot and negative y-axis running down the left-hand edge of the plot (fig. 4). Plot elevations were measured using an electronic survey instrument, Nikon Model 352, at major break points along transect lines spaced 0.10 m apart. The density of points ranged from 280 to 430 points per square meter. The array of X' and Y' values (measured by the electronic survey instrument) were rotated to X and Y values by using a rotation angle based on the two end-points of the y = –0.90-m transect line. The array was then translated to match the coordinates (x- and y-values) of these two end-points. The minimum elevation within each plot was subtracted from all elevations (Z-values) to give z-values, which represent elevation above the lowest point in the plot.

The topographic point data were gridded to a raw digital elevation model (DEM) with 0.01-m cell spacing using a linear interpolation algorithm (MATLAB Inc.). The data in the raw DEM were extrapolated beyond the side, top, and bottom boundaries of the plot such that the x-coordinate ranged from –0.1 to 1.1 m and the y-coordinate ranged from 0.1 to –1.1 m. The extrapolation beyond plot boundaries was required to eliminate errors at the boundaries during interpolation.

This raw DEM was truncated to the plot DEM by using the following procedure. First, the minimum and maximum grid-cell coordinates of the plot DEM were calculated. The grid cell with the minimum y-coordinate, y_{min}(m), was determined by examining the topographic point data and selecting the grid cell that included the minimum y input. For example if y_{min} was –0.932 m then the minimum cell would have a y-coordinate of –0.94 m. The y_{max} was then calculated on the basis of adding rows to the minimum coordinate until the rounded-off grid area equaled the calculated plot area. The grid x_{min} was set to 0 and the grid x_{max} was set to 1.0. Given these plot coordinates, the raw (extrapolated) DEMs were clipped to the final grid coordinates using the clipping tool in ArcMap, which allows the user to specify the minimum and maximum grid coordinates.

In calculating flow networks, the DEMs were further modified to resolve some numerical, edge-effect issues in RiverTools (Rivix LLC, 2001). In calculating flow directions, the water "flowed" off the right or left edge (along the y-axis) unless a topographic barrier was added outside the grid to force water downslope to the plot outlet (collecting apron). This action, similar to having a plot border, was achieved by adding two columns of cells (x+1 and x+2 on the right side) to the right and left side (y-axis) of the DEM. On the right side, the elevations in these two cells would be z+0.1 m and z–0.1 m, respectively. The presence of the increased elevation in the x+1 barrier cell kept the flow from the plot from going off the edge of the DEM. However, the x+1 (barrier) cell would drain into the plot, adding contributing area, unless another row was added. By making the elevation in the x+2 cell less than in the x cell, the water from the barrier cell, x+1, flowed toward x+2 cell and not toward the plot. A similar issue existed for the upper row of cells in the DEM. To remedy this, we added two rows at the top of the DEM so that the actual elevation data would not be affected but the water

would flow downslope toward the collecting apron. Finally, we addressed the edge effect for the lowest row (adjacent to the collecting apron). Some quantities (flow length for example) are not calculated for this lowest row because it was at the edge. We calculated the elevation of this lowest cell by using the local slope. If the lowest cell was y, then the elevation z of the y–1 cell was calculated as $z_{y-1}=2z_y-z_{y+1}$. The final result of all of these modifications was to add three rows and four columns to the DEM. None of these added, artificial data are considered when computing averages of slope, flow length, or elevation.

Slope, flow directions, and flow lengths were calculated from these modified 1-m^2 DEMs. The slope (finite-difference) and flow length were computed using the program RiverTools, the D–8 algorithm (Jenson and Domingue, 1988), which generated one-dimensional flow directions on the DEM, and the imposed gradient plus algorithm (Garbrecht and Martz, 1997; Rivix LLC, 2001), which resolved flow directions. A drainage network was thus created and exported as a shape file and then used to compute the number of flow paths. The shape file included drainages in the topography added along the edges (see modifications discussed previously), and these were removed in the program ArcGIS. To calculate the number of distinct flow-path sources, we used the number of first-order streams or the network magnitude. The length of each flow path was the sum of the cells from the source to the collecting apron. For each plot, we also computed means and coefficient of variations for the elevation, local slope or gradient for each cell, and the flow-path lengths. The minimum elevation should be 0, but because additional cells were added (see modifications) we computed the mean elevation and then subtracted the computed minimum elevation from the mean. Similarly, because an extra row was added to the bottom of the DEM, all flow paths were 0.01 m too long, so 0.01 m was subtracted from the average. Finally, the slope grid was a finite-difference approximation where x=0 m and x=1 m were affected by the presence of the artificial data, and therefore these data were not included in the average.

After all the rainfall simulation experiments, the plots also were excavated to a depth of about 0.30 m along the 0.10-m transect lines. The thickness of ash was measured along these transect lines, and the locations of cobble-size and larger rocks were mapped. Representative samples of the underlying soil and overlying ash were collected, and particle-size distributions were measured in the laboratory by using a set of standard sieves, which separated the soil particles into whole phi (ϕ) size classes ($\phi = -\log_2$) of the particle-size diameter in millimeters; Krumbein, 1934). These sieves were put on an automatic sieve shaker for about 15 minutes, and the mass of each particle-size class was then weighed to produce grain-size distribution curves (Guy, 1969).

Additional measurements were made of the organic content, bulk density, and particle density of the ash. The organic content was measured using the loss on ignition method (LOI) at 550°C (Håkanson and Jansson, 1983) for one sample of ash (from each plot), which was separated into different size classes. Bulk density measurements also were made for different size classes, but because the samples for each plot were small, the bulk density was measured for a large sample (collected from an eolian deposit in the lee of a hill about 100 m from the north-facing study area) that provided enough volume of ash for a bulk density measurement in each size class. Particle densities of three ash sizes (less than 0.063, 0.063–0.125, and 0.125–0.250 mm) were measured using approximately 0.0005-kg samples. The ash was slowly added to water in a small-diameter tube (0.008 m) and allowed to settle. The accuracy of the mass measurement was about 1 part in 1,000, but the accuracy of the volume measurement was only about 1 part in 10, which limited the particle density of the ash to 2 significant figures. To decrease the number of possible voids in any organic material in the ash, the 0.063–0.125-mm and the 0.125–0.250-mm size fractions were ground with a mortar and pestle, and only the material that passed through a 0.063-mm sieve was used to determine the particle density.

Rainfall Simulations

Fourteen rainfall simulation experiments were run on plots in the north- and south-facing study areas. Three experiments were run on each of the two north-facing plots and four experiments were run on each of the two south-facing plots. The experiments had rainfall intensities that varied from 19 mm/h to 50 mm/h. The rainfall in all experiments lasted 30 minutes, and runoff was collected each minute during the rainfall and for 2–3 minutes after the conclusion of the rainfall.

The primary experimental measurement was plot runoff. Runoff was collected at the base of the plot (fig. 4) in the 0.07777-m^2 triangle-shaped collecting apron that funneled water to a collection container (fig. 4). The collecting apron was shielded by a lid to prevent rain from falling on the apron and generating runoff that was not from the soil surface inside the plot. The uphill edge of the collecting apron protruded 0.0254 m into the plot so that the soil surface started at y=0.0254 m. Manual collection of runoff at the plot outlet used a plastic container that was switched with another container at 1-minute intervals (a couple intervals were inadvertently longer or shorter). Total runoff for the collection interval was measured in one of two graduated cylinders (0.100 L and 1.000 L) depending upon the runoff rate or discharge.

Soil Moisture

Samples for gravimetric soil moisture and particle-size distribution were collected before and after each simulation experiment directly adjacent to the plot. Samples were collected at two or three depths, usually as composite samples for the intervals 0.00–0.05, 0.10–0.15, and 0.20–0.25 m, but sometimes we sampled at other depths if obstructions existed in the soil. The soil sample was placed in a preweighed metal soil container, sealed, weighed, dried in the laboratory over-

night at 105°C, and reweighed after drying. Percentage soil moisture by mass, *SM*, was then calculated as:

$$SM = \frac{m_w - m_d}{m_d} \times 100 \quad (5)$$

where m_w (kilograms) is the wet mass and m_d (kilograms) is the dry mass (Gardner, 1986). Soil moisture by mass was converted to soil moisture by volume by multiplying by the soil bulk density.

Overland Flow Velocities and Suspended Sediment

For some experiments, steady-state overland flow velocities were measured at selected points within the plot. Two small-diameter pins were inserted adjacent to the visible flow paths, and red food coloring was added to the water above the upper pin; then the traveltime between the two pins was measured and recorded.

For some north-facing plot experiments, water samples were collected to measure the sediment concentrations. Successive samples of the 1-minute runoff were collected after the runoff from experiments 9, 10, 11, and 12 had reached a steady state (about 10–14 minutes) and added to a 1-L plastic bottle until it was nearly full. After the experiment, these samples were brought to the laboratory and the volume of water was measured. The sediment concentrations were separated into size classes by using the wet-sieving method and collecting the < 0.063-mm fraction on 0.45-micrometer filters, then drying and weighing.

Simulated Rainfall Characteristics

Spatial Variability

Spatial variability of rain intensity was measured primarily on a flat surface. The coefficient of variation (CV) of the rainfall produced by the standard nozzles (FullJet® nozzles with spray angles of 67–90 degrees and rainfall intensities ranging from 217 to 557 mm/h, table 1) and collected in the 45 small rain-gage array ranged from 0.07 to 0.47. The CV in rainfall intensity was lowest (0.07) for the GG22 nozzle, which had the highest spray angle of the four nozzles (90° at 138 kPa and not listed but assumed similar for tested 276 kPa). This observation suggested that spray homogeneity is related to greater spray angles. Subsequently, we tested the wide-angle nozzles (about 120˚) GG2.8W, GG10W, and GG20W for field application because of their potential to provide a more homogeneous rainfall distribution than the standard nozzles.

The wide-angle nozzles produced rainfall intensities similar to rainfall intensities in the Colorado foothills, varying from 18 to 57 mm/h for a 1.1-m spray circle on a level surface (table 1). Also, the wide angles reduced the coefficient of variation of the rainfall intensities in the rain gage array to ≤0.16, indicating a more homogeneous spray distribution (fig. 6). Even on the logarithmic scale in figure 6, the differences in variability between wide-angle and standard-angle nozzles are visible. Thus, we used these three wide-angle nozzles for field applications. All the analyses in the remainder of this report only refer to the three nozzles: GG2.8W, GG10W, and GG20W.

Few studies have examined the spatial variability in simulated rainfall in detail. One such study (Laschelles and others, 2000) identified large differences in rain intensity during the use of a system that consisted of four full-cone nozzles (like the FullJet® nozzles). In that example, rainfall intensity varied from greater than 50 mm/h to less than 20 mm/h on a 20-minute simulation with a mean rate of 40 mm/h (Laschelles and others, 2000, their figure 2a). Given a similar type of cone nozzle in this study, the results here are more encouraging as the maximum difference in rain gages is 18 mm/h (fig. 6). If our results are computed as a coefficient of uniformity (1-CV), our nozzles have 92-percent uniformity compared to 93 percent estimated for Cerdà and others (1997) over a much smaller area (0.24 m^2) and ≈ 80 percent for Laschelles and others (2000, their figure 3). Reported coefficients of uniformity for an automated programmable simulator varied between 85 to 90 percent for the same intensity range (Niebling and others, 1981) and the coefficient of uniformity for a Spraying Systems square nozzle was about 80 percent (Esteves and others, 2000). Thus, it appears that these wide-angle nozzles produce as uniform or more uniform rainfall intensity than other rainfall simulators.

The measured rainfall intensity was compared to the predicted intensity. The nozzle characteristics (spray angle and flow rate at a given pressure) were provided by Spraying Systems (2005) and were used to predict the rainfall intensity assuming a 1.4-m height, a triangular geometry, and radial symmetry in spray. The data (table 1) indicate that intensities calculated using this simplified geometry underpredict all measured intensities at all pressures. This underprediction is due to simulated rainfall bending as it falls to the ground and concentrating higher rainfall intensities closer to the center of the spray circle (de Lima and others, 2002, their figure 12).

Drop Characteristics

The 2DVD evaluation of raindrop characteristics indicated that, although the rain intensities could be applied at the desired intensities, the characteristics of the simulated rain were different from natural rains. Empirical curves (Gunn and Kinzer, 1949; Atlas and others, 1973) of raindrop velocity as a function of raindrop diameter indicate that, for large drops (greater than 5 mm), the terminal velocity approaches 9 m/s in natural rain (fig. 7; Gunn and Kinzer curve). The data in this study from 1.4 m below the nozzle show two distinct patterns (figure 7 is a representative sample). For drop diameters less than 1 mm, the drop velocities form a vertical cluster ranging

Table 1. Characteristics of rainfall intensity measured on a level surface.

[m, meters; kPa, kilopascals; psi, pounds per square inch; CV, coefficient of variation equal to standard deviation divided by the mean; mm/h, millimeters per hour; L, liter; min, minutes; MJ, megajoules; ha, hectares]

Nozzle	Height above level surface (m)	Pressure		Rainfall intensity				Prescribed flow rate (L/min)[d]	Approximate spray angle at reference pressure[d,e] (degrees)	Unit rainfall energy[f] (MJ/ha/mm)
		(kPa)	(psi)	Measured by small rain gages (mm/h)	CV	Calculated spray cone[b] (mm/h)	Estimated from nozzle data provided by supplier[c,d] (mm/h)			
GG10	1.45	69	10	217	0.42	206	84	3.8	67	0.29
	1.45	276	40	361	0.36	307	160	7.2	67	0.29
GG15	1.48	34	5	277	0.47	219	93	4.2	67	0.29
	1.47	69	10	232	0.47	181	126	5.7	67	0.29
	1.47	276	40	493	0.35	420	244	11.0	67	0.29
GG22	1.47	34	5	228	0.24	203	59	6.1	90	0.29
	1.47	69	10	258	0.20	234	81	8.3	90	0.29
	1.46	276	40	439	0.07	438	155	15.9	90	0.29
GG32	1.47	34	5	406	0.37	335	144	8.7	75	0.29
	1.43	69	10	398	0.30	348	200	12.1	75	0.29
	1.43	138	20	557	0.29	487	276	16.7	75	0.29
GG2.8W[a]	1.40	34	5	18	0.16	18	2[g]	0.6	120	0.21
GG10W[a]	1.38	34	5	33	0.10	33	9	2.8	120	0.25
	1.38	138	20	57	0.08	56	17	3.8	120	0.28
GG20W[a]	1.38	34	5	43	0.12	40	18	5.7	120	0.26
	1.38	69	10	55	0.07	53	25	7.6	120	0.28

[a] Selected for field applications.

[b] Assumes circle with 1.1-m diameter.

[c] Assumes circle on ground based on height (1.4 m), spray angle, and prescribed flow rate at given pressure.

[d] Reported in Spraying Systems Company, 2005.

[e] Reference pressure for standard nozzles: 138 kPa; reference pressure for wide-angle nozzles: 69 kPa.

[f] Calculate using equation (4) and the rainfall intensity measured by the tipping-bucket rain gage.

[g] Calculated with data at 69 kPa, no manufacturer data below this pressure.

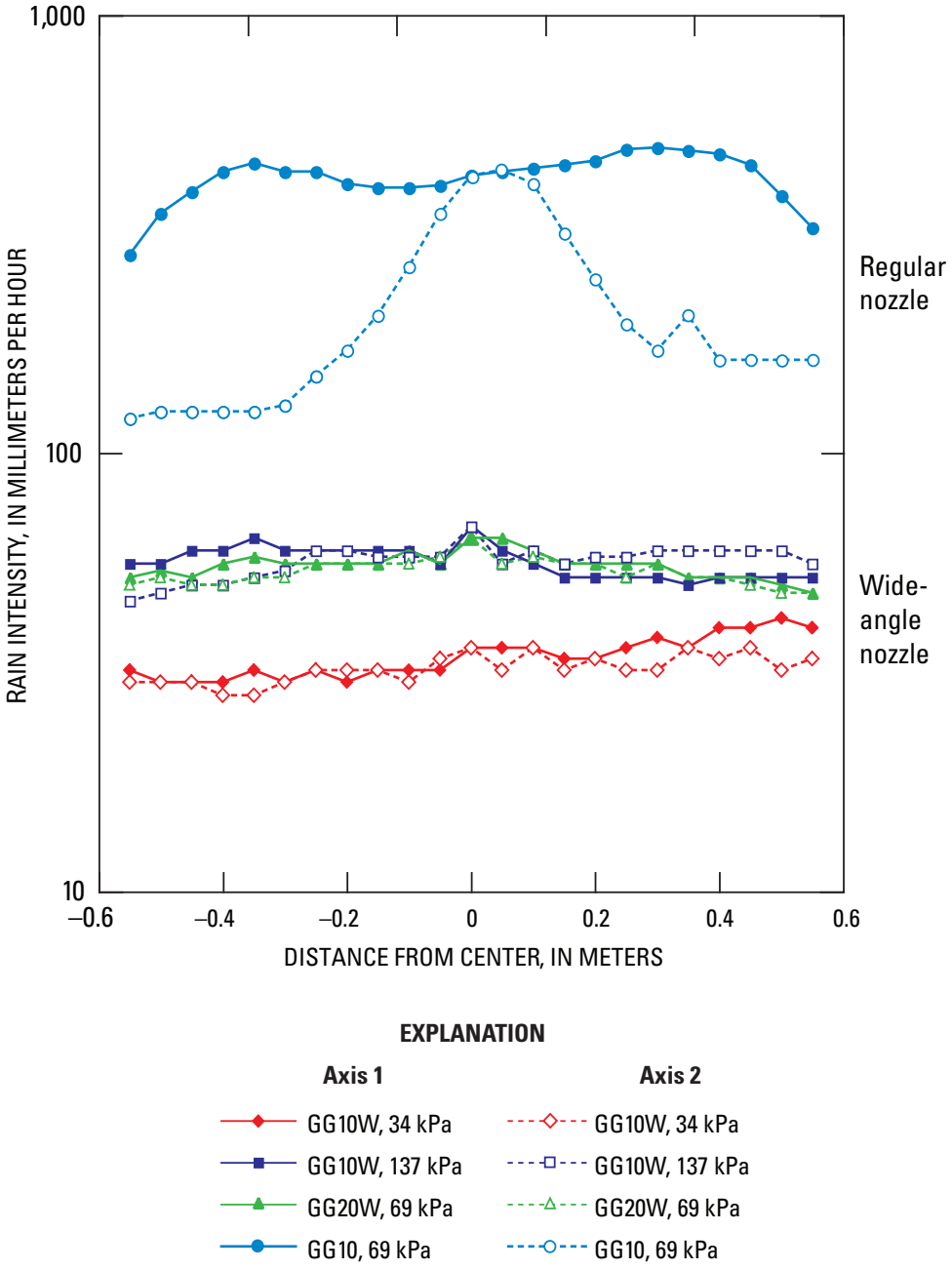

Figure 6. Comparison of the spatial distribution of rainfall produced by different nozzles measured from an array of 45 rain gages (see figure 3).

from 0.5 to 8 m/s. These drops are undoubtedly those that are near the measurement limit of the 2DVD and thus show variability and potential error (Kyoko Ikeda, National Center for Atmospheric Research, oral commun., 2004). A second cluster for larger drop sizes (greater than 1 mm) appears to approach an asymptote near 5 m/s. These velocities are less than natural rainfall but are in fact similar to the velocities measured by Laws (1941; his table 2) for drops originating at 1.5 m (fig. 7). Thus, the similarity between the drop velocity from 1.5 m and the rainfall-simulator drop velocities from almost the same height (1.4 m) imply that the rainfall simulator imparts little velocity to the drops.

Another characteristic, which provides a comparison to natural rain, is the relation between oblateness of raindrops and raindrop diameter. As in the relation between drop diameter and drop velocity, a data cloud is close to the graph origin (fig. 8) that reflects the measurement limitations of the 2DVD. At diameters greater than 2 mm, the drops are closer to a

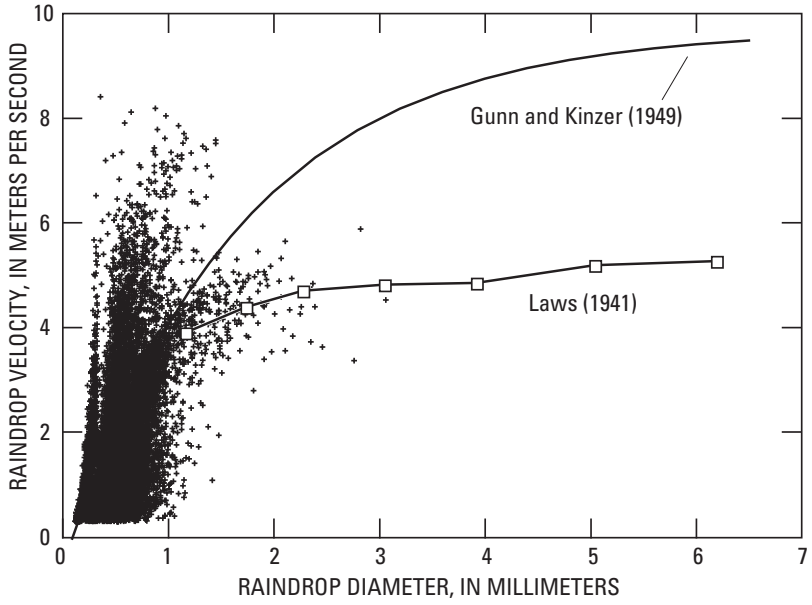

Figure 7. Relation between raindrop diameter and velocity produced by nozzle GG20W and measured using a two-dimensional video disdrometer at 1.4 meters below the nozzle

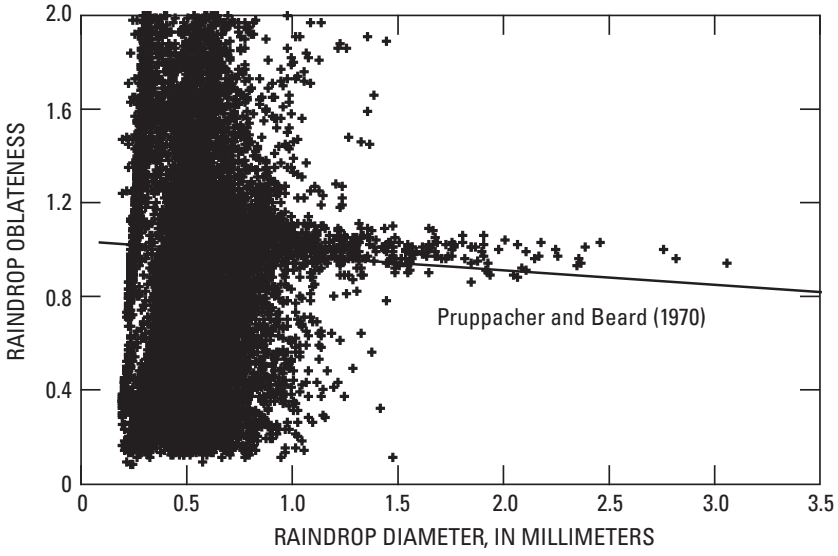

Figure 8. Relation between raindrop diameter and oblateness produced by nozzle GG20W and measured using a two-dimensional video disdrometer at 1.4 meters below the nozzle

sphere or prolate spheroidal shape (oblateness ≥1) than natural rainfall, which tends to flatten as it falls and approximate an oblate spheroidal shape (see empirical relation of Pruppacher and Beard (1970) in figure 8 and Laws (1941, his figure 4 for picture of drop). The shape initially imparted by the nozzle does not change appreciably because of the short fall time from the nozzle to the disdrometer or from the nozzle to the soil surface.

Unit rainfall energies produced by the simulator are less than those calculated using the empirical equation of Brown and Foster (1987) (equation 4). The measured unit rainfall energies produced by the simulator (calculated with equation 3) were about 20–25 percent of the predicted energy for storms with the same rainfall intensity (table 2; unit rainfall energy and calculated unit rainfall energy). The reduction in energy is due to the aforementioned reduction in velocity and also a reduction in drop size. The nozzle drop distribution is skewed to a finer drop size than natural drop distributions. The mass-weighted mean diameter values of convective rain for Colorado are typically greater than 2 mm (Brigini and others, 2003, their figure 11) whereas the similar calculation for the nozzles indicates a mass (volume)-weighted mean diameter of about 0.69–1.03 mm (table 2).

Similar rainfall-simulator designs also underproduce unit rainfall energies. For example, another similar single-nozzle system produced only 36 percent (Wilcox and others, 1986) of natural kinetic energies. Increasing applied unit rainfall energy with the Spraying Systems FullJet® nozzles will be difficult. Because little incident velocity is derived from the nozzle, the only method by which to increase velocity is to raise the height of the nozzle. Over short distances, this may reduce the coefficient of variation of rainfall intensity, but setting up a rainfall simulator at great height on a steep slope has practical difficulties. Little can be done to increase drop size. The wide-angle nozzles that are used here, particularly GG20W, are among the largest manufactured, and they are being operated at a low pressure. Therefore, options for increasing drop size and velocity will likely shift to a different nozzle design like the VeeJet nozzles recommended by Mutchler and Hermsmeier (1965) and used by Meyer and Harmon (1979) and Paige and others (2003). Using this VeeJet nozzle may require

Table 2. Disdrometer characteristics of the simulated rainfall produced by three nozzles.

[kPa, kilopascals; psi, pounds per square inch; center, measurements were made 1.4 m directly below the nozzle; CV, coefficient of variation equal to standard deviation divided by the mean; mm, millimeter; m, meter; h, hour; MJ, megajoules; ha, hectares]

	Nozzle			
	GG2.8W	GG10 W		GG20W
Pressure (kPa)	34	34	138	69
Pressure (psi)	5	5	20	10
Numerical average drop size (mm), center	0.42	0.50	0.48	0.52
Numerical average drop size (mm), 0.5 m off center	0.49	0.53	0.49	0.49
Volume average drop size (mm), center	0.77	1.03	0.75	0.93
Volume average drop size (mm), 0.5 m off center	0.69	0.83	0.69	0.88
Volume average velocity (m/s), center	2.40	2.92	3.17	2.90
Volume average velocity (m/s), 0.5 m off center	2.08	2.79	3.14	2.90
Disdrometer intensity (mm/h), center	7.48	31.70	27.69	46.51
Disdrometer intensity (mm/h), 0.5 m off center	14.23	40.52	27.19	29.42
Drops/m^2/s, center	27,103	69,459	85,064	103,024
Drops/m^2/s, 0.5 m off center	46,391	93,550	83,840	75,377
Unit rainfall energy[a] (MJ/ha/mm), center	0.04	0.05	0.06	0.06
Unit rainfall energy[a] (MJ/ha/mm), 0.5 m off center	0.03	0.05	0.06	0.05
Calculated unit rainfall energy[b] (MJ/ha/mm), center	0.15	0.25	0.24	0.27
Calculated unit rainfall energy[b] (MJ/ha/mm), 0.5 m off center	0.19	0.26	0.24	0.24
Integrated rainfall intensity on Plot N15 (mm/h)	18.77	29.51	47.36	46.13
Temporal CV of the integrated rainfall intensity on Plot N15	0.03	0.01	0.06	0.02

[a]Unit rainfall energy was calculated using the equation (3) for each recorded raindrop.

[b]Calculated unit rainfall energy was calculated using the equation (4) and the observed intensity.

additional experimental infrastructure and depart from our design objectives for the development of a rainfall simulator.

Despite the utility of the 2DVD for measuring a large number of drops, there is error in its drop calculations. When we used lower flow-rate nozzles (GG2.8W and GG10W) at higher pressures, the rain intensity measured by the 2DVD was less than the intensity measured on a level surface (tables 1 and 2). For example, the 2DVD-measured intensity (measured at the center of the rainfall pattern of the GG10W nozzle operated at 34 kPa or 5 psi) was 33.67 mm/h, which was similar to the intensity (33 mm/h) measured in the laboratory on a level surface (compare tables 1 and 2). However, when the nozzle was operated at a higher pressure (138 kPa or 20 psi), the 2DVD intensity was 27.69 mm/h and the intensity of a level surface was 57 mm/h. This reduction of intensities could be a function of having too many small drops to count because the phenomenon was most pronounced when the drop sizes were smallest (the GG2.8W nozzle and the GG10W nozzle with the high flow). Alternatively, this underestimate of rain intensity could be a function of measurement setup. The 2DVD opening is 1 m off the ground and required our tripod to be elevated to a height (2.4 m) at which it may be more vulnerable to wind. Thus, the estimates of unit rainfall energy may be in error, but the data do suggest that the nozzles produce simulated rain, which has less energy than natural rain. This makes assessment of surface-sealing processes difficult; however, runoff was still produced in the field without the requisite unit rainfall energy associated with natural rain.

This study is similar to only a few studies (for example, Paige and others, 2003) in its use of automated analysis of raindrop fields. Using the 2DVD provided some interesting data to compare the simulated rain to natural rain. However, its application appeared to be limited by the large number of drops. Thus, at this point, we recommend the use with the caveat that the estimates of small drop sizes could be in error and that results are optimized with rain fields with larger and fewer drops.

Incident Rainfall

The spatially integrated rainfall intensity was assumed to represent the "actual" incident rainfall intensity on the plot. Spatially integrated rainfall intensity was related directly to the intensities measured by the tipping-bucket rain gages and indirectly to the intensities measured by the small rain gages. The tipping-bucket rain-gage method was used during the sheet calibration experiments so tipping-bucket intensities can be directly compared to the spatially integrated rainfall intensity (table 3). For this comparison, the intensities for the three tipping-bucket rain gages were averaged and compared to the spatially integrated rainfall intensity (average runoff rate/horizontal projection of the plot area) from the sheet calibration experiments. However, the tipping-bucket rain gage at the upslope edge of the plot consistently produced higher rainfall intensities (60–70 mm/h) for the nozzle-pressure combination of GG10W, 34 kPa (table 3 and table 4). This can be interpreted as being an edge effect of the spray, but including this gage into the average tends to overestimate the tipping bucket rain estimate relative to the spatially integrated rainfall intensity. To correct for this bias, the upslope gage was omitted from the average in this sheet calibration experiment (table 3) and in the rainfall simulation experiments when the GG10W nozzle was used at a pressure of 34 kPa (table 4). The calibration line (fig. 9) between the mean tipping-bucket rain-gage intensity (I_{mean}) and the spatially integrated rainfall intensity ($I_{integrated}$) was forced through the origin but shows a good fit (R^2=0.97, n=4):

$$I_{integrated} = 1.05 I_{mean} \quad (6)$$

The second calibration related the mean tipping-bucket rain-gage intensities and the small rain-gage intensities (I_{small_rain}) for experiments 7–14. This calibration was necessary because experiments 1–6 have no tipping-bucket data. This

Table 3. Sheet calibration of the nozzle rainfall intensity.

[All measurements were made on plot N15 with a slope of 0.37; the integrated intensities were computed for a horizontal surface; only the Middle and Bottom gages were used to compute the mean for the GG10W nozzle; kPa, kilopascals; mm, millimeters; h, hour; psi, pounds per square inch]

Nozzle	Pressure		Integrated rainfall intensity (mm/h)	Tipping-bucket rain gage intensity (mm/h)			Mean tipping-bucket intensity (mm/h)
	(kPa)	(psi)		Top	Middle	Bottom	
GG10W	34	5	34.3	63	38.8	32.9	35.9
GG10W	138	20	50.5	55.3	47.9	39.4	47.5
GG2.8W	34	5	20.0	21.2	16.9	12.5	16.9
GG20W	69	10	49.2	49.6	42.7	43.8	45.4

Table 4. Comparison of different field measurements of rainfall intensity.

[kPa, kilopascals; psi, pounds per square inch; mm/h, millimeters per hour; m, meters; L/min, liters per minute; the slopes of the plots were 0.41 for S13, 0.36 for S15, 0.31 for N13, and 0.37 for N15; tipping-bucket rain gages were outside and on the right-hand side of the plot; the distances below Top, Middle, and Bottom are measured from the bottom edge of the plot; --, no data]

Experiment	Plot	Nozzle	Pressure		Small rain gage (mm/h)					Tipping-bucket rain gage (mm/h)				Modified tipping-bucket rain gage (mm/h)	Incident rainfall intensity (mm/h)	Apron correction C_{apron} (L/min)
			(kPa)	(psi)	Top left	Top right	Bottom left	Bottom right	Mean	Top[a] 0.8 m	Middle[a] 0.5 m	Bottom[a] 0.1 m	Mean			
1	S13	GG20W	69	10	56	40	42	44	46	--	--	--	--	--	46	0.027
2	S15	GG10W	138	20	52	50	44	44	48	--	--	--	--	--	48	0.028
3	S15	GG10W	138	20	40	52	40	48	45	--	--	--	--	--	46	0.028
4	S13	GG20W	69	10	56	48	46	44	49	--	--	--	--	--	49	0.029
5	S13	GG10W	34	5	40	42	40	24	37	--	--	--	--	--	37	0.020
6	S15	GG10W	34	5	34	40	32	28	34	--	--	--	--	--	34	0.019
7	S15	GG2.8W	34	5	20	28	12	14	19	14	19	24	19	19	20	0.008
8	S13	GG2.8W	34	5	24	22	20	12	20	13	18	22	17	17	18	0.010
9	N13	GG2.8W	34	5	30	28	16	20	24	25	25	17	22	22	23	0.011
10	N13	GG10W	34	5	48	40	28	34	38	70	34	31	45	32	34	0.020
11	N15	GG2.8W	34	5	30	12	26	12	20	9	28	34	24	24	25	0.012
12	N15	GG10W	34	5	52	42	32	36	41	61	35	32	43	34	35	0.022
13	N15	GG20W	69	10	52	52	46	34	46	50	43	42	45	45	47	0.025
14	N13	GG20W	69	10	50	53	40	33	44	67	42	37	49	49	51	0.023

[a]The tipping-bucket rain gages in experiment 7 were located at 1.1, 0.5, and –0.1 meter.

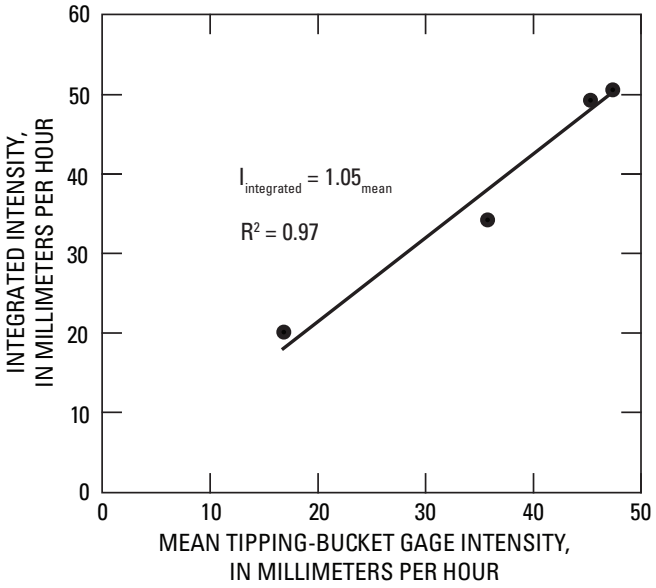

Figure 9. Calibration curve between spatially integrated rainfall intensity and mean tipping-bucket rainfall intensity.

calibration curve (fig. 10) also was forced through the origin (R^2=0.89, n=8):

$$I_{mean} = 0.96 I_{smallrain} \quad (7)$$

To compute the incident rainfall intensity for each experiment (1–14), two techniques were used depending on the available rain data. For experiments 7–14, the rainfall intensity was calculated using the mean tipping-bucket rain-gage data and converted to the integrated rainfall intensity by using equation (6) to give the incident rainfall intensity. For experiments 1–6, the two regression equations were used in succession. Starting with the available small rain-gage intensities, these were converted to mean tipping-bucket rain-gage intensities using equation (7). Then, the mean tipping-bucket rain-gage intensities were converted to the spatially integrated rainfall intensity using equation (6) to give the incident rainfall intensity. Because all the slopes of the calibration equation were within 4–5 percent of 1.00, it is implied that all the methods will provide a fairly similar estimate (8–10 percent) of incident rainfall (table 4). On average, the rainfall intensities measured by (1) the four small rain gages was 0.3 percent lower than the integrated rainfall intensity (CV of difference is 10 percent) for experiments 1–14, and (2) the mean tipping-bucket rain-gage intensity was 0.9 percent higher than the

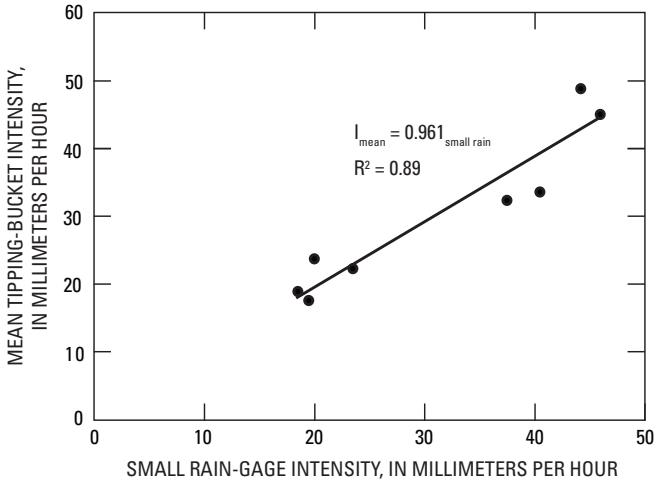

Figure 10. Calibration curve between small rain-gage intensity and mean tipping-bucket rainfall intensity.

integrated rainfall-intensity (CV of difference is 15 percent) for experiments 7–14.

Spatial variability of rainfall intensities was measured at the field sites on sloping surfaces. Variability exists in the measurements made between small gages at the lower and upper edges of the plot. Further, tipping buckets deployed in the field also indicate upslope (y-axis) variation in rainfall intensities. The best example of variability is the nozzle GG10W at 34 kPa. This combination produces an intensity at the upslope edge of the plot that is almost double that of the mean intensity for the plot. These calibration data indicate that this gage is consistently high in all measurements and anomalous relative to the mean intensity measured over the plot.

Despite the up- and downslope variability of spray measured during field applications of the rainfall simulator, little cross-slope variability is apparent. If extensive cross-slope variability in the spray existed, then the exterior rain gages would measure different rainfall intensity than that measured on the plot. However, the on-plot and outside-plot estimates are very similar in the calibration runs. Further, by comparing the intensities from several simulations with the same nozzle in pressure to the calibration data, very little variability exists among runs ($R^2 = 0.92$, slope 0.98). Therefore, the simulator is able to replicate fairly constant rainfall intensity throughout multiple simulations. Rainfall rates applied during the experiments varied from 18 to 51 mm/h (table 4).

Temporal Variability

The tipping-bucket rain gages also measured the temporal variation in rain intensity during the rainfall simulation experiments. Changes in rainfall intensities may indicate variability in pumping rates or the change in the simulator environment (for example wind velocity). For experiments 1–6, rainfall intensities computed for each 2-minute interval for a single, tipping-bucket rain gage were evaluated, and for experiments 7–14, the average intensity (three gages) computed for each 2-minute interval was evaluated. Each trend was evaluated for significance using an F-test and a significance level of α=0.05. Of the 14 tests, only three had significant linear trends (experiments 3, 12, and 13). Experiment 3 had a change in average rainfall intensity of 9.3 mm/h over the length of the experiment (0.31 mm/h/min), experiment 12 had a change of 4.1 mm/h and experiment 13 had a change of 3.2 mm/h. Thus, the only significant linear change related to an evident change in pumping rate was experiment 3 (N15, GG10W, 138 kPa). Experiment 2 had a significant quadratic trend where the rainfall intensity increased during the middle of the experiment and then dropped toward the end.

The disdrometer was used to make similar estimates of temporal variability for each nozzle. However, the data for the disdrometer tests were recorded at a shorter interval (15 seconds) and over a smaller area (about 0.10 m by 0.10 m window). The disdrometer data showed that four of the eight tests had significant changes in rainfall intensity over the about 3-minute measurement periods. Of the four tests, one (GG20W at 69 kPa) changed 6.9 mm/h over the 3-minute test (2.3 mm/h/min). The averaged change for the other three tests was 2.2 mm/h over the 3-minute test, suggesting the changes were greater during the disdrometer tests than the field experiments. This may suggest that short-term temporal variability may be higher than longer term temporal variability. Alternatively, the windy disdrometer test site may have had conditions conducive to higher short-term temporal variability than the field site.

Study Area

Topography

Both study areas consisted of two quasi-planar slopes with a slope break that divided the study areas into about equal areas of upper and lower slope. The upper slope was steeper than the lower slope (fig. 5A and 5B), and both slopes were greater in the south-facing study area than in the north-facing study area. The typical slope of the upper slope was 0.54 in the south-facing and 0.50 in the north-facing study area and was 0.40 and 0.35 on the lower slopes, respectively. The experimental plots were on the lower slopes in both study areas. The north-facing study area had an area with a third slope (0.20) at the bottom that may have been a small terrace adjacent to the stream but has been used for the access road (Forest Service road 284.1). The lower slope in the south-facing study area continued about 10 m farther and formed the left bank of the stream channel (fig. 1).

Surficial Features

In both study areas, the upper slope had bedrock outcrops, and on the lower slope this bedrock is covered by soil. The bedrock is lithic material greater than 50 mm in diameter,

and the average difference between the two independent estimates of the percentage of bedrock is 1.4 and 3.8 percent in the north- and south-facing study areas, respectively. The bedrock outcrops on the upper slope in the south-facing study area were more continuous (mean percent=31 and CV=1.0) than in the north-facing study area (mean =11 percent and CV=1.2). No substantial bedrock outcrops existed on the lower slopes (table 5).

The mean depth of ash was similar between the upper and lower slopes of the study areas. In the south-facing study area, the ash on the upper slope had mean thickness of 10 mm and on the lower slope a mean thickness of 15 mm (table 5). The maximum thickness on the upper slope was 70 mm, which had collected between a large root and rock, and the maximum thickness on the lower slope was 42 mm. The litter and duff layer, which remained after the fire under the ash at many sampling sites, was charred in many samples and was about 10 mm on the upper and lower slopes. In the north-facing study area, the mean ash thickness was similar to the south-facing study area but was more uniform on the upper (14 mm) and lower slopes (15 mm) than in the south-facing study area (table 5). The litter and duff layer that remained after the fire was much thicker than the layer on the south-facing study area. The mean thickness was 37 mm for the two lowest transects on the upper slope (third, topmost transect was near to ridge crest and was not measured but was very rocky) and 32 mm for the three transects on the lower slope. The presence of the litter and duff layer in both study areas indicates that the fire had a low soil severity even though the condition of the vegetation indicated a high burn severity. This thicker litter and duff layer in the north-facing study area reflects the wetter soils and greater biomass density on the north-facing than on the south-facing slopes.

The soil in the south-facing study area was generally coarser than the soil in the north-facing study area. The maximum particle size (30 mm) was limited by the size of the soil core. Thus, large gravel, cobbles, and rocks were not sampled, but some were sampled as bedrock material. The mean, median diameter (D_{50}) of the particle sizes in the soil samples in the south-facing study area was greater on the upper slope (1.02 mm) than on the lower slope (0.74 mm) and these D_{50} were greater than those in the north-facing study area (0.88 mm and 0.46 mm, respectively). However, the variability (measured by the coefficient of variation) in upper slope of the north-facing study area (CV=0.84) was greater than the south-facing study area (CV=0.58), but the opposite was true on the lower slopes.

Rainfall-Simulation Experiments

Plot Topography

The topographic variability and flow-path characteristics were similar among the four experimental plots. The mean elevations above the lowest point in the plots were slightly greater in plot S13 than in the other plots (table 6, figs. 11–14). This is probably caused by the large rocks on the surface of plot S13 (fig. 13); however, the coefficient of variation in elevation was essentially the same (0.54 to 0.57) for all plots. The local gradients also were greater in plot S13 than in the other plots and also may reflect the presence of the large rocks. Remnants of burned vegetation were common in the north-facing plots, and plot N13 had the greatest spatial variability of the gradient (figs. 11 and 15), while plot N15 (figs. 12 and 16) had the fewest sources of flow paths, both of which may reflect the effects of vegetation. In general, the theoretical drainage network is similar within each plot. It consisted of a 6th-order system with essentially the same number of flow paths, flow-path lengths, and contributing area in each plot (table 6).

Plot Stratigraphy

All four plots were on the lower slopes of the study areas and were mostly covered with a deposit of ash. The maximum thickness (tables 7 and 8) of ash was greater on the north-facing plots (80 mm in N13 and 120 mm in N15) than on the south-facing plots (70 mm in S13 and 32 mm in S15). Rocks, bones, roots, and stumps of small trees and herbaceous vegetation also were on the surface besides the deposit of ash. Plots N13 and N15 included stumps of vegetation that determine some of the topography (figs. 15 and 16). Large rocks were mostly on the surface in plot S13 (figs. 13 and 17), bones were only in plot N15 (fig. 12), and plot S15 had only the layer of ash (fig. 18). The largest subsurface rocks were in plot N15 (fig. 16). Subsurface roots and holes dominated plot N15, but plot S15 (fig. 18) also had a few large subsurface roots but few surficial features.

Ash and Soil Characteristics

Particle sizes of the ash and soil were finer on north-facing plots than on the south-facing plots. One sample of ash and soil was collected from plots N13, N15, and S13, and five samples were collected from plot S15 when the plots were excavated (table 9). The finer ash on the north-facing plots than on south-facing plots (fig. 19) may reflect the difference in vegetation that burned on the north- and south-facing slopes. Soils on south-facing slopes are generally coarser and drier. Ponderosa pine is adapted to these drier soils (Bates, 1923, 1924) and has large needles and branches, which when burned created coarse ash. Soils on north-facing slopes, which are typically finer than south-facing soils, retain more soil moisture, which favors aspen and Douglas fir. When the aspen leaves and smaller fir needles burn, they create finer ash. An alternative explanation would be that the fire burned at a higher temperature on the north-facing slopes because of the greater fuel density and thus the combustion was more complete, producing a finer ash. Particle density of the ash varied from 1,700 to 2,400 kg/m^3.

Table 5. Summary of the spatial distribution of surficial material in the north-facing and south-facing study areas.

[mm, millimeters; CV, coefficient of variation; kg/m^3, kilograms per cubic meter; D_{50}, median grain diameter; --, no data]

	Sample number	Median	Mean	Standard deviation	CV	Skewness
			North-facing upper slope			
Percent bedrock	33	6.5	11	14	1.2	1.8
Ash thickness (mm)	20	11	14	19	0.70	1.0
Litter and duff thickness (mm)	20	40	37	23	0.63	–0.30
Bulk density (kg/m^3)	37	1,100	1,100	134	0.12	–0.33
Mean D_{50} (mm)	39	0.62	0.88	0.74	0.84	2.6
Soil size class:			Percent			
32–16 mm	39	0.0	3.9	8.5	2.2	2.2
16–8 mm	39	3.2	4.4	5.1	1.2	1.4
8–4 mm	39	9.0	10.9	9.1	0.83	2.8
4–2 mm	39	10.3	9.9	3.1	0.31	–0.04
2–1mm	39	11.5	12.0	2.5	0.21	0.49
1–0.5 mm	39	12.6	12.5	2.8	0.22	0.13
0.5–0.250 mm	39	13.8	14.4	3.7	0.26	0.82
0.250–0.125 mm	39	12.3	12.4	2.8	0.23	0.02
0.125–0.063 mm	39	7.4	7.5	1.9	0.25	0.47
Less than 0.063 mm	39	11.9	12.1	3.6	0.30	0.46
			South-facing upper slope			
Percent bedrock	33	21	31	31	1.0	1.2
Ash thickness (mm)	33	5	10	14	1.4	2.8
Litter and duff thickness (mm)	33	5	10	13	1.4	1.6
Bulk density (kg/m^3)	32	1,150	1,180	129	0.109	–0.14
Mean D_{50} (mm)	32	0.88	1.02	0.59	0.58	2.7
Soil size class:			Percent			
32–16 mm	32	0.0	1.7	6.7	4.0	3.9
16–8 mm	32	0.0	1.1	3.1	2.8	2.7
8–4 mm	32	11.0	13.2	7.9	0.60	1.8
4–2 mm	32	13.0	12.8	2.7	0.21	0.05
2–1mm	32	17.9	18.2	3.3	0.18	0.19
1–0.5 mm	32	14.6	14.3	2.6	0.18	-0.31
0.5–0.250 mm	32	12.6	12.5	3.3	0.26	0.79
0.250–0.125 mm	32	10.4	10.2	2.4	0.24	0.20
0.125–0.063 mm	32	7.2	6.9	1.7	0.25	0.13
Less than 0.063 mm	32	9.3	9.2	2.3	0.26	-0.26

Table 5. Summary of the spatial distribution of surficial material in the north-facing and south-facing study areas.—Continued

[mm, millimeters; CV, coefficient of variation; kg/m^3, kilograms per cubic meter; D_{50}, median grain diameter; --, no data]

	Sample number	Median	Mean	Standard deviation	CV	Skewness
			North-facing lower slope			
Percent bedrock	33	0.0	0.7	3.2	4.4	5.4
Ash thickness (mm)	18	13	15	5.8	0.39	0.91
Litter and duff thickness (mm)	18	27	32	21	0.65	1.1
Bulk density (kg/m^3)	36	1,100	1,080	119	0.11	–0.43
Mean D_{50} (mm)	42	0.45	0.46	0.16	0.34	0.7
Soil size class:			Percent			
32–16 mm	42	0.0	1.8	6.3	3.4	3.7
16–8 mm	42	0.0	2.0	3.2	1.6	1.7
8–4 mm	42	6.4	7.2	5.0	0.70	0.98
4–2 mm	42	7.7	7.7	2.4	0.31	0.31
2–1mm	42	11.7	12.2	4.0	0.33	0.65
1–0.5 mm	42	14.2	14.9	4.0	0.27	0.25
0.5–0.250 mm	42	15.5	15.5	3.0	0.20	0.33
0.250–0.125 mm	42	13.6	13.1	2.6	0.20	0.35
0.125–0.063 mm	42	8.8	8.8	1.7	0.20	0.17
Less than 0.063 mm	42	16.2	16.6	4.2	0.26	0.63
			South-facing lower slope			
Percent bedrock	33	0	5.7	12	2.2	2.6
Ash thickness (mm)	22	12	15	11	1.5	2.1
Litter and duff thickness (mm)	22	5	10	15	0.74	0.68
Bulk density (kg/m^3)	40	1,170	1,190	139	0.12	0.14
Mean D_{50} (mm)	40	0.72	0.74	0.30	0.40	0.73
Soil size class:			Percent			
32–16 mm	40	0.0	0.0	0.0	--	--
16–8 mm	40	0.0	1.7	3.6	2.1	2.5
8–4 mm	40	7.3	8.8	5.5	0.63	0.98
4–2 mm	40	12.2	12.2	4.2	0.34	0.72
2–1mm	40	18.1	17.6	3.4	0.19	-0.20
1–0.5 mm	40	15.3	15.6	3.2	0.20	0.88
0.5–0.250 mm	40	13.2	13.8	3.4	0.25	0.63
0.250–0.125 mm	40	11.2	11.7	2.9	0.25	0.39
0.125–0.063 mm	40	7.4	7.8	1.9	0.25	0.73
Less than 0.063 mm	40	10.3	10.8	2.9	0.26	0.95

Table 6. Topographic variability and flow-path characteristics for rainfall simulation plots.

[Mean elevation is measured above the lowest elevation (0.00 m) within the plot; CV, coefficient of variation; gradient is the maximum of the eight slopes from a specified cell; m, meters]

	Rainfall simulation plots			
	N13	N15	S13	S15
Mean elevation (m)	0.15	0.18	0.21	0.18
CV of mean elevation	0.57	0.54	0.55	0.54
Mean gradient	0.40	0.44	0.59	0.43
CV of mean gradient	0.62	0.55	0.69	0.33
Number of sources for the drainage network	1,621	1,588	1,817	1,680
Mean flow-path length from all source cells (m)	0.53	0.51	0.50	0.49
CV of mean flow-path length	0.58	0.58	0.57	0.58
Number of:				
1st-order flow paths	1,621	1,588	1,817	1,680
2nd-order flow paths	330	328	328	283
3rd-order flow paths	69	69	73	52
4th-order flow paths	16	20	18	13
5th-order flow paths	4	5	5	4
6th-order flow paths	1	2	1	1
Mean flow path length (m):				
1st-order flow paths	0.047	0.043	0.039	0.042
2nd-order flow paths	0.070	0.070	0.063	0.077
3rd-order flow paths	0.088	0.13	0.10	0.16
4th-order flow paths	0.22	0.20	0.22	0.26
5th-order flow paths	0.43	0.27	0.36	0.38
6th-order flow paths	0.34	0.28	0.12	0.27
Mean upstream contributing area (m^2):				
1st-order flow paths	0.000	0.000	0.000	0.000
2nd-order flow paths	0.002	0.002	0.002	0.002
3rd-order flow paths	0.006	0.009	0.007	0.010
4th-order flow paths	0.026	0.032	0.030	0.041
5th-order flow paths	0.15	0.086	0.11	0.12
6th-order flow paths	0.25	0.26	0.25	0.20

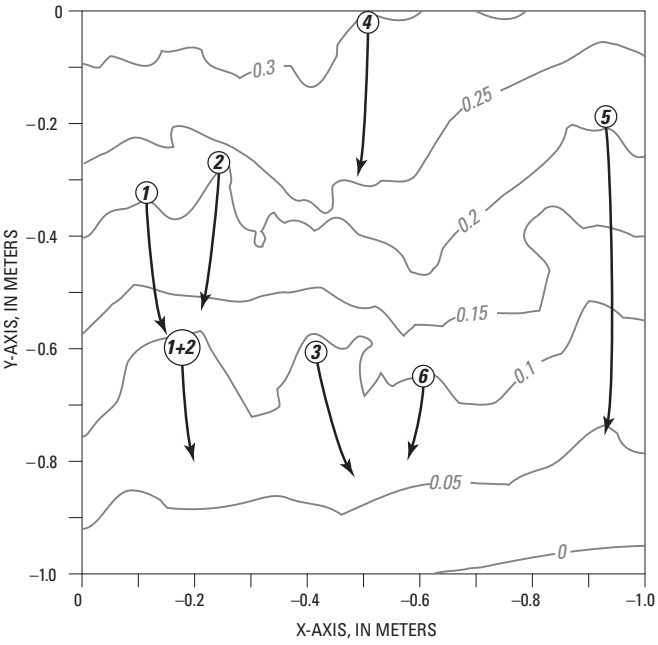

Figure 11. Photograph and topographic map of Plot N13.

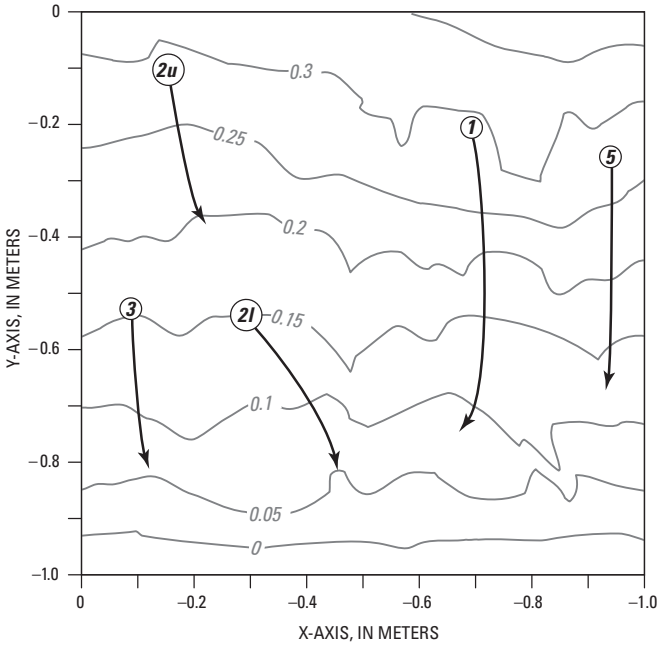

Figure 12. Photograph and topographic map of Plot N15.

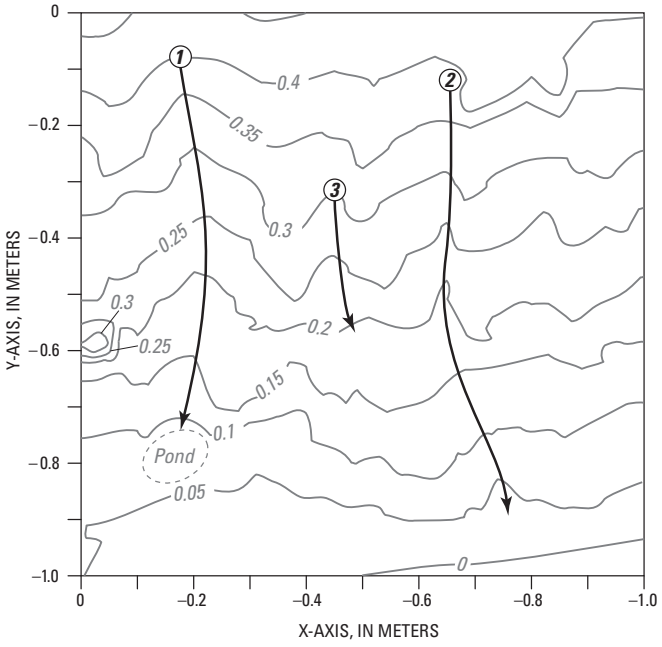

Figure 13. Photograph and topographic map of Plot S13.

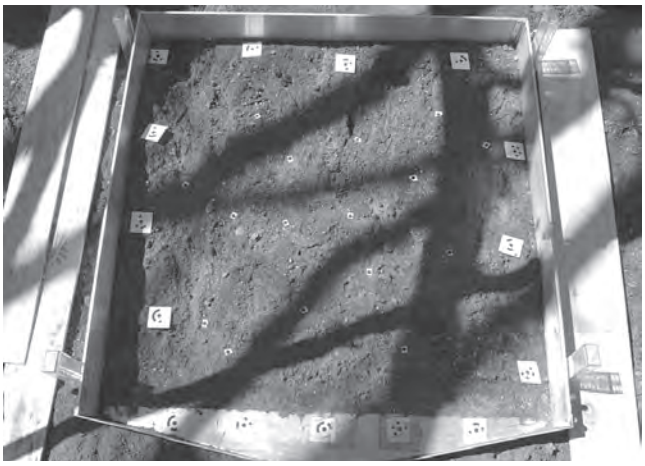

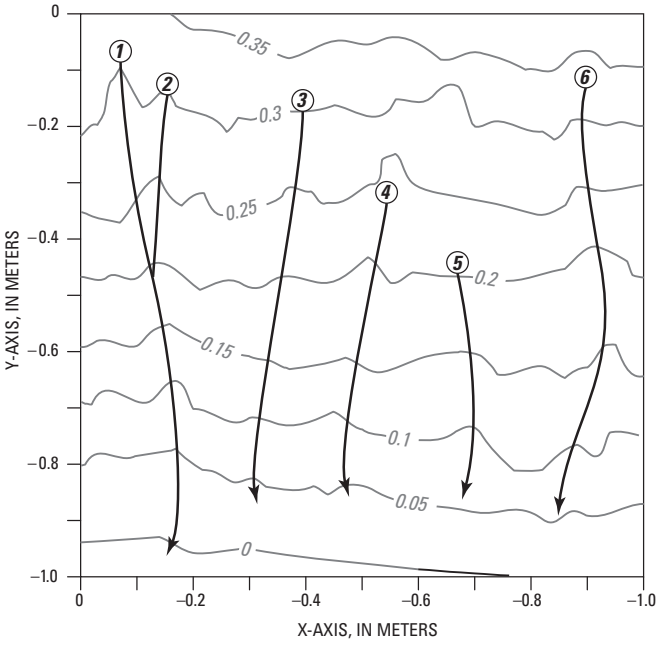

Figure 14. Photograph and topographic map of Plot S15.

Table 7. Ash thickness and surficial features in north-facing plots.

[Thickness between points should be interpolated linearly; m, meters; mm, millimeters]

Plot N13				Plot N15			
		Surface				Surface	
x (m)	y (m)	Ash thickness (mm)	Material	x (m)	y (m)	Ash thickness (mm)	Material
Average (mm)		10	Ash	Average (mm)		27	Ash
0.00	0	15	ash	0.00	0	30	ash
0.10	0	15	ash	0.10	0	40	ash
0.12	0	10	ash	0.20	0	40	ash
0.15	0	8	ash	0.30	0	45	ash
0.18	0	10	ash	0.40	0	40	ash
0.22	0	5	ash	0.50	0	25	ash
0.26	0	5	ash	0.60	0	20	ash
0.30	0	0	ash	0.70	0	25	ash
0.43	0	0	ash	0.80	0	30	ash
0.44	0	3	ash	0.90	0	30	ash
0.46	0	5	ash	1.00	0	30	ash
0.49	0	10	ash				
0.53	0	20	ash	0.00	–0.1	30	ash
0.57	0	15	ash	0.05	–0.1	30	ash
0.61	0	20	ash	0.10	–0.1	25	ash
0.62	0	0	burned	0.13	–0.1	10	ash
0.63	0	0	wood	0.16	–0.1	10	ash
0.64	0	0	40 mm	0.20	–0.1	10	ash
0.68	0	0	thick	0.25	–0.1	20	ash
0.70	0	20	ash	0.30	–0.1	30	ash
0.74	0	15	ash	0.35	–0.1	35	ash
0.76	0	5	ash	0.40	–0.1	45	ash
0.80	0	5	ash	0.45	–0.1	60	ash
0.85	0	5	ash	0.50	–0.1	60	ash
0.90	0	5	ash	0.55	–0.1	75	ash
0.95	0	10	ash	0.60	–0.1	20	ash
1.00	0	15	ash	0.62	–0.1	5	ash
				0.66	–0.1	5	ash
0.00	–0.1	1	ash	0.69	–0.1	15	ash
0.12	–0.1	1	ash	0.72	–0.1	15	ash
0.13	–0.1	10	ash	0.76	–0.1	10	ash
0.16	–0.1	20	ash	0.80	–0.1	10	ash
0.18	–0.1	10	ash	0.85	–0.1	15	ash
0.18	–0.1	0	soil	0.90	–0.1	20	ash
0.19	–0.1	0	soil	0.95	–0.1	15	ash
0.20	–0.1	1	ash	1.00	–0.1	1	ash
0.45	–0.1	1	ash				
0.46	–0.1	10	ash	0.00	–0.2	5	ash
0.48	–0.1	15	ash	0.05	–0.2	5	ash
0.50	–0.1	15	ash	0.10	–0.2	10	ash
0.52	–0.1	5	ash	0.15	–0.2	25	ash
0.54	–0.1	5	ash	0.20	–0.2	35	ash
0.55	–0.1	1	ash	0.22	–0.2	60	ash
0.66	–0.1	1	ash	0.25	–0.2	50	ash
0.69	–0.1	5	ash	0.28	–0.2	75	ash
0.71	–0.1	5	ash	0.32	–0.2	80	ash
0.73	–0.1	0	soil	0.36	–0.2	70	ash
0.74	–0.1	0	soil	0.40	–0.2	70	ash
0.75	–0.1	15	ash	0.45	–0.2	100	ash
0.77	–0.1	10	ash	0.50	–0.2	120	ash

Table 7. Ash thickness and surficial features in north-facing plots.—Continued

[Thickness between points should be interpolated linearly; m, meters; mm, millimeters]

Plot N13				Plot N15			
		Surface				Surface	
x (m)	y (m)	Ash thickness (mm)	Material	x (m)	y (m)	Ash thickness (mm)	Material
Average (mm)		10	Ash	Average (mm)		27	Ash
0.00	0	15	ash	0.00	0	30	ash
0.10	0	15	ash	0.10	0	40	ash
0.12	0	10	ash	0.20	0	40	ash
0.15	0	8	ash	0.30	0	45	ash
0.18	0	10	ash	0.40	0	40	ash
0.22	0	5	ash	0.50	0	25	ash
0.26	0	5	ash	0.60	0	20	ash
0.30	0	0	ash	0.70	0	25	ash
0.43	0	0	ash	0.80	0	30	ash
0.44	0	3	ash	0.90	0	30	ash
0.46	0	5	ash	1.00	0	30	ash
0.49	0	10	ash				
0.53	0	20	ash	0.00	–0.1	30	ash
0.57	0	15	ash	0.05	–0.1	30	ash
0.61	0	20	ash	0.10	–0.1	25	ash
0.62	0	0	burned	0.13	–0.1	10	ash
0.63	0	0	wood	0.16	–0.1	10	ash
0.64	0	0	40 mm	0.20	–0.1	10	ash
0.68	0	0	thick	0.25	–0.1	20	ash
0.70	0	20	ash	0.30	–0.1	30	ash
0.74	0	15	ash	0.35	–0.1	35	ash
0.76	0	5	ash	0.40	–0.1	45	ash
0.80	0	5	ash	0.45	–0.1	60	ash
0.85	0	5	ash	0.50	–0.1	60	ash
0.90	0	5	ash	0.55	–0.1	75	ash
0.95	0	10	ash	0.60	–0.1	20	ash
1.00	0	15	ash	0.62	–0.1	5	ash
				0.66	–0.1	5	ash
0.00	–0.1	1	ash	0.69	–0.1	15	ash
0.12	–0.1	1	ash	0.72	–0.1	15	ash
0.13	–0.1	10	ash	0.76	–0.1	10	ash
0.16	–0.1	20	ash	0.80	–0.1	10	ash
0.18	–0.1	10	ash	0.85	–0.1	15	ash
0.18	–0.1	0	soil	0.90	–0.1	20	ash
0.19	–0.1	0	soil	0.95	–0.1	15	ash
0.20	–0.1	1	ash	1.00	–0.1	1	ash
0.45	–0.1	1	ash				
0.46	–0.1	10	ash	0.00	–0.2	5	ash
0.48	–0.1	15	ash	0.05	–0.2	5	ash
0.50	–0.1	15	ash	0.10	–0.2	10	ash
0.52	–0.1	5	ash	0.15	–0.2	25	ash
0.54	–0.1	5	ash	0.20	–0.2	35	ash
0.55	–0.1	1	ash	0.22	–0.2	60	ash
0.66	–0.1	1	ash	0.25	–0.2	50	ash
0.69	–0.1	5	ash	0.28	–0.2	75	ash
0.71	–0.1	5	ash	0.32	–0.2	80	ash
0.73	–0.1	0	soil	0.36	–0.2	70	ash
0.74	–0.1	0	soil	0.40	–0.2	70	ash
0.75	–0.1	15	ash	0.45	–0.2	100	ash
0.77	–0.1	10	ash	0.50	–0.2	120	ash

Table 7. Ash thickness and surficial features in north-facing plots.—Continued

[Thickness between points should be interpolated linearly; m, meters; mm, millimeters]

Plot N13				Plot N15			
		Surface				Surface	
x (m)	y (m)	Ash thickness (mm)	Material	x (m)	y (m)	Ash thickness (mm)	Material
Average (mm)		10	Ash	Average (mm)		27	Ash
0.00	0	15	ash	0.00	0	30	ash
0.10	0	15	ash	0.10	0	40	ash
0.12	0	10	ash	0.20	0	40	ash
0.15	0	8	ash	0.30	0	45	ash
0.18	0	10	ash	0.40	0	40	ash
0.22	0	5	ash	0.50	0	25	ash
0.26	0	5	ash	0.60	0	20	ash
0.30	0	0	ash	0.70	0	25	ash
0.43	0	0	ash	0.80	0	30	ash
0.44	0	3	ash	0.90	0	30	ash
0.46	0	5	ash	1.00	0	30	ash
0.49	0	10	ash				
0.53	0	20	ash	0.00	–0.1	30	ash
0.57	0	15	ash	0.05	–0.1	30	ash
0.61	0	20	ash	0.10	–0.1	25	ash
0.62	0	0	burned	0.13	–0.1	10	ash
0.63	0	0	wood	0.16	–0.1	10	ash
0.64	0	0	40 mm	0.20	–0.1	10	ash
0.68	0	0	thick	0.25	–0.1	20	ash
0.70	0	20	ash	0.30	–0.1	30	ash
0.74	0	15	ash	0.35	–0.1	35	ash
0.76	0	5	ash	0.40	–0.1	45	ash
0.80	0	5	ash	0.45	–0.1	60	ash
0.85	0	5	ash	0.50	–0.1	60	ash
0.90	0	5	ash	0.55	–0.1	75	ash
0.95	0	10	ash	0.60	–0.1	20	ash
1.00	0	15	ash	0.62	–0.1	5	ash
				0.66	–0.1	5	ash
0.00	–0.1	1	ash	0.69	–0.1	15	ash
0.12	–0.1	1	ash	0.72	–0.1	15	ash
0.13	–0.1	10	ash	0.76	–0.1	10	ash
0.16	–0.1	20	ash	0.80	–0.1	10	ash
0.18	–0.1	10	ash	0.85	–0.1	15	ash
0.18	–0.1	0	soil	0.90	–0.1	20	ash
0.19	–0.1	0	soil	0.95	–0.1	15	ash
0.20	–0.1	1	ash	1.00	–0.1	1	ash
0.45	–0.1	1	ash				
0.46	–0.1	10	ash	0.00	–0.2	5	ash
0.48	–0.1	15	ash	0.05	–0.2	5	ash
0.50	–0.1	15	ash	0.10	–0.2	10	ash
0.52	–0.1	5	ash	0.15	–0.2	25	ash
0.54	–0.1	5	ash	0.20	–0.2	35	ash
0.55	–0.1	1	ash	0.22	–0.2	60	ash
0.66	–0.1	1	ash	0.25	–0.2	50	ash
0.69	–0.1	5	ash	0.28	–0.2	75	ash
0.71	–0.1	5	ash	0.32	–0.2	80	ash
0.73	–0.1	0	soil	0.36	–0.2	70	ash
0.74	–0.1	0	soil	0.40	–0.2	70	ash
0.75	–0.1	15	ash	0.45	–0.2	100	ash
0.77	–0.1	10	ash	0.50	–0.2	120	ash

Table 7. Ash thickness and surficial features in north-facing plots.—Continued

[Thickness between points should be interpolated linearly; m, meters; mm, millimeters]

Plot N13				Plot N15			
		Surface				Surface	
x (m)	y (m)	Ash thickness (mm)	Material	x (m)	y (m)	Ash thickness (mm)	Material
Average (mm)		10	Ash	Average (mm)		27	Ash
0.00	0	15	ash	0.00	0	30	ash
0.10	0	15	ash	0.10	0	40	ash
0.12	0	10	ash	0.20	0	40	ash
0.15	0	8	ash	0.30	0	45	ash
0.18	0	10	ash	0.40	0	40	ash
0.22	0	5	ash	0.50	0	25	ash
0.26	0	5	ash	0.60	0	20	ash
0.30	0	0	ash	0.70	0	25	ash
0.43	0	0	ash	0.80	0	30	ash
0.44	0	3	ash	0.90	0	30	ash
0.46	0	5	ash	1.00	0	30	ash
0.49	0	10	ash				
0.53	0	20	ash	0.00	–0.1	30	ash
0.57	0	15	ash	0.05	–0.1	30	ash
0.61	0	20	ash	0.10	–0.1	25	ash
0.62	0	0	burned	0.13	–0.1	10	ash
0.63	0	0	wood	0.16	–0.1	10	ash
0.64	0	0	40 mm	0.20	–0.1	10	ash
0.68	0	0	thick	0.25	–0.1	20	ash
0.70	0	20	ash	0.30	–0.1	30	ash
0.74	0	15	ash	0.35	–0.1	35	ash
0.76	0	5	ash	0.40	–0.1	45	ash
0.80	0	5	ash	0.45	–0.1	60	ash
0.85	0	5	ash	0.50	–0.1	60	ash
0.90	0	5	ash	0.55	–0.1	75	ash
0.95	0	10	ash	0.60	–0.1	20	ash
1.00	0	15	ash	0.62	–0.1	5	ash
				0.66	–0.1	5	ash
0.00	–0.1	1	ash	0.69	–0.1	15	ash
0.12	–0.1	1	ash	0.72	–0.1	15	ash
0.13	–0.1	10	ash	0.76	–0.1	10	ash
0.16	–0.1	20	ash	0.80	–0.1	10	ash
0.18	–0.1	10	ash	0.85	–0.1	15	ash
0.18	–0.1	0	soil	0.90	–0.1	20	ash
0.19	–0.1	0	soil	0.95	–0.1	15	ash
0.20	–0.1	1	ash	1.00	–0.1	1	ash
0.45	–0.1	1	ash				
0.46	–0.1	10	ash	0.00	–0.2	5	ash
0.48	–0.1	15	ash	0.05	–0.2	5	ash
0.50	–0.1	15	ash	0.10	–0.2	10	ash
0.52	–0.1	5	ash	0.15	–0.2	25	ash
0.54	–0.1	5	ash	0.20	–0.2	35	ash
0.55	–0.1	1	ash	0.22	–0.2	60	ash
0.66	–0.1	1	ash	0.25	–0.2	50	ash
0.69	–0.1	5	ash	0.28	–0.2	75	ash
0.71	–0.1	5	ash	0.32	–0.2	80	ash
0.73	–0.1	0	soil	0.36	–0.2	70	ash
0.74	–0.1	0	soil	0.40	–0.2	70	ash
0.75	–0.1	15	ash	0.45	–0.2	100	ash
0.77	–0.1	10	ash	0.50	–0.2	120	ash

Table 7. Ash thickness and surficial features in north-facing plots.—Continued

[Thickness between points should be interpolated linearly; m, meters; mm, millimeters]

Plot N13				Plot N15			
		Surface				Surface	
x (m)	y (m)	Ash thickness (mm)	Material	x (m)	y (m)	Ash thickness (mm)	Material
Average (mm)		10	Ash	Average (mm)		27	Ash
0.80	–0.1	15	ash	0.55	–0.2	120	ash
0.82	–0.1	15	ash	0.60	–0.2	90	ash
0.84	–0.1	5	ash	0.65	–0.2	60	ash
0.87	–0.1	0	soil	0.70	–0.2	70	ash
0.88	–0.1	0	soil	0.75	–0.2	60	ash
0.90	–0.1	10	ash	0.80	–0.2	60	ash
0.91	–0.1	15	ash	0.85	–0.2	50	ash
0.93	–0.1	15	ash	0.90	–0.2	30	ash
0.95	–0.1	10	ash	0.95	–0.2	30	ash
0.96	–0.1	0	tarp	1.00	–0.2	25	ash
1.00	–0.1	0	tarp				
0.00	–0.2	0	soil	0.05	–0.3	10	ash
0.08	–0.2	0	soil	0.10	–0.3	20	ash
0.09	–0.2	4	ash	0.13	–0.3	10	ash
0.10	–0.2	4	ash	0.15	–0.3	15	ash
0.11	–0.2	4	ash	0.17	–0.3	40	ash
0.12	–0.2	0	soil	0.20	–0.3	75	ash
0.28	–0.2	0	soil	0.24	–0.3	90	ash
0.30	–0.2	5	ash	0.27	–0.3	110	ash
0.32	–0.2	10	ash	0.30	–0.3	120	ash
0.35	–0.2	20	ash	0.33	–0.3	85	ash
0.37	–0.2	15	ash	0.36	–0.3	70	ash
0.39	–0.2	15	ash	0.40	–0.3	80	ash
0.44	–0.2	12	ash	0.43	–0.3	70	ash
0.45	–0.2	55	ash	0.47	–0.3	60	ash
0.48	–0.2	75	ash	0.50	–0.3	70	ash
0.51	–0.2	80	ash	0.55	–0.3	50	ash
0.52	–0.2	0	soil	0.60	–0.3	60	ash
0.64	–0.2	0	soil	0.65	–0.3	60	ash
0.65	–0.2	10	ash	0.70	–0.3	50	ash
0.68	–0.2	15	ash	0.75	–0.3	15	ash
0.70	–0.2	12	ash	0.80	–0.3	40	ash
0.73	–0.2	0	soil	0.85	–0.3	70	ash
0.75	–0.2	0	soil	0.87	–0.3	5	ash
0.76	–0.2	25	ash	0.90	–0.3	0	soil
0.78	–0.2	35	ash	0.93	–0.3	30	ash
0.80	–0.2	35	ash	0.96	–0.3	15	ash
0.82	–0.2	10	ash	1.00	–0.3	0	soil
0.85	–0.2	10	ash				
0.88	–0.2	10	ash	0.00	–0.4	20	ash
0.90	–0.2	5	ash	0.03	–0.4	20	ash
0.94	–0.2	5	ash	0.05	–0.4	20	ash
0.96	–0.2	0	tarp	0.08	–0.4	20	ash
1.00	–0.2	0	tarp	0.10	–0.4	20	ash
				0.12	–0.4	10	ash
0.00	–0.3	30	ash	0.15	–0.4	3	ash; root
0.04	–0.3	30	ash	0.19	–0.4	10	ash; root
0.05	–0.3	0	soil	0.20	–0.4	35	ash
0.25	–0.3	0	soil & hole	0.23	–0.4	50	ash

Table 7. Ash thickness and surficial features in north-facing plots.—Continued

[Thickness between points should be interpolated linearly; m, meters; mm, millimeters]

Plot N13				Plot N15			
		Surface				Surface	
x (m)	y (m)	Ash thickness (mm)	Material	x (m)	y (m)	Ash thickness (mm)	Material
Average (mm)		10	Ash	Average (mm)		27	Ash
0.28	–0.3	15	ash	0.26	–0.4	50	ash
0.30	–0.3	15	ash & hole	0.29	–0.4	50	ash
0.31	–0.3	0	soil	0.32	–0.4	60	ash
0.47	–0.3	0	soil	0.35	–0.4	60	ash
0.49	–0.3	15	ash	0.38	–0.4	50	ash
0.52	–0.3	0	soil	0.40	–0.4	35	ash
0.53	–0.3	1	ash	0.43	–0.4	15	ash
0.85	–0.3	1	ash	0.46	–0.4	10	ash
0.86	–0.3	15	ash	0.50	–0.4	10	ash
0.87	–0.3	15	ash	0.52	–0.4	5	ash
0.88	–0.3	15	hole	0.55	–0.4	5	ash
0.89	–0.3	15	ash	0.57	–0.4	20	ash
0.90	–0.3	15	ash	0.60	–0.4	30	ash
0.91	–0.3	15	ash	0.63	–0.4	50	ash
0.92	–0.3	15	ash	0.68	–0.4	70	ash
0.93	–0.3	0	fill	0.70	–0.4	50	ash
0.96	–0.3	0	fill	0.73	–0.4	25	ash
0.97	–0.3	0	tarp	0.78	–0.4	20	ash
1.00	–0.3	0	tarp	0.80	–0.4	25	ash
				0.84	–0.4	15	ash
0.00	–0.4	10	ash	0.86	–0.4	15	ash
0.05	–0.4	15	ash	0.88	–0.4	25	ash
0.07	–0.4	20	ash	0.91	–0.4	30	ash
0.08	–0.4	0	soil	0.94	–0.4	25	ash
0.10	–0.4	0	soil	0.97	–0.4	20	ash
0.17	–0.4	2	ash	1.00	–0.4	30	ash
0.20	–0.4	2	ash				
0.21	–0.4	0	soil	0.00	–0.5	5	ash
0.22	–0.4	0	soil	0.05	–0.5	10	ash
0.23	–0.4	10	ash	0.08	–0.5	15	ash
0.26	–0.4	30	ash	0.10	–0.5	20	ash
0.30	–0.4	30	ash	0.13	–0.5	20	ash
0.33	–0.4	30	ash	0.16	–0.5	0	root
0.36	–0.4	20	ash	0.21	–0.5	0	root
0.37	–0.4	0	ash	0.22	–0.5	40	ash
0.38	–0.4	0	ash	0.25	–0.5	40	ash
0.43	–0.4	20	ash	0.30	–0.5	20	ash
0.55	–0.4	20	ash	0.33	–0.5	20	ash
0.56	–0.4	0	ash	0.36	–0.5	25	ash
0.80	–0.4	0	ash	0.40	–0.5	15	ash
0.81	–0.4	10	ash	0.43	–0.5	5	ash
0.90	–0.4	10	ash	0.46	–0.5	3	ash
0.91	–0.4	0	fill	0.49	–0.5	2	ash
0.94	–0.4	0	fill	0.52	–0.5	10	ash
0.95	–0.4	0	fill & tarp	0.56	–0.5	10	ash
1.00	–0.4	0	fill & tarp	0.60	–0.5	10	ash
				0.64	–0.5	20	ash
0.00	–0.5	2	ash	0.68	–0.5	5	ash
0.07	–0.5	2	ash	0.71	–0.5	20	ash
0.09	–0.5	10	ash	0.75	–0.5	30	ash

Table 7. Ash thickness and surficial features in north-facing plots.—Continued

[Thickness between points should be interpolated linearly; m, meters; mm, millimeters]

Plot N13				Plot N15			
		Surface				Surface	
x (m)	y (m)	Ash thickness (mm)	Material	x (m)	y (m)	Ash thickness (mm)	Material
Average (mm)		10	Ash	Average (mm)		27	Ash
0.11	–0.5	20	ash	0.78	–0.5	30	ash
0.13	–0.5	10	ash	0.81	–0.5	20	ash
0.13	–0.5	0	soil	0.84	–0.5	30	ash
0.14	–0.5	0	soil	0.87	–0.5	30	ash
0.15	–0.5	0.5	ash	0.90	–0.5	50	ash
0.30	–0.5	0.5	ash	0.94	–0.5	35	ash
0.32	–0.5	10	ash	0.97	–0.5	20	ash
0.34	–0.5	10	ash	0.99	–0.5	10	ash
0.38	–0.5	20	ash				
0.40	–0.5	30	ash	0.00	–0.6	10	ash
0.42	–0.5	30	ash	0.04	–0.6	10	ash
0.44	–0.5	40	ash	0.07	–0.6	25	ash
0.46	–0.5	60	ash	0.10	–0.6	25	ash
0.48	–0.5	40	ash	0.13	–0.6	25	ash
0.50	–0.5	10	ash	0.16	–0.6	15	ash
0.52	–0.5	0	soil	0.18	–0.6	15	ash
0.90	–0.5	0	soil	0.20	–0.6	5	ash
0.91	–0.5	8	ash	0.21	–0.6	5	ash
0.92	–0.5	8	ash	0.22	–0.6	20	ash
0.93	–0.5	8	ash	0.23	–0.6	30	ash
0.94	–0.5	8	ash	0.25	–0.6	35	ash
0.95	–0.5	0	tarp	0.27	–0.6	40	ash
1.00	–0.5	0	tarp	0.30	–0.6	20	ash
				0.33	–0.6	8	ash
0.00	–0.6	5	ash	0.36	–0.6	10	ash
0.15	–0.6	5	ash	0.39	–0.6	10	ash
0.18	–0.6	20	ash	0.41	–0.6	10	ash
0.20	–0.6	35	ash	0.44	–0.6	5	ash
0.23	–0.6	50	ash	0.45	–0.6	0	soil
0.27	–0.6	50	ash	0.50	–0.6	0	soil
0.30	–0.6	50	ash	0.52	–0.6	5	ash
0.34	–0.6	10	ash	0.55	–0.6	5	ash
0.35	–0.6	1	ash	0.59	–0.6	5	ash
0.55	–0.6	1	ash	0.62	–0.6	5	ash
0.56	–0.6	0	soil	0.67	–0.6	5	ash
0.70	–0.6	0	soil	0.70	–0.6	20	ash
0.73	–0.6	5	ash	0.73	–0.6	30	ash
0.76	–0.6	5	ash	0.76	–0.6	25	ash
0.80	–0.6	5	ash	0.79	–0.6	25	ash; glass
0.85	–0.6	5	ash	0.82	–0.6	15	ash
0.87	–0.6	0	root	0.85	–0.6	5	ash
0.88	–0.6	0	fill	0.87	–0.6	10	ash
0.94	–0.6	0	fill	0.90	–0.6	5	ash
0.95	–0.6	0	fill & tarp	0.93	–0.6	5	ash
1.00	–0.6	0	fill & tarp	0.95	–0.6	10	ash
				0.98	–0.6	25	ash
0.00	–0.7	2	ash	1.00	–0.6	30	ash
0.12	–0.7	2	ash				
0.13	–0.7	0	soil	0.00	–0.7	50	ash
0.20	–0.7	0	soil	0.04	–0.7	60	ash

Table 7. Ash thickness and surficial features in north-facing plots.—Continued

[Thickness between points should be interpolated linearly; m, meters; mm, millimeters]

Plot N13				Plot N15			
		Surface				Surface	
x (m)	y (m)	Ash thickness (mm)	Material	x (m)	y (m)	Ash thickness (mm)	Material
Average (mm)		10	Ash	Average (mm)		27	Ash
0.23	–0.7	15	ash	0.08	–0.7	80	ash
0.27	–0.7	10	ash	0.11	–0.7	90	ash
0.32	–0.7	10	ash	0.12	–0.7	50	ash
0.35	–0.7	10	ash	0.13	–0.7	20	ash
0.40	–0.7	10	ash	0.14	–0.7	15	ash
0.43	–0.7	30	ash	0.16	–0.7	10	ash
0.47	–0.7	30	ash	0.18	–0.7	10	ash
0.50	–0.7	30	ash	0.20	–0.7	10	ash
0.55	–0.7	25	ash	0.22	–0.7	5	ash
0.60	–0.7	20	ash	0.24	–0.7	2	ash
0.65	–0.7	25	ash	0.25	–0.7	5	ash
0.70	–0.7	1	ash	0.27	–0.7	15	ash
0.71	–0.7	2	ash	0.28	–0.7	30	ash
0.80	–0.7	2	ash	0.30	–0.7	40	ash
0.81	–0.7	1	ash	0.32	–0.7	45	ash
0.90	–0.7	1	ash	0.34	–0.7	40	ash
0.91	–0.7	0	soil	0.36	–0.7	40	ash
0.96	–0.7	0	soil	0.38	–0.7	30	ash
0.97	–0.7	0	tarp	0.40	–0.7	35	ash
1.00	–0.7	0	tarp	0.42	–0.7	30	ash
				0.44	–0.7	20	ash
0.00	–0.8	0	fill	0.46	–0.7	5	ash
0.15	–0.8	0	fill	0.48	–0.7	1	ash
0.16	–0.8	2	ash	0.51	–0.7	0	soil
0.20	–0.8	2	ash	0.52	–0.7	0	soil
0.21	–0.8	3	ash	0.55	–0.7	0	soil
0.35	–0.8	3	ash	0.57	–0.7	5	ash
0.40	–0.8	10	ash	0.60	–0.7	10	ash
0.45	–0.8	15	ash	0.63	–0.7	15	ash
0.50	–0.8	18	ash	0.67	–0.7	20	ash
0.55	–0.8	10	ash	0.70	–0.7	15	ash
0.60	–0.8	10	ash	0.74	–0.7	40	ash
0.65	–0.8	5	ash	0.79	–0.7	50	ash
0.66	–0.8	2	ash	0.84	–0.7	60	ash
0.74	–0.8	2	ash	0.87	–0.7	50	ash
0.75	–0.8	20	ash	0.91	–0.7	25	ash
0.78	–0.8	15	ash	0.94	–0.7	20	ash
0.80	–0.8	10	ash	0.98	–0.7	30	ash
0.85	–0.8	10	ash	1.00	–0.7	30	ash
0.90	–0.8	0	ash				
0.95	–0.8	5	ash	0.00	–0.8	60	ash
0.96	–0.8	0	tarp	0.04	–0.8	70	ash
1.00	–0.8	0	tarp	0.08	–0.8	80	ash
				0.10	–0.8	60	ash
0.00	–0.9	0	fill	0.13	–0.8	30	ash
0.15	–0.9	0	fill	0.17	–0.8	10	ash
0.45	–0.9	0	fill	0.20	–0.8	5	ash
0.50	–0.9	5	ash	0.23	–0.8	5	ash
0.55	–0.9	10	ash	0.26	–0.8	5	ash
0.60	–0.9	15	ash	0.29	–0.8	15	ash

Table 7. Ash thickness and surficial features in north-facing plots.—Continued

[Thickness between points should be interpolated linearly; m, meters; mm, millimeters]

Plot N13				Plot N15			
		Surface				Surface	
x (m)	y (m)	Ash thickness (mm)	Material	x (m)	y (m)	Ash thickness (mm)	Material
Average (mm)		10	Ash	Average (mm)		27	Ash
0.65	–0.9	15	ash	0.32	–0.8	25	ash
0.70	–0.9	10	ash	0.35	–0.8	30	ash
0.75	–0.9	8	ash	0.38	–0.8	20	ash
0.80	–0.9	10	ash	0.41	–0.8	15	ash
0.85	–0.9	20	ash	0.44	–0.8	10	ash
0.90	–0.9	15	ash	0.47	–0.8	5	ash
0.95	–0.9	25	ash	0.51	–0.8	2	ash
0.97	–0.9	20	ash	0.55	–0.8	0	soil
1.00	–0.9	15	ash	0.57	–0.8	0	soil
				0.58	–0.8	10	ash
				0.62	–0.8	10	ash
				0.65	–0.8	5	ash
				0.75	–0.8	1	ash
				0.76	–0.8	0	stump
				0.84	–0.8	0	stump
				0.85	–0.8	25	ash; bone
				0.88	–0.8	60	ash; bone
				0.92	–0.8	80	ash; bone
				0.96	–0.8	60	ash
				1.00	–0.8	15	ash
				0.00	–0.9	0	soil
				0.05	–0.9	0	soil
				0.08	–0.9	25	ash
				0.11	–0.9	30	ash
				0.13	–0.9	15	ash
				0.15	–0.9	10	ash
				0.17	–0.9	2	ash
				0.20	–0.9	3	ash
				0.24	–0.9	3	ash
				0.27	–0.9	10	ash
				0.30	–0.9	15	ash
				0.33	–0.9	20	ash
				0.35	–0.9	20	ash
				0.38	–0.9	8	ash
				0.40	–0.9	15	ash
				0.43	–0.9	40	ash
				0.46	–0.9	30	ash
				0.50	–0.9	15	ash
				0.54	–0.9	20	ash
				0.57	–0.9	10	ash
				0.58	–0.9	0	soil
				0.70	–0.9	0	soil
				0.73	–0.9	20	ash
				0.77	–0.9	30	ash
				0.78	–0.9	0	stump
				0.90	–0.9	0	stump
				0.93	–0.9	20	ash
				0.97	–0.9	30	ash
				1.00	–0.9	0	soil

Table 8. Ash thickness and surficial features in south-facing plots.

[Thickness between points should be interpolated linearly; m, meters; mm, millimeters]

Plot S13				Plot S15			
		Surface				Surface	
x (m)	y (m)	Ash thickness (mm)	Material	x (m)	y (m)	Ash thickness (mm)	Material
Average (mm)		22	Ash	Average (mm)		9	Ash
0.00	–0.1	0	soil	0.00	–0.1	5	ash
0.11	–0.1	0	soil	0.04	–0.1	10	ash
0.12	–0.1	0	soil/fungus	0.06	–0.1	20	ash
0.13	–0.1	0	fungus	0.06	–0.1	0	soil
0.24	–0.1	0	fungus	0.11	–0.1	0	soil
0.25	–0.1	5	ash	0.13	–0.1	20	ash
0.27	–0.1	5	ash	0.16	–0.1	25	ash
0.30	–0.1	15	ash	0.18	–0.1	30	ash
0.31	–0.1	0	rock	0.20	–0.1	30	ash
0.36	–0.1	0	rock	0.22	–0.1	25	ash
0.36	–0.1	3	ash	0.25	–0.1	25	ash
0.39	–0.1	5	ash	0.27	–0.1	25	ash
0.44	–0.1	2	ash	0.30	–0.1	20	ash
0.46	–0.1	3	ash	0.33	–0.1	15	ash
0.51	–0.1	10	ash	0.35	–0.1	10	ash
0.54	–0.1	15	ash	0.37	–0.1	10	ash
0.56	–0.1	3	ash	0.39	–0.1	10	ash
0.56	–0.1	0	soil	0.41	–0.1	10	ash
0.66	–0.1	0	soil	0.43	–0.1	20	ash
0.67	–0.1	0	rock	0.45	–0.1	15	ash
0.81	–0.1	0	rock	0.47	–0.1	28	ash
0.82	–0.1	5	ash	0.49	–0.1	28	ash
0.86	–0.1	15	ash	0.51	–0.1	28	ash
0.89	–0.1	20	ash	0.53	–0.1	30	ash
0.92	–0.1	18	ash	0.55	–0.1	25	ash
0.95	–0.1	20	ash	0.57	–0.1	15	ash
0.97	–0.1	15	ash	0.58	–0.1	0	soil
1.00	–0.1	20	ash	0.59	–0.1	0	soil
				0.61	–0.1	0	soil
0.00	–0.2	0	soil	0.62	–0.1	10	ash
0.04	–0.2	0	soil	0.63	–0.1	15	ash
0.05	–0.2	15	ash	0.64	–0.1	10	ash
0.08	–0.2	20	ash	0.66	–0.1	10	ash
0.10	–0.2	25	ash	0.68	–0.1	5	ash
0.12	–0.2	20	ash	0.70	–0.1	10	ash
0.13	–0.2	10	ash	0.72	–0.1	15	ash
0.14	–0.2	0	soil	0.74	–0.1	10	ash
0.15	–0.2	0	soil	0.76	–0.1	5	ash

Table 8. Ash thickness and surficial features in south-facing plots.—Continued

[Thickness between points should be interpolated linearly; m, meters; mm, millimeters]

Plot S13				Plot S15			
		Surface				Surface	
x (m)	y (m)	Ash thickness (mm)	Material	x (m)	y (m)	Ash thickness (mm)	Material
Average (mm)		22	Ash	Average (mm)		9	Ash
0.16	–0.2	0	soil	0.79	–0.1	18	ash
0.17	–0.2	0	soil/fungus	0.82	–0.1	20	ash
0.18	–0.2	0	fungus	0.85	–0.1	23	ash
0.27	–0.2	0	fungus/soil	0.89	–0.1	15	ash
0.28	–0.2	0	soil	0.89	–0.1	0	soil
0.32	–0.2	0	soil	1.00	–0.1	0	soil
0.32	–0.2	10	ash				
0.35	–0.2	30	ash	0.00	–0.2	0	soil
0.38	–0.2	30	ash	0.18	–0.2	5	ash
0.41	–0.2	23	ash	0.21	–0.2	10	ash
0.43	–0.2	10	ash	0.23	–0.2	5	ash
0.45	–0.2	0	rock	0.24	–0.2	5	ash
0.56	–0.2	0	rock	0.26	–0.2	20	ash
0.56	–0.2	35	ash	0.28	–0.2	28	ash
0.60	–0.2	25	ash	0.30	–0.2	30	ash
0.63	–0.2	20	ash	0.32	–0.2	20	ash
0.65	–0.2	10	ash	0.46	–0.2	5	ash
0.69	–0.2	20	ash	0.49	–0.2	8	ash
0.73	–0.2	28	ash	0.51	–0.2	14	ash
0.77	–0.2	20	ash	0.54	–0.2	18	ash
0.80	–0.2	20	ash	0.57	–0.2	0	soil
0.83	–0.2	18	ash	0.64	–0.2	0	soil
0.88	–0.2	20	ash	0.65	–0.2	5	ash
0.90	–0.2	20	ash	0.67	–0.2	20	ash
0.94	–0.2	30	ash	0.70	–0.2	25	ash
0.97	–0.2	50	ash	0.72	–0.2	24	ash
0.99	–0.2	50	ash	0.76	–0.2	20	ash
1.00	–0.2	30	ash	0.79	–0.2	20	ash
				0.82	–0.2	20	ash
0.00	–0.3	0	soil	0.85	–0.2	20	ash
0.01	–0.3	0	soil/rock	0.89	–0.2	20	ash
0.02	–0.3	0	rock	0.89	–0.2	0	soil
0.09	–0.3	0	rock/soil	1.00	–0.2	0	soil
0.10	–0.3	0	soil				
0.21	–0.3	0	soil/fungus	0.04	–0.3	20	ash
0.22	–0.3	0	fungus	0.06	–0.3	30	ash
0.25	–0.3	0	fungus	0.09	–0.3	20	ash

Table 8. Ash thickness and surficial features in south-facing plots.—Continued

[Thickness between points should be interpolated linearly; m, meters; mm, millimeters]

Plot S13				Plot S15			
		Surface				Surface	
x (m)	y (m)	Ash thickness (mm)	Material	x (m)	y (m)	Ash thickness (mm)	Material
Average (mm)		22	Ash	Average (mm)		9	Ash
0.26	–0.3	0	soil	0.13	–0.3	0	soil
0.30	–0.3	20	ash	0.25	–0.3	0	soil
0.33	–0.3	25	ash	0.28	–0.3	2	ash
0.36	–0.3	45	ash	0.30	–0.3	10	ash
0.39	–0.3	65	ash	0.32	–0.3	10	ash
0.41	–0.3	60	ash	0.34	–0.3	14	ash
0.42	–0.3	45	ash	0.36	–0.3	12	ash
0.46	–0.3	25	ash	0.38	–0.3	10	ash
0.49	–0.3	20	ash	0.40	–0.3	3	ash
0.51	–0.3	30	ash	0.42	–0.3	18	ash
0.53	–0.3	35	ash	0.44	–0.3	20	ash
0.56	–0.3	45	ash	0.46	–0.3	26	ash
0.59	–0.3	30	ash	0.48	–0.3	30	ash
0.61	–0.3	20	ash	0.50	–0.3	25	ash
0.64	–0.3	10	ash	0.52	–0.3	25	ash
0.65	–0.3	0	rock	0.55	–0.3	10	ash
0.71	–0.3	0	rock	0.55	–0.3	0	soil
0.71	–0.3	30	ash	0.60	–0.3	0	soil
0.74	–0.3	40	ash	0.60	–0.3	15	ash
0.77	–0.3	35	ash	0.62	–0.3	32	ash
0.80	–0.3	30	ash	0.65	–0.3	28	ash
0.83	–0.3	20	ash	0.67	–0.3	20	ash
0.85	–0.3	30	ash	0.69	–0.3	10	ash
0.88	–0.3	30	ash	0.73	–0.3	5	ash
0.90	–0.3	30	ash	0.75	–0.3	5	ash
0.93	–0.3	40	ash	0.77	–0.3	5	ash
0.96	–0.3	45	ash	0.79	–0.3	5	ash
1.00	–0.3	20	ash	0.81	–0.3	10	ash
				0.83	–0.3	20	ash
0.00	–0.4	0	soil	0.85	–0.3	20	ash
0.03	–0.4	0	soil	0.87	–0.3	20	ash
0.03	–0.4	35	ash	0.89	–0.3	0	soil
0.06	–0.4	40	ash	1.00	–0.3	0	soil
0.09	–0.4	40	ash				
0.11	–0.4	30	ash	0.00	–0.4	0	soil
0.13	–0.4	20	ash	0.30	–0.4	0	soil
0.15	–0.4	10	ash	0.30	–0.4	1	ash

Table 8. Ash thickness and surficial features in south-facing plots.—Continued

[Thickness between points should be interpolated linearly; m, meters; mm, millimeters]

Plot S13				Plot S15			
		Surface				Surface	
x (m)	y (m)	Ash thickness (mm)	Material	x (m)	y (m)	Ash thickness (mm)	Material
Average (mm)		22	Ash	Average (mm)		9	Ash
0.16	–0.4	0	soil	0.32	–0.4	3	ash
0.20	–0.4	0	soil	0.34	–0.4	10	ash
0.21	–0.4	0	fungus	0.36	–0.4	10	ash
0.25	–0.4	0	fungus	0.38	–0.4	10	ash
0.26	–0.4	0	rock	0.40	–0.4	5	ash
0.27	–0.4	0	rock	0.42	–0.4	10	ash
0.28	–0.4	0	rock	0.44	–0.4	18	ash
0.29	–0.4	0	rock	0.46	–0.4	20	ash
0.30	–0.4	3	ash	0.48	–0.4	20	ash
0.32	–0.4	30	ash	0.50	–0.4	24	ash
0.33	–0.4	0	rock	0.53	–0.4	20	ash
0.45	–0.4	0	rock/soil	0.53	–0.4	0	soil
0.46	–0.4	0	soil/rock	0.61	–0.4	0	soil
0.47	–0.4	0	rock	0.61	–0.4	10	ash
0.48	–0.4	0	rock	0.62	–0.4	20	ash
0.58	–0.4	0	rock/soil	0.64	–0.4	30	ash
0.59	–0.4	0	soil	0.66	–0.4	30	ash
0.67	–0.4	0	soil	0.68	–0.4	30	ash
0.68	–0.4	40	ash	0.70	–0.4	24	ash
0.70	–0.4	50	ash	0.72	–0.4	20	ash
0.74	–0.4	50	ash	0.74	–0.4	16	ash
0.77	–0.4	45	ash	0.76	–0.4	18	ash
0.80	–0.4	40	ash	0.78	–0.4	18	ash
0.84	–0.4	40	ash	0.80	–0.4	14	ash
0.86	–0.4	50	ash	0.82	–0.4	10	ash
0.88	–0.4	60	ash	0.84	–0.4	10	ash
0.90	–0.4	50	ash	0.86	–0.4	12	ash
0.92	–0.4	45	ash	0.88	–0.4	10	ash
0.94	–0.4	45	ash	0.90	–0.4	0	soil
0.96	–0.4	40	ash	1.00	–0.4	0	soil
0.98	–0.4	20	ash				
1.00	–0.4	24	ash	0.02	–0.5	0	soil
				0.04	–0.5	10	ash
0.00	–0.5	0	soil	0.06	–0.5	8	ash
0.06	–0.5	0	soil	0.08	–0.5	4	ash
0.06	–0.5	20	ash	0.10	–0.5	0	soil
0.08	–0.5	15	ash	0.21	–0.5	0	soil
0.10	–0.5	20	ash	0.22	–0.5	1	ash

Table 8. Ash thickness and surficial features in south-facing plots.—Continued

[Thickness between points should be interpolated linearly; m, meters; mm, millimeters]

Plot S13				Plot S15			
		Surface				Surface	
x (m)	y (m)	Ash thickness (mm)	Material	x (m)	y (m)	Ash thickness (mm)	Material
Average (mm)		22	Ash	Average (mm)		9	Ash
0.12	–0.5	10	ash	0.48	–0.5	1	ash
0.13	–0.5	0	soil	0.48	–0.5	0	soil
0.33	–0.5	0	soil	0.58	–0.5	0	soil
0.33	–0.5	50	ash	0.58	–0.5	2	ash
0.36	–0.5	55	ash	0.60	–0.5	20	ash
0.37	–0.5	45	ash	0.64	–0.5	20	ash
0.39	–0.5	40	ash	0.66	–0.5	20	ash
0.41	–0.5	40	ash	0.68	–0.5	12	ash
0.43	–0.5	40	ash	0.70	–0.5	8	ash
0.46	–0.5	40	ash	0.72	–0.5	5	ash
0.49	–0.5	45	ash	0.74	–0.5	5	ash
0.51	–0.5	40	ash	0.76	–0.5	8	ash
0.54	–0.5	45	ash	0.78	–0.5	8	ash
0.57	–0.5	50	ash	0.80	–0.5	10	ash
0.59	–0.5	57	ash	0.82	–0.5	10	ash
0.62	–0.5	50	ash	0.84	–0.5	5	ash
0.65	–0.5	38	ash	0.87	–0.5	0	soil
0.67	–0.5	10	ash	1.00	–0.5	0	soil
0.70	–0.5	0	rock				
0.73	–0.5	5	ash	0.00	–0.6	0	soil
0.75	–0.5	15	ash	0.02	–0.6	15	ash
0.77	–0.5	28	ash	0.04	–0.6	10	ash
0.80	–0.5	40	ash	0.06	–0.6	5	ash
0.82	–0.5	18	ash	0.07	–0.6	0	soil
0.84	–0.5	18	ash	0.28	–0.6	0	soil
0.86	–0.5	20	ash	0.30	–0.6	2	ash
0.87	–0.5	3	ash	0.32	–0.6	5	ash
0.88	–0.5	0	rock	0.36	–0.6	5	ash
0.89	–0.5	0	rock	0.38	–0.6	5	ash
0.90	–0.5	0	rock	0.40	–0.6	8	ash
0.91	–0.5	5	ash	0.42	–0.6	10	ash
0.92	–0.5	38	ash	0.44	–0.6	10	ash
0.94	–0.5	35	ash	0.46	–0.6	10	ash
0.96	–0.5	35	ash	0.48	–0.6	4	ash
0.98	–0.5	35	ash	0.50	–0.6	2	ash
1.00	–0.5	25	ash	0.52	–0.6	5	ash
				0.54	–0.6	10	ash
0.00	–0.6	0	soil	0.56	–0.6	10	ash

Table 8. Ash thickness and surficial features in south-facing plots.—Continued

[Thickness between points should be interpolated linearly; m, meters; mm, millimeters]

Plot S13				Plot S15			
		Surface				Surface	
x (m)	y (m)	Ash thickness (mm)	Material	x (m)	y (m)	Ash thickness (mm)	Material
Average (mm)		22	Ash	Average (mm)		9	Ash
0.10	–0.6	0	soil	0.58	–0.6	6	ash
0.10	–0.6	10	ash	0.60	–0.6	5	ash
0.12	–0.6	20	ash	0.62	–0.6	2	ash
0.13	–0.6	15	ash	0.66	–0.6	1	ash
0.14	–0.6	0	soil	0.68	–0.6	0	soil
0.22	–0.6	0	soil	0.73	–0.6	0	soil
0.23	–0.6	0	soil/rock	0.74	–0.6	4	ash + 2mm diameter gravel
0.24	–0.6	0	rock/soil	0.76	–0.6	10	ash + 2mm diameter gravel
0.35	–0.6	0	soil	0.77	–0.6	8	ash + 2mm diameter gravel
0.36	–0.6	0	soil	0.80	–0.6	3	ash + 2mm diameter gravel
0.41	–0.6	0	soil	0.83	–0.6	3	ash + 2mm diameter gravel
0.42	–0.6	40	ash	0.86	–0.6	3	ash + 2mm diameter gravel
0.44	–0.6	60	ash	0.89	–0.6	0	soil
0.46	–0.6	50	ash	1.00	–0.6	0	soil
0.48	–0.6	45	ash				
0.50	–0.6	40	ash	0.00	–0.7	15	ash
0.52	–0.6	50	ash	0.03	–0.7	15	ash
0.54	–0.6	64	ash	0.04	–0.7	0	soil
0.56	–0.6	65	ash	0.23	–0.7	0	soil
0.58	–0.6	65	ash	0.24	–0.7	2	ash
0.60	–0.6	70	ash	0.26	–0.7	5	ash
0.62	–0.6	70	ash	0.28	–0.7	10	ash
0.66	–0.6	0	rock	0.30	–0.7	4	ash
0.82	–0.6	0	rock	0.32	–0.7	5	ash
0.83	–0.6	10	ash	0.34	–0.7	5	ash
0.86	–0.6	10	ash	0.36	–0.7	10	ash
0.87	–0.6	20	ash	0.38	–0.7	10	ash
0.89	–0.6	20	ash	0.40	–0.7	10	ash
0.92	–0.6	15	ash	0.42	–0.7	5	ash
0.94	–0.6	25	ash	0.44	–0.7	2	ash
0.97	–0.6	10	ash	0.46	–0.7	5	ash
1.00	–0.6	10	ash	0.48	–0.7	10	ash
				0.50	–0.7	10	ash
0.00	–0.7	0	soil	0.52	–0.7	5	ash
0.10	–0.7	0	soil	0.54	–0.7	3	ash
0.11	–0.7	15	ash	0.56	–0.7	2	ash
0.12	–0.7	15	ash	0.58	–0.7	5	ash
0.13	–0.7	20	ash	0.60	–0.7	5	ash

Table 8. Ash thickness and surficial features in south-facing plots.—Continued

[Thickness between points should be interpolated linearly; m, meters; mm, millimeters]

Plot S13				Plot S15			
		Surface				Surface	
x (m)	y (m)	Ash thickness (mm)	Material	x (m)	y (m)	Ash thickness (mm)	Material
Average (mm)		22	Ash	Average (mm)		9	Ash
0.14	–0.7	5	ash	0.62	–0.7	5	ash
0.15	–0.7	0	soil	0.64	–0.7	7	ash
0.21	–0.7	0	soil	0.66	–0.7	0	soil
0.22	–0.7	0	rock	0.76	–0.7	0	soil
0.30	–0.7	0	rock	0.78	–0.7	2	ash
0.31	–0.7	0	soil	0.80	–0.7	2	ash
0.41	–0.7	0	soil	0.82	–0.7	2	ash
0.42	–0.7	0	soil	0.84	–0.7	5	ash
0.43	–0.7	40	ash	0.86	–0.7	5	ash
0.45	–0.7	35	ash	0.88	–0.7	0	soil
0.48	–0.7	45	ash	1.00	–0.7	0	soil
0.50	–0.7	45	ash				
0.52	–0.7	40	ash	0.00	–0.8	10	ash
0.54	–0.7	30	ash	0.04	–0.8	10	ash
0.56	–0.7	28	ash	0.04	–0.8	0	soil
0.58	–0.7	24	ash	0.08	–0.8	0	soil
0.60	–0.7	20	ash	0.08	–0.8	2	ash
0.62	–0.7	20	ash	0.13	–0.8	2	ash
0.64	–0.7	40	ash	0.13	–0.8	0	soil
0.66	–0.7	45	ash; rill B	0.24	–0.8	0	soil
0.69	–0.7	45	ash	0.25	–0.8	5	ash
0.71	–0.7	50	ash	0.27	–0.8	15	ash
0.77	–0.7	50	ash	0.29	–0.8	15	ash
0.80	–0.7	40	ash	0.31	–0.8	3	ash
0.83	–0.7	40	ash	0.34	–0.8	5	ash
0.86	–0.7	45	ash	0.37	–0.8	5	ash
0.89	–0.7	40	ash	0.40	–0.8	3	ash
0.92	–0.7	45	ash	0.43	–0.8	5	ash
0.95	–0.7	45	ash	0.46	–0.8	5	ash
0.97	–0.7	40	ash	0.49	–0.8	3	ash
0.99	–0.7	15	ash	0.51	–0.8	1	ash
				0.54	–0.8	1	ash
0.00	–0.8	0	soil	0.57	–0.8	1	ash
0.44	–0.8	0	soil/ash	0.60	–0.8	3	ash
0.44	–0.8	20	ash	0.62	–0.8	3	ash
0.48	–0.8	45	ash	0.64	–0.8	0	soil
0.50	–0.8	40	ash	0.77	–0.8	0	soil

Table 8. Ash thickness and surficial features in south-facing plots.—Continued

[Thickness between points should be interpolated linearly; m, meters; mm, millimeters]

Plot S13				Plot S15			
		Surface				Surface	
x (m)	y (m)	Ash thickness (mm)	Material	x (m)	y (m)	Ash thickness (mm)	Material
Average (mm)		22	Ash	Average (mm)		9	Ash
0.53	–0.8	40	ash	0.79	–0.8	1	ash
0.54	–0.8	15	ash	0.82	–0.8	3	ash
0.57	–0.8	0	rock	0.85	–0.8	3	ash
0.68	–0.8	0	rock	0.88	–0.8	3	ash
0.69	–0.8	25	ash	0.91	–0.8	0	soil
0.72	–0.8	45	ash	0.98	–0.8	0	soil
0.75	–0.8	30	ash				
0.77	–0.8	20	ash; rill B	0.00	–0.9	0	soil
0.80	–0.8	25	ash	0.25	–0.9	0	soil
0.83	–0.8	35	ash	0.25	–0.9	3	ash
0.86	–0.8	30	ash	0.30	–0.9	5	ash
0.88	–0.8	40	ash	0.35	–0.9	10	ash
0.90	–0.8	35	ash	0.40	–0.9	5	ash
0.94	–0.8	55	ash	0.45	–0.9	5	ash
0.96	–0.8	48	ash	0.50	–0.9	10	ash
1.00	–0.8	38	ash	0.55	–0.9	15	ash
				0.65	–0.9	0	soil
0.00	–0.9	0	soil	0.73	–0.9	0	soil
0.43	–0.9	0	soil	0.73	–0.9	10	ash
0.44	–0.9	25	ash	0.80	–0.9	5	ash
0.49	–0.9	15	ash	0.85	–0.9	10	ash
0.52	–0.9	30	ash	0.90	–0.9	5	ash
0.55	–0.9	50	ash	0.98	–0.9	0	ash
0.60	–0.9	60	ash	1.00	–0.9	0	ash
0.65	–0.9	55	ash				
0.68	–0.9	50	ash				
0.70	–0.9	45	ash				
0.73	–0.9	30	ash				
0.76	–0.9	30	ash				
0.80	–0.9	40	ash				
0.83	–0.9	40	ash				
0.87	–0.9	55	ash				
0.90	–0.9	60	ash				
0.93	–0.9	30	ash				
0.96	–0.9	20	ash				
1.00	–0.9	25	ash				

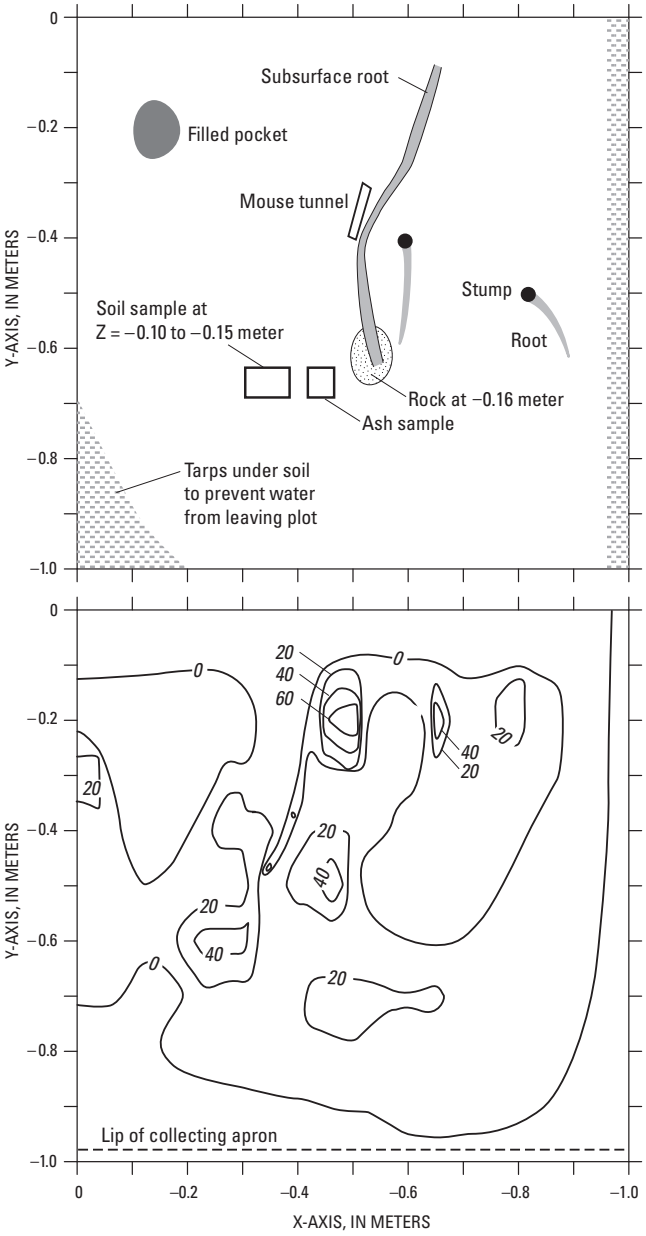

Figure 15. Drawing of subsurface and surface features for Plot N13 and contours of ash thickness.

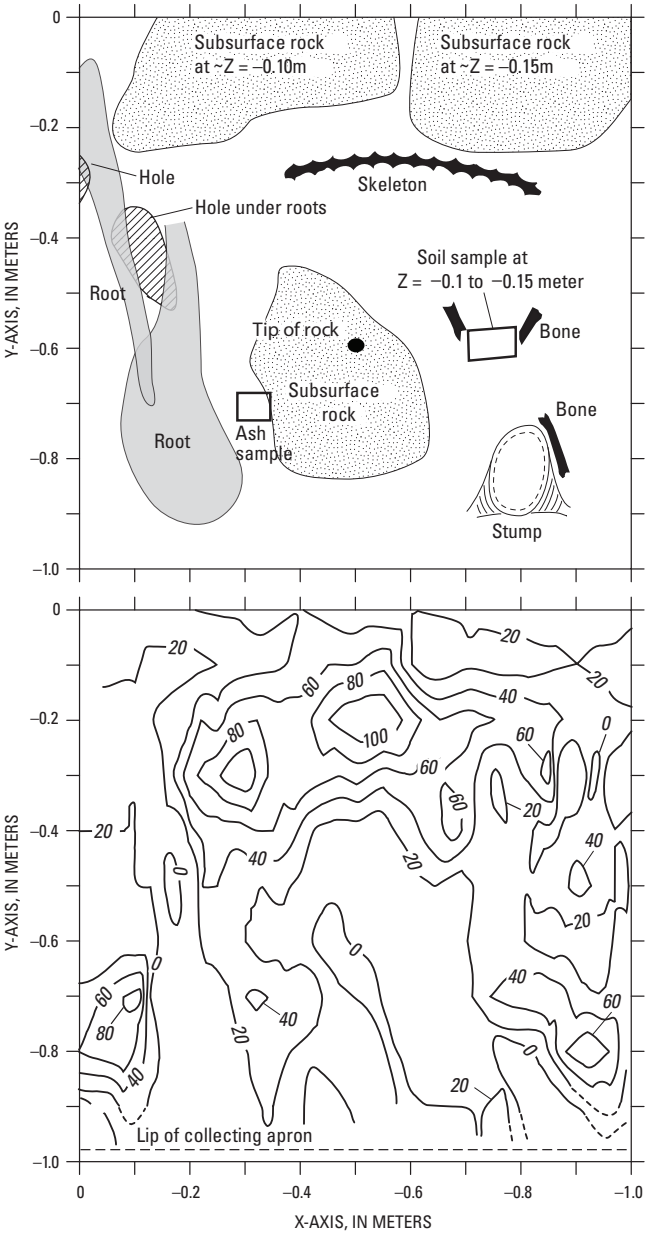

Figure 16. Drawing of subsurface and surface features for Plot N15 and contours of ash thickness.

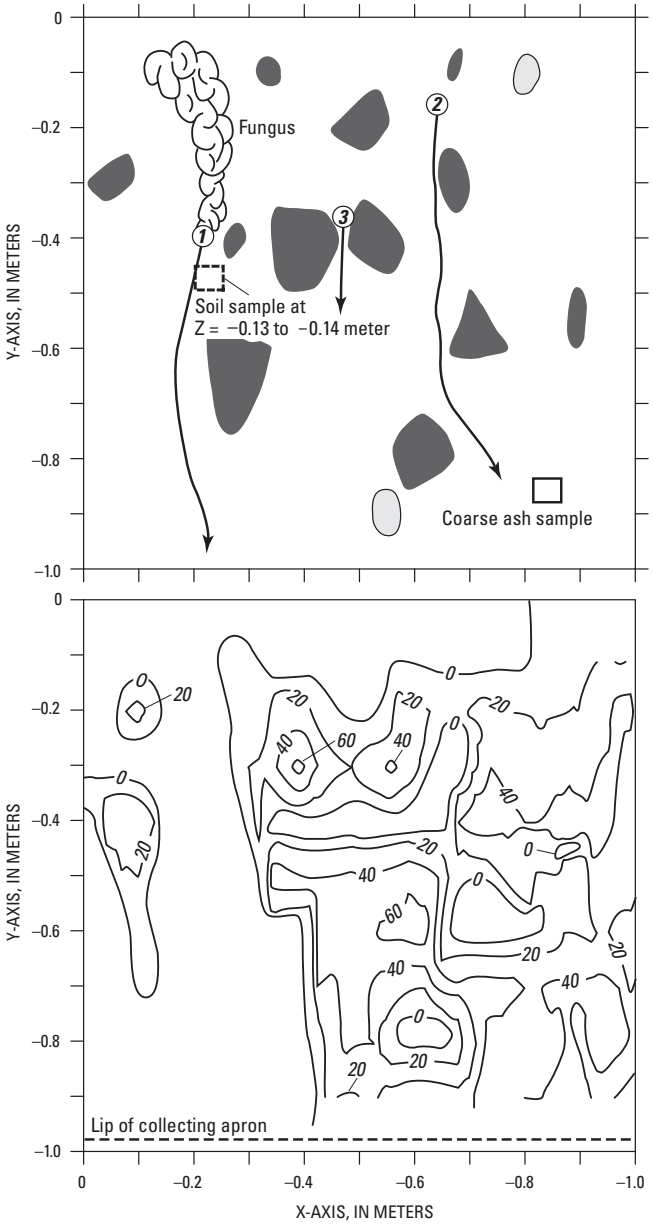

Figure 17. Drawing of subsurface and surface features for Plot S13 and contours of ash thickness.

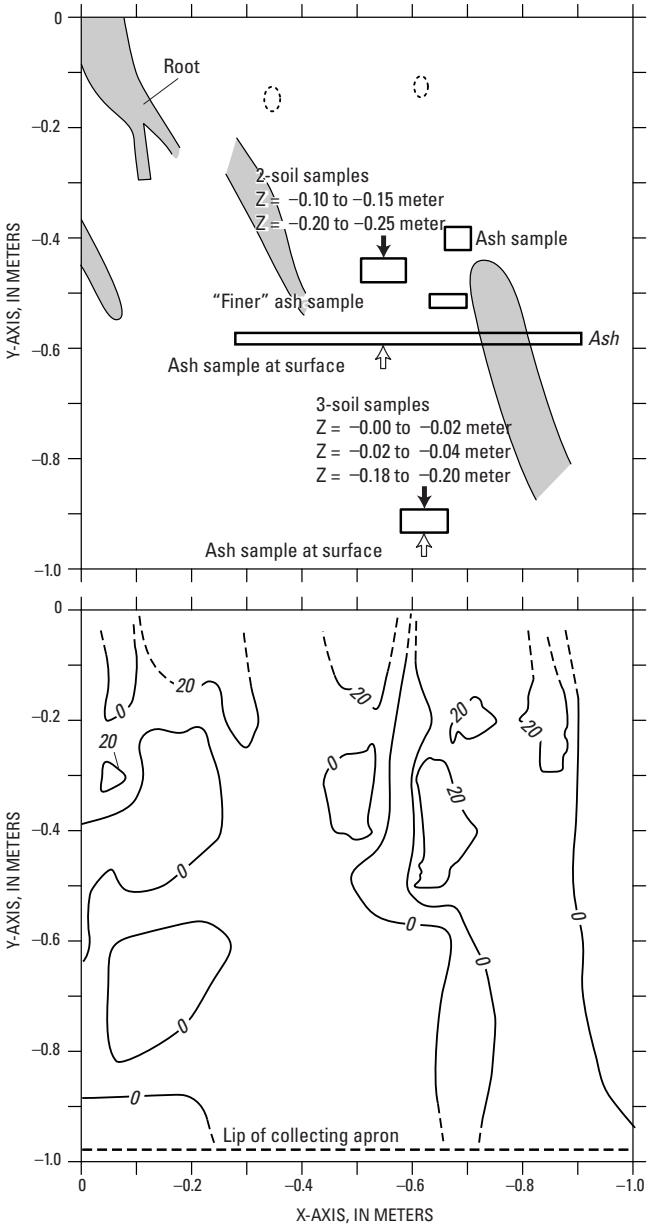

Figure 18. Drawing of subsurface and surface features for Plot S15 and contours of ash thickness.

The loss on ignition (LOI) is one method of quantifying the percentage of organic matter in each size class of ash. This percentage of organic matter decreased with decrease in particle size of the ash from about 20 percent (on average) for 4–8-mm particles to about 8 percent (on average) for the less than 0.063 mm particles (table 9). For 55 percent of the samples, the LOI was less than 10 percent by mass. However, in two samples, the LOI exceeded 50 percent. One of these samples, from plot S13, reflects the observed presence of partially combusted needles on the soil surface.

In contrast to the relation between size and LOI, both the bulk density and particle density of the ash increased with decrease in particle size (table 9). As a bulk material, ash will float on the water but individual particles have a density greater than water. This particle density probably suggest that ash may be a mixture of the organic matter burned during the fire and the relatively heavy minerals re-suspended and transported by the wind during the fire and by natural eolian transport after the fire.

Particle sizes of north- and south-facing soils were different. The north-facing plots had finer material at all sampled depths (table 9; figure 19; mean D_{50}=0.75 mm). The south-facing plots have sizes that are dominated by the 1–2 mm size fraction (table 9; figure 19; mean D_{50}=1.40 mm). Despite these aspect-related differences, particle-size differences between the surface samples (0–0.05 m) and the underlying soil did not exist. The exception to this is plot N15, which has a finer surface layer than the underlying soil. The lack of discrepancy between these layers likely is related to the fact that the surface layer (0–0.05 m) incorporates a mixture of ash into the underlying sandy soil.

Soil Moisture

The time between rainfall experiments on the same plots and the ambient seasonal moisture cycle influenced the soil moisture before each experiment. In general, the soil moisture on the north-facing plots before and after experiments was higher than those on the south-facing plots (tables 10 and 11). This may be because the north-facing plots retain water better than south-facing plots or that north-facing experiments were conducted a month later (in the fall) than the south-facing

Table 9. Ash and soil characteristics within the plots.

[m, meter; mm, millimeter; kg, kilogram; D_{50}, median particle diameter; <, less than; °C, degrees Celsius]

Material	Plot	Coordinates of sample			Percentage of total sample in each size class								D_{50} (mm)
		x (m)	y(m)	z(m)	8–4 mm	4–2 mm	2–1 mm	1–0.500 mm	0.500–0.250 mm	0.250–0.125 mm	0.125–0.063 mm	<0.063 mm	
Ash	N13	0.40	0.65	0.00	2.4	7.7	16.6	19.3	19.0	20.8	9.6	4.7	0.40
		0.50	0.75	0.03									
Ash	N15	0.30	0.70	0.00	4.8	4.3	10.1	14.4	20.7	31.0	11.4	3.3	0.30
		0.40	0.80	0.03									
		North-facing mean			3.6	6.0	13.4	16.8	19.9	25.9	10.5	4.0	0.35
Ash	S13	0.85	0.85	0.00	1.7	6.8	16.1	23.6	22.7	25.6	2.2	1.3	0.48
		0.95	0.90	0.03									
Ash	S15	0.57	0.88	0.00	18.0	21.4	21.0	15.2	10.2	8.3	3.7	2.2	1.50
		0.64	0.90	0.03									
Ash	S15	0.30	0.58	0.00	9.1	18.2	21.7	17.7	16.0	8.7	5.1	3.6	0.97
		0.86	0.60	0.01									
Ash	S15	0.50	0.48	0.00	5.3	14.0	21.2	18.8	15.6	11.9	9.2	4.0	0.75
		0.55	0.50	0.05									
Ash	S15	0.63	0.48	0.00	6.2	17.7	20.8	18.4	18.3	13.7	2.7	2.2	0.86
		0.73	0.50	0.02									
Ash	S15	0.64	0.38	0.00	7.9	18.5	21.9	21.6	16.0	10.0	2.3	2.0	0.96
		0.70	0.40	0.03									
		South-facing mean			8.0	16.1	20.4	19.2	16.4	13.0	4.2	2.5	0.92
					Ash bulk density (kg/m^3)			200	320	500	710	850	
					Ash particle density (kg/m^3)			did not analyze		1,700	1,800	2,400	

experiments when soil moisture was higher. Additionally, for experiments 10 and 12, rainfall simulations were run immediately after experiments 9 and 11. Thus, the preexperiment soil-moisture content was the same as the postexperiment soil moisture measured after experiments 9 and 11. All postexperiment measurements of soil moisture for each experiment were either greater than or the same as the preexperiment measurements of soil moisture except for the surface measures for experiment 11. This difference is likely because the samples were taken in two different locations before and after the storm.

Plot Runoff

The discharge hydrograph can be divided into three separate phases. The phases are (1) discharge derived strictly from the plot collecting apron, (2) the rising limb of the hydrograph, and (3) a steady flow phase where fluctuations in discharge are small. Observations indicated that, generally, some discharge was derived from direct rainfall on the collecting apron (fig. 4) while no water was flowing off the soil surface inside the plot.

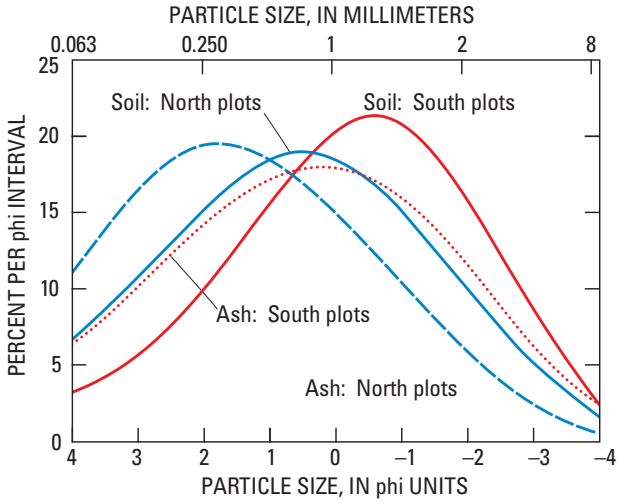

Figure 19. Particle-size distribution for ash and soil from the north- and south-facing plots.

Table 9. Ash and soil characteristics within the plots.—Continued

[m, meter; mm, millimeter; kg, kilogram; D_{50}, median particle diameter; <, less than; °C, degrees Celsius]

Material	Plot	Coordinates of sample			Percentage of total sample lost on ignition at 550°C							
		x (m)	y(m)	z(m)	8–4 mm	4–2 mm	2–1 mm	1–0.500 mm	0.500–0.250 mm	0.250–0.125 mm	0.125–0.063 mm	<0.063 mm
Ash	N13	0.40	0.65	0.00	1.7	3.9	3.3	3.6	5.7	7.7	6.4	5.9
		0.50	0.75	0.03								
Ash	N15	0.30	0.70	0.00	48.8	32.5	15.4	10.9	8.1	8.1	6.1	4.9
		0.40	0.80	0.03								
		North-facing mean			25.3	18.2	9.4	7.3	6.9	7.9	6.3	5.4
Ash	S13	0.85	0.85	0.00	60.7	51.18	43.9	30.1	18.4	14.1	10.5	6.4
		0.95	0.90	0.03								
Ash	S15	0.57	0.88	0.00	14.9	5.9	9.8	10.2	10.9	10.5	8.9	8.3
		0.64	0.90	0.03								
Ash	S15	0.30	0.58	0.00	did not analyze							
		0.86	0.60	0.01								
Ash	S15	0.50	0.48	0.00	did not analyze							
		0.55	0.50	0.05								
Ash	S15	0.63	0.48	0.00	4.7	3.7	5.1	8.6	11.7	10.5	9.1	7.8
		0.73	0.50	0.02								
Ash	S15	0.64	0.38	0.00	did not analyze							
		0.70	0.40	0.03								
		South-facing mean			26.8	20.3	19.6	16.3	13.7	11.7	9.5	7.5
		Ash bulk density (kg/m³)			did not analyze							
		Ash particle density (kg/m³)			did not analyze							

Table 10. Pre- and postexperiment measurements of soil moisture and particle size at various depths for each rainfall simulation experiment on north-facing slope.

[Samples were collected adjacent to but outside each plot; kPa, kilopascals; psi, pounds per square inch; m, meters; kg, kilograms; D_{50}, median particle diameter; mm, millimeters; --, no data]

Experiment number	Date of collection (m/d/y)	Pre- or post-experiment	Plot	Nozzle	Pressure		Depth (m)	Soil moisture (kg/kg)	D_{50} (mm)
					(kPa)	(psi)			
9	10/8/04	Pre	N13	2.8W	34	5	0.00–0.05	0.27	0.62
							0.10–0.15	0.16	0.58
							0.20–0.25	0.18	0.99
9	10/8/04	Post	N13	2.8W	34	5	0.00–0.05	0.27	1.22
							0.10–0.15	0.19	1.19
							0.20–0.25	0.19	1.05
10	10/8/04	Pre	N13	10W	34	5	0.00–0.05	0.27	1.22
							0.10–0.15	0.19	1.19
							0.20–0.25	0.19	1.05
10	10/8/04	Post	N13	10W	34	5	0.00–0.05	0.52	0.58
							0.10–0.15	0.23	0.43
							0.20–0.25	0.25	0.52
14	10/9/04	Pre	N13	20W	69	10	0.00–0.05	0.25	0.70
							0.10–0.15	0.22	0.59
							0.20–0.25	0.26	0.73
14	10/9/04	Post	N13	20W	69	10	0.00–0.05	0.35	0.64
							0.10–0.15	0.21	0.81
							0.20–0.25	0.25	0.51
11	10/8/04	Pre	N15	2.8W	34	5	0.00–0.05	0.66	0.26
							0.10–0.15	0.19	0.69
							0.20–0.25	0.19	0.47
11	10/8/04	Post	N15	2.8W	34	5	0.00–0.05	0.42	0.45
							0.10–0.15	0.22	0.78
							0.20–0.25	0.20	0.51
12	10/8/04	Pre	N15	10W	34	5	0.00–0.05	0.42	0.45
							0.10–0.15	0.22	0.78
							0.20–0.25	0.20	0.51
12	10/8/04	Post	N15	10W	34	5	0.00–0.05	0.45	0.37
							0.10–0.15	0.25	0.53
							0.20–0.25	0.20	0.93
13	10/9/04	Pre	N15	20W	69	10	0.00–0.05	0.39	0.43
							0.10–0.15	0.22	0.56
							0.20–0.25	0.19	0.48
13	10/9/04	Post	N15	20W	69	10	0.00–0.05	0.42	0.36
							0.10–0.15	0.28	0.41
							0.20–0.25	--	--

Table 11. Pre- and postexperiment measurements of soil moisture and particle size at various depths for each rainfall simulation experiment on the south-facing slope.

[Samples were collected adjacent to but outside each plot; kPa, kilopascals; psi, pounds per square inch; m, meters; kg, kilograms; mm, milligrams; D_{50}, median particle diameter]

Experiment number	Date of collection (m/d/y)	Pre- or post-experiment	Plot	Nozzle	Pressure		Depth (m)	Soil moisture (kg/kg)	D50 (mm)
					(kPa)	(psi)			
1	9/1/04	Pre	S13	20W	69	10	0.00–0.05	0.09	1.19
							0.10–0.15	0.12	0.89
							0.20–0.25	0.09	1.15
1	9/1/04	Post	S13	20W	69	10	0.00–0.05	0.19	1.08
							0.10–0.15	0.14	1.01
							0.20–0.25	0.15	0.92
4	9/2/04	Pre	S13	20W	69	10	0.00–0.05	0.13	1.19
							0.10–0.15	0.14	0.95
							0.20–0.25	0.13	0.85
4	9/2/04	Post	S13	20W	69	10	0.00–0.05	0.23	0.86
							0.10–0.15	0.19	0.92
							0.20–0.25	0.18	0.95
5	9/8/04	Pre	S13	10W	34	5	0.00–0.05	0.08	0.94
							0.10–0.15	0.13	1.25
							0.20–0.25	0.11	1.74
5	9/8/04	Post	S13	10W	34	5	0.00–0.05	0.21	0.89
							0.10–0.15	0.21	1.23
							0.20–0.25	0.19	1.18
8	9/9/04	Pre	S13	2.8W	34	5	0.00–0.05	0.14	1.06
							0.10–0.15	0.16	1.39
8	9/9/04	Post	S13	2.8W	34	5	0.00–0.05	0.17	1.06
							0.10–0.15	0.15	1.49
2	9/1/04	Pre	S15	10W	138	20	0.00–0.06	0.06	1.48
							0.13–0.17	0.13	0.97
							0.20–0.25	0.12	0.98
2	9/1/04	Post	S15	10W	138	20	0.00–0.05	0.15	3.35
							0.13–0.17	0.21	0.90
							0.20–0.25	0.19	1.06
3	9/2/04	Pre	S15	10W	138	20	0.00–0.05	0.16	0.77
							0.10–0.15	0.16	0.86
							0.20–0.25	0.16	1.02
3	9/2/04	Post	S15	10W	138	20	0.00–0.05	0.21	1.58
							0.10–0.15	0.22	1.03
							0.20–0.25	0.26	0.69
6	9/8/04	Pre	S15	10W	34	5	0.00–0.05	0.06	1.39
							0.10–0.15	0.15	1.34
							0.20–0.25	0.14	1.56
6	9/8/04	Post	S15	10W	34	5	0.00–0.05	0.15	1.23
							0.10–0.15	0.18	1.52
							0.20–0.25	0.19	1.56
7	9/9/04	Pre	S15	2.8W	34	5	0.00–0.05	0.09	1.66
							0.10–0.15	0.16	1.54
							0.20–0.25	0.15	1.32
7	9/9/04	No postexperiment samples were collected because we ran sheet-calibration experiments.							

Table 12. Raw runoff and corrected runoff data at approximately 1-minute intervals.

[min, minutes; L/min, liters per minute; L, liters; data after 30 minutes represent runoff without rainfall]

Experiment 1			Experiment 2			Experiment 3			Experiment 4		
C_{apron} = 0.0278 L/min			C_{apron} = 0.0284 L/min			C_{apron} = 0.0284 L/min			C_{apron} = 0.0291 L/min		
Elapsed time (min)	Runoff (L)	Corrected runoff (L)	Elapsed time (min)	Runoff (L)	Corrected runoff (L)	Elapsed time (min)	Runoff (L)	Corrected runoff (L)	Elapsed time (min)	Runoff (L)	Corrected runoff (L)
0.0	0.000	0.000	0.0	0.000	0.000	0.0	0.000	0.000	0.0	0.000	0.000
1.2	0.047	0.015	1.0	0.033	0.005	1.0	0.037	0.009	1.0	0.007	–0.022
2.5	0.043	0.006	2.0	0.038	0.009	2.0	0.069	0.041	2.0	0.030	0.001
3.5	0.047	0.019	3.1	0.047	0.017	3.0	0.250	0.222	3.0	0.047	0.018
4.5	0.101	0.073	4.0	0.052	0.025	4.0	0.395	0.367	4.0	0.090	0.061
6.5	0.220	0.164	5.1	0.125	0.094	5.0	0.405	0.377	5.0	0.120	0.091
7.5	0.180	0.152	6.0	0.160	0.134	6.0	0.400	0.372	6.0	0.135	0.106
8.7	0.200	0.167	7.0	0.220	0.192	7.0	0.410	0.382	7.0	0.175	0.146
9.6	0.140	0.115	8.0	0.275	0.247	8.0	0.530	0.502	8.0	0.220	0.191
10.5	0.260	0.235	9.0	0.350	0.322	9.0	0.490	0.462	9.0	0.260	0.231
11.5	0.250	0.222	10.0	0.390	0.362	10.0	0.460	0.432	10.0	0.250	0.221
12.6	0.250	0.220	11.0	0.420	0.392	11.0	0.450	0.422	11.1	0.280	0.248
13.5	0.270	0.244	12.0	0.420	0.392	12.0	0.450	0.422	12.0	0.215	0.189
14.5	0.290	0.262	13.0	0.420	0.392	13.0	0.465	0.437	13.0	0.230	0.201
15.5	0.290	0.262	14.0	0.465	0.437	14.0	0.475	0.447	14.0	0.240	0.211
16.5	0.310	0.282	15.0	0.410	0.382	15.0	0.440	0.412	15.0	0.230	0.201
17.5	0.300	0.272	16.0	0.430	0.402	16.0	0.370	0.342	16.0	0.230	0.201
18.5	0.300	0.272	17.0	0.405	0.377	17.0	0.435	0.407	17.0	0.230	0.201
19.6	0.320	0.290	18.0	0.390	0.362	18.0	0.480	0.452	18.1	0.250	0.218
20.5	0.300	0.274	19.0	0.440	0.412	19.0	0.490	0.462	19.0	0.215	0.188
21.5	0.295	0.267	20.0	0.475	0.447	20.0	0.460	0.432	20.1	0.270	0.237
22.5	0.310	0.282	21.0	0.455	0.427	21.0	0.450	0.422	21.0	0.180	0.155
23.5	0.290	0.262	22.0	0.465	0.437	22.0	0.470	0.442	22.0	0.210	0.181
24.5	0.300	0.272	23.0	0.475	0.447	23.0	0.520	0.492	23.0	0.220	0.191
25.5	0.270	0.242	24.0	0.480	0.452	24.0	0.400	0.372	24.0	0.225	0.196
26.5	0.295	0.267	25.0	0.500	0.472	25.0	0.470	0.442	25.0	0.215	0.186
27.5	0.315	0.287	26.0	0.480	0.452	26.0	0.465	0.437	26.0	0.220	0.191
28.5	0.300	0.272	27.0	0.475	0.447	27.0	0.460	0.432	27.0	0.220	0.191
29.5	0.300	0.272	28.0	0.470	0.442	28.0	0.450	0.422	28.0	0.215	0.186
30.5	0.220	0.192	29.0	0.470	0.442	29.0	0.440	0.412	29.0	0.220	0.191
31.5	0.046	0.018	30.0	0.490	0.462	30.0	0.430	0.402	30.0	0.220	0.191
32.5	0.017	–0.011	31.0	0.180	0.152	31.0	0.150	0.122	31.0	0.087	0.058
33.7	0.009	–0.025	32.0	0.049	0.021	32.0	0.012	–0.016	32.0	0.003	–0.026
			33.0	0.011	–0.017						

Table 12. Raw runoff and corrected runoff data at approximately 1-minute intervals.—Continued

[min, minutes; L/min, liters per minute; L, liters; data after 30 minutes represent runoff without rainfall]

Experiment 5			Experiment 6			Experiment 7		
C_{apron} = 0.0207 L/min			C_{apron} = 0.0194 L/min			C_{apron} = 0.0084 L/min		
Elapsed time (min)	Runoff (L)	Corrected runoff (L)	Elapsed time (min)	Runoff (L)	Corrected runoff (L)	Elapsed time (min)	Runoff (L)	Corrected runoff (L)
0.0	0.000	0.000	0.0	0.000	0.000	0.0	0.000	0.000
1.0	0.020	–0.001	1.0	0.034	0.015	1.0	0.005	–0.003
2.0	0.024	0.003	2.0	0.027	0.008	2.0	0.007	–0.001
3.0	0.027	0.006	3.0	0.027	0.007	3.1	0.010	0.000
4.0	0.047	0.026	4.0	0.021	0.002	4.0	0.006	–0.001
5.0	0.058	0.037	5.0	0.026	0.007	5.0	0.009	0.001
6.0	0.060	0.039	6.0	0.031	0.012	6.0	0.010	0.002
7.0	0.088	0.067	7.0	0.055	0.036	7.0	0.022	0.014
8.0	0.088	0.067	8.0	0.071	0.052	8.0	0.029	0.021
9.0	0.088	0.067	9.0	0.080	0.061	9.0	0.027	0.019
10.0	0.090	0.069	10.0	0.083	0.064	10.0	0.036	0.028
11.0	0.084	0.063	11.0	0.098	0.079	11.0	0.033	0.024
12.1	0.110	0.087	12.0	0.115	0.096	12.0	0.033	0.025
13.0	0.091	0.073	13.0	0.130	0.111	13.0	0.037	0.029
14.0	0.103	0.082	14.0	0.142	0.123	14.0	0.038	0.030
15.2	0.116	0.092	15.0	0.126	0.107	15.0	0.033	0.025
16.0	0.090	0.072	16.0	0.133	0.114	16.0	0.028	0.020
16.9	0.094	0.074	17.0	0.166	0.147	17.0	0.033	0.025
18.0	0.186	0.164	18.0	0.173	0.154	18.0	0.032	0.024
19.0	0.114	0.093	19.0	0.150	0.131	19.0	0.025	0.016
20.3	0.148	0.122	20.0	0.160	0.141	20.1	0.029	0.019
21.0	0.096	0.080	21.0	0.145	0.126	21.2	0.029	0.020
22.0	0.129	0.108	22.0	0.144	0.125	22.0	0.024	0.017
23.0	0.147	0.126	23.1	0.152	0.130	23.0	0.032	0.024
24.0	0.221	0.200	24.0	0.109	0.092	24.0	0.026	0.018
25.1	0.200	0.177	25.0	0.130	0.111	25.0	0.027	0.019
26.0	0.140	0.121	26.0	0.147	0.128	26.0	0.027	0.019
27.0	0.140	0.119	27.0	0.104	0.085	27.0	0.022	0.014
28.0	0.155	0.134	28.0	0.106	0.087	28.0	0.025	0.017
29.0	0.140	0.119	29.0	0.108	0.089	29.0	0.032	0.024
30.0	0.180	0.159	30.0	0.132	0.113	30.0	0.028	0.020
31.0	0.047	0.026	31.0	0.053	0.034	31.0	0.016	0.008
32.0	0.089	0.068	32.0	0.012	–0.007	32.0	0.005	–0.003
33.0	0.050	0.029	33.0	0.009	–0.010	33.0	0.008	–0.000

Table 12. Raw runoff and corrected runoff data at approximately 1-minute intervals.—Continued

[min, minutes; L/min, liters per minute; L, liters; data after 30 minutes represent runoff without rainfall]

Experiment 8			Experiment 9			Experiment 10			Experiment 11		
C_{apron} = 0.0103 L/min			C_{apron} = 0.0116 L/min			C_{apron} = 0.0200 L/min			C_{apron} = 0.0123 L/min		
Elapsed time (min)	Runoff (L)	Corrected runoff (L)	Elapsed time (min)	Runoff (L)	Corrected runoff (L)	Elapsed time (min)	Runoff (L)	Corrected runoff (L)	Elapsed time (min)	Runoff (L)	Corrected runoff (L)
0.0	0.000	0.000	0.0	0.000	0.000	0.0	0.000	0.000	0.0	0.000	0.000
1.0	0.003	–0.007	1.0	0.000	–0.012	1.0	0.140	0.120	1.0	0.002	–0.010
2.0	0.003	–0.007	2.0	0.008	–0.004	2.0	0.120	0.100	2.0	0.019	0.007
3.0	0.014	0.004	3.0	0.007	–0.005	3.0	0.200	0.180	3.0	0.019	0.007
4.0	0.011	0.001	4.0	0.035	0.023	4.0	0.240	0.220	4.0	0.032	0.020
5.0	0.010	–0.000	5.0	0.056	0.044	5.0	0.225	0.205	5.0	0.022	0.010
6.0	0.012	0.002	6.0	0.076	0.064	6.0	0.250	0.230	6.0	0.033	0.021
7.0	0.012	0.002	7.0	0.089	0.077	7.1	0.270	0.248	7.0	0.039	0.027
8.0	0.012	0.001	8.1	0.105	0.093	8.0	0.240	0.222	8.0	0.045	0.033
9.0	0.012	0.002	9.0	0.094	0.083	9.0	0.260	0.240	9.0	0.049	0.037
10.0	0.012	0.002	10.0	0.091	0.079	10.0	0.260	0.240	10.0	0.058	0.046
11.0	0.010	–0.000	11.0	0.095	0.083	11.0	0.270	0.250	11.0	0.069	0.057
12.0	0.011	0.001	12.0	0.100	0.088	12.0	0.265	0.245	12.0	0.075	0.063
13.0	0.011	0.001	13.0	0.094	0.082	13.0	0.270	0.250	13.0	0.076	0.064
14.0	0.013	0.003	14.0	0.103	0.091	14.1	0.300	0.277	14.0	0.077	0.065
15.0	0.011	0.001	15.0	0.102	0.090	15.3	0.300	0.276	15.0	0.079	0.067
16.0	0.010	–0.000	16.0	0.102	0.090	16.1	0.230	0.215	16.0	0.079	0.067
17.0	0.011	0.001	17.2	0.111	0.097	17.0	0.225	0.207	17.0	0.075	0.063
18.0	0.013	0.003	18.1	0.116	0.105	18.0	0.250	0.230	18.0	0.074	0.062
19.0	0.010	–0.000	19.1	0.096	0.084	19.0	0.245	0.225	19.0	0.071	0.059
20.1	0.014	0.003	20.1	0.089	0.079	20.0	0.255	0.235	20.0	0.079	0.067
21.0	0.009	–0.000	21.0	0.095	0.084	21.0	0.260	0.240	21.1	0.077	0.064
22.0	0.011	0.001	22.0	0.096	0.084	22.0	0.260	0.240	22.0	0.073	0.061
23.0	0.011	0.001	23.0	0.084	0.072	23.0	0.265	0.245	23.0	0.081	0.069
24.0	0.010	–0.000	24.0	0.081	0.069	24.0	0.265	0.245	24.0	0.075	0.063
25.0	0.011	0.001	25.0	0.082	0.070	25.0	0.250	0.230	25.0	0.078	0.066
26.0	0.012	0.002	26.0	0.086	0.074	26.0	0.235	0.215	26.0	0.075	0.063
27.0	0.012	0.002	27.0	0.087	0.075	27.0	0.265	0.245	27.0	0.078	0.066
28.0	0.013	0.003	28.0	0.085	0.073	28.0	0.265	0.245	28.0	0.075	0.063
29.0	0.013	0.002	29.0	0.086	0.074	29.0	0.270	0.250	29.0	0.080	0.068
30.0	0.015	0.005	30.0	0.088	0.076	30.0	0.260	0.240	30.0	0.080	0.068
31.0	0.007	–0.003	31.1	0.061	0.048	31.0	0.325	0.305	31.0	0.034	0.022
32.0	0.002	–0.008	32.0	0.063	0.053	32.0	0.200	0.180	32.0	0.009	–0.003
			33.0	0.033	0.021	33.0	0.025	0.005			

Table 12. Raw runoff and corrected runoff data at approximately 1-minute intervals.—Continued

[min, minutes; L/min, liters per minute; L, liters; data after 30 minutes represent runoff without rainfall]

Experiment 12			Experiment 13			Experiment 14		
C_{apron} = 0.0220 L/min			C_{apron} = 0.0259 L/min			C_{apron} = 0.0236 L/min		
Elapsed time (min)	Runoff (L)	Corrected runoff (L)	Elapsed time (min)	Runoff (L)	Corrected runoff (L)	Elapsed time (min)	Runoff (L)	Corrected runoff (L)
0.0	0.000	0.000	0.0	0.000	0.000	0.0	0.000	0.000
1.0	0.012	–0.010	1.0	0.023	–0.003	1.0	0.030	0.006
2.0	0.057	0.035	2.0	0.054	0.028	2.0	0.033	0.009
3.0	0.120	0.098	3.0	0.150	0.124	3.0	0.260	0.236
4.0	0.170	0.148	4.0	0.240	0.214	4.0	0.400	0.376
5.0	0.210	0.188	5.0	0.320	0.294	5.0	0.450	0.426
6.0	0.215	0.193	6.0	0.350	0.324	6.0	0.450	0.426
7.0	0.205	0.183	7.0	0.390	0.364	7.0	0.495	0.471
8.0	0.210	0.188	8.0	0.380	0.354	8.0	0.490	0.466
9.0	0.200	0.178	9.0	0.380	0.354	9.0	0.470	0.446
10.0	0.200	0.178	10.0	0.400	0.374	10.0	0.490	0.466
11.0	0.200	0.178	11.0	0.380	0.354	11.0	0.485	0.461
12.0	0.200	0.178	12.0	0.390	0.364	12.0	0.492	0.468
13.0	0.200	0.178	13.0	0.375	0.349	13.0	0.492	0.468
14.0	0.200	0.178	14.0	0.400	0.374	14.0	0.490	0.466
15.0	0.205	0.183	15.0	0.415	0.389	15.0	0.490	0.466
16.0	0.200	0.178	16.0	0.400	0.374	16.1	0.515	0.489
17.0	0.200	0.178	17.0	0.380	0.354	17.0	0.435	0.413
18.0	0.190	0.168	18.0	0.405	0.379	17.9	0.465	0.443
19.0	0.195	0.173	19.0	0.415	0.389			
20.0	0.200	0.178	20.0	0.420	0.394			
21.0	0.190	0.168	21.0	0.410	0.384			
22.0	0.200	0.178	22.0	0.400	0.374			
23.0	0.190	0.168	23.0	0.400	0.374			
24.0	0.190	0.168	24.0	0.395	0.369			
25.0	0.190	0.168	25.0	0.405	0.379			
26.0	0.195	0.173	26.1	0.430	0.402			
27.0	0.190	0.168	27.0	0.380	0.356			
28.0	0.190	0.168	28.0	0.430	0.404			
29.0	0.200	0.178	29.0	0.410	0.384			
30.0	0.195	0.173	30.0	0.405	0.379			
31.0	0.190	0.168	31.0	0.190	0.164			
32.0	0.100	0.078	32.0	0.020	–0.006			
33.0	0.016	-0.006	33.0	0.002	–0.024			

Therefore, any early contribution to the discharge was likely from the collecting apron. To develop a correction for the apron contribution, the predicted apron runoff was compared to the measured runoff during approximately the first minute (table 12), with the assumption that the first minute only represented collecting-apron discharge. The predicted discharge from the first minute was calculated as the apron area (0.07777 m^2) multiplied by the average rainfall intensity measured in the two small rain gages (table 4, bottom left, I_{BL}, and bottom right, I_{BR}, and adjusted using equation 8) at the downhill end of the plot near the collecting apron. One experiment (experiment 10, GG10W, 34 kPa) was not included in the comparison because experiment 9 was run immediately before the plot was wet, and the runoff during the first minute of experiment 10 was immediate. Runoff was much greater than all other experiments, and it was likely that prewetted plot runoff combined with the runoff from the collecting apron. The comparison of the predicted and measured apron discharge for the other 13 experiments (fig. 20) indicates that on average the measured discharge for the first minute was roughly one-half (0.52) the predicted apron discharge (fig. 20). The discharge from the collecting apron was probably less than that predicted discharge because part of the collecting apron was shielded by the lid. Some rain fell on the collecting apron despite the lid because the plot was on a 30–40 percent slope. Therefore, the following empirical equation was used to compute the apron correction, C_{apron}:

$$C_{apron} = 0.52 \text{ x } (0.96) \frac{(I_{BL} + I_{BR})}{2} A_{apron} \quad (8)$$

where the 0.96 comes from equation (7) and 0.52 comes from the regression equation shown on figure 20. This correction multiplied by the time interval was subtracted from the entire hydrograph to give a corrected hydrograph. However, because of the uncertainty in the correlation between the predicted discharge and the measured discharge (fig. 20), any value of the corrected hydrograph that was less than zero was set to zero.

The rising limb of the hydrograph was derived from the corrected hydrographs by using a smoothing procedure. First, the corrected hydrograph was smoothed by fitting a cubic spline to the data. The cubic spline program allowed the standard deviation between the observed points and the smoothed points to be specified (Robert Stallard, U.S. Geological Survey, 2005, written commun.). The standard deviation for the high-flow nozzles (GG20W and GG10W) was set at 0.020 L/min and the standard deviation for the low-flow nozzle (GG2.8W) was set at 0.005 L/min. This distinction was justified by our field procedure that used a smaller (0.100 L) graduated cylinder for the GG2.8W experiments. Second, the rising limb of hydrograph was defined as the segment of the smoothed, corrected hydrograph (table 13) from the start of the rain to the first 1-minute interval where the discharge, Q (L/min) was constant or decreases with time, t. This is the first local maximum of the runoff discharge or $dQ/dt \leq 0$. This time defined the end of the rising limb of the hydrograph and the beginning of the steady-state flow phase (table 13).

After the rise, the hydrograph entered a steady-state phase with small perturbations at 7–26 minutes. In some experiments, the discharge increased throughout the steady-state phase (experiment 2 and 13, fig. 21), decreased (experiments 4, 6, and 7, figs. 22, and 23), fluctuated (experiments 3 and 9, figs. 21 and 23), or remained fairly constant (experiment 1, 5, 9, 10, 11, 12, and 14, figs. 21, 22, and 23). Experiment 8 had no observed discharge and the corrected discharge (table 12) was always less than 0.005 L/min. In general, steady-state discharge perturbations could indicate an increasing or decreasing contributing area or experimental error. The temporal variability (coefficient of variation) of the steady-state discharge was

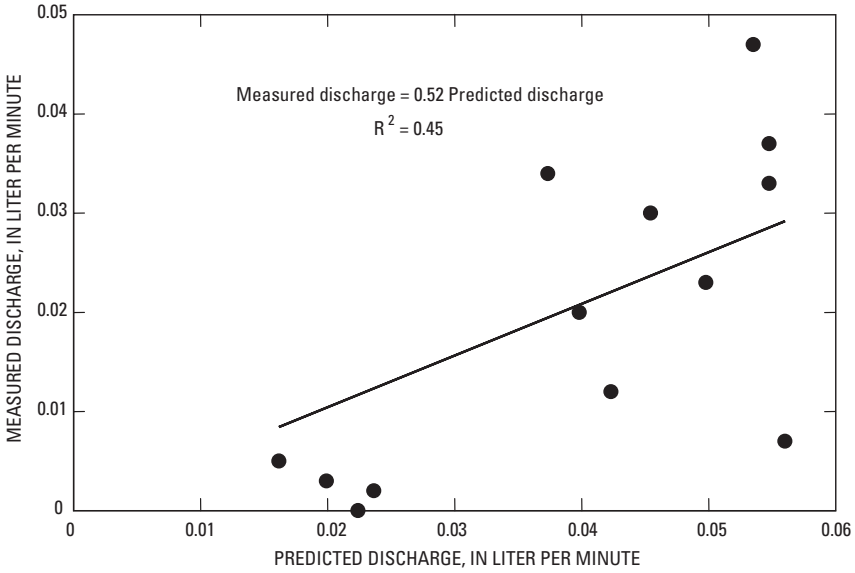

Figure 20. Correlation of predicted discharge from the collecting apron and the measured discharge during the first minute of experiment.

Table 13. Summary of rainfall, soil, and hydrologic data for rainfall simulation experiments.

[kPa, kilopascals; psi, pounds per square inch; mm/h, millimeters per hour; m^2, square meter; L/min, liters per minute; Exp., experiment; Exp. 8 had no observed runoff and an average ash thickness of 22 mm; --, no data; steady incident rainfall intensity is taken from table 4; plot area is the area projected on a horizontal surface; CV, coefficient of variation]

	High-intensity nozzles: GG20W and GG10W at 138 kPa (20 psi)						Medium-intensity nozzle: GG10W at 34 kPa (5 psi)				Low-intensity nozzle: GG2.8W at 34 kPa (5 psi)		
Experiment	1	2	3	4	13	14	5	6	10	12	7	9	11
Plot	S13	S15	S15	S13	N15	N13	S13	S15	N13	N15	S15	N13	N15
Steady incident rainfall intensity (mm/h)	46	48	46	49	47	51	37	34	34	35	20	23	25
Plot area (m^2)	0.90	0.92	0.92	0.90	0.91	0.93	0.90	0.92	0.93	0.91	0.92	0.93	0.91
Average ash thickness (mm)	22	9	9	22	27	10	22	9	10	27	9	10	27
Elapsed time (min)	**Smooth hydrograph discharge (L/min) during the preceding 1-minute interval**												
1	0.015	0.004	0.055	0.015	0.049	0.047	0.011	0.005	0.102	0.049	0.000	0.001	0.005
2	0.026	0.018	0.149	0.030	0.101	0.147	0.016	0.008	0.138	0.078	0.001	0.007	0.007
3	0.041	0.040	0.261	0.051	0.166	0.274	0.023	0.012	0.171	0.110	0.003	0.019	0.011
4	0.059	0.074	0.343	0.077	0.231	0.375	0.030	0.017	0.197	0.140	0.005	0.034	0.015
5	0.079	0.118	0.384	0.105	0.287	0.432	0.038	0.024	0.216	0.163	0.007	0.051	0.020
6	0.101	0.170	0.410	0.133	0.327	0.458	0.045	0.033	0.229	0.177	0.010	0.066	0.025
7	0.124	0.224	0.440	0.160	0.352	0.467	0.052	0.042	0.238	0.185	0.014	0.077	0.031
8	0.147	0.277	0.457	0.184	0.363	0.464	0.059	0.053	0.243	0.187	0.017	0.084	0.037
9	0.170	0.323	0.451	0.201	0.367	0.462	0.064	0.064	0.246	0.187	0.020	0.086	0.043
10	0.192	0.359	0.438	0.211	0.367	0.463	0.069	0.075	0.247	0.185	0.022	0.086	0.049
11	0.212	0.383	0.430	0.216	0.366	0.465	0.073	0.086	0.248	0.183	0.024	0.087	0.054
12	0.229	0.398	0.430	0.216	0.366	0.467	0.078	0.096	0.247	0.181	0.025	0.087	0.058
13	0.244	0.404	0.427	0.214	0.367	0.466	0.082	0.105	0.246	0.180	0.025	0.088	0.062
14	0.256	0.403	0.413	0.211	0.371	0.464	0.086	0.114	0.245	0.179	0.025	0.089	0.064
15	0.265	0.399	0.395	0.208	0.373	0.460	0.091	0.120	0.243	0.178	0.025	0.089	0.065
16	0.271	0.396	0.396	0.205	0.374	0.459	0.096	0.126	0.240	0.176	0.024	0.090	0.065
17	0.275	0.397	0.419	0.203	0.377	0.463	0.102	0.129	0.237	0.175	0.023	0.091	0.065
18	0.278	0.403	0.439	0.200	0.380	0.465	0.107	0.131	0.235	0.174	0.022	0.091	0.065
19	0.278	0.413	0.443	0.198	0.383	--	0.112	0.131	0.235	0.173	0.021	0.090	0.064
20	0.278	0.424	0.440	0.195	0.383	--	0.118	0.129	0.236	0.173	0.020	0.087	0.064
21	0.276	0.434	0.441	0.192	0.380	--	0.124	0.126	0.237	0.172	0.020	0.084	0.064
22	0.274	0.442	0.443	0.191	0.377	--	0.130	0.123	0.237	0.171	0.019	0.079	0.064
23	0.272	0.449	0.435	0.190	0.376	--	0.135	0.119	0.237	0.170	0.019	0.075	0.065
24	0.269	0.453	0.427	0.189	0.376	--	0.138	0.115	0.237	0.170	0.019	0.073	0.065
25	0.267	0.454	0.429	0.189	0.378	--	0.140	0.112	0.236	0.170	0.018	0.072	0.065
26	0.266	0.453	0.430	0.189	0.382	--	0.141	0.109	0.237	0.170	0.018	0.073	0.065
27	0.265	0.451	0.425	0.189	0.386	--	0.141	0.106	0.239	0.171	0.018	0.073	0.065
28	0.263	0.450	0.417	0.189	0.388	--	0.141	0.105	0.241	0.171	0.018	0.074	0.065
29	0.261	0.450	0.411	0.189	0.388	--	0.141	0.104	0.242	0.172	0.018	0.075	0.065
30	0.260	0.450	0.408	0.189	0.388	--	0.141	0.104	0.242	0.172	0.018	0.075	0.065
Time to steady-state discharge (min)	19	13	8	11	9	7	26	18	10	8	13	17	16
Average steady-state discharge (L/min)	0.268	0.431	0.427	0.197	0.377	0.464	0.141	0.115	0.240	0.175	0.020	0.079	0.065
CV of steady-state discharge	0.023	0.054	0.035	0.049	0.016	0.005	0.000	0.087	0.017	0.029	0.118	0.088	0.005
Steady Infiltration rate (mm/h)	28	20	18	36	23	21	28	26	19	24	19	18	21

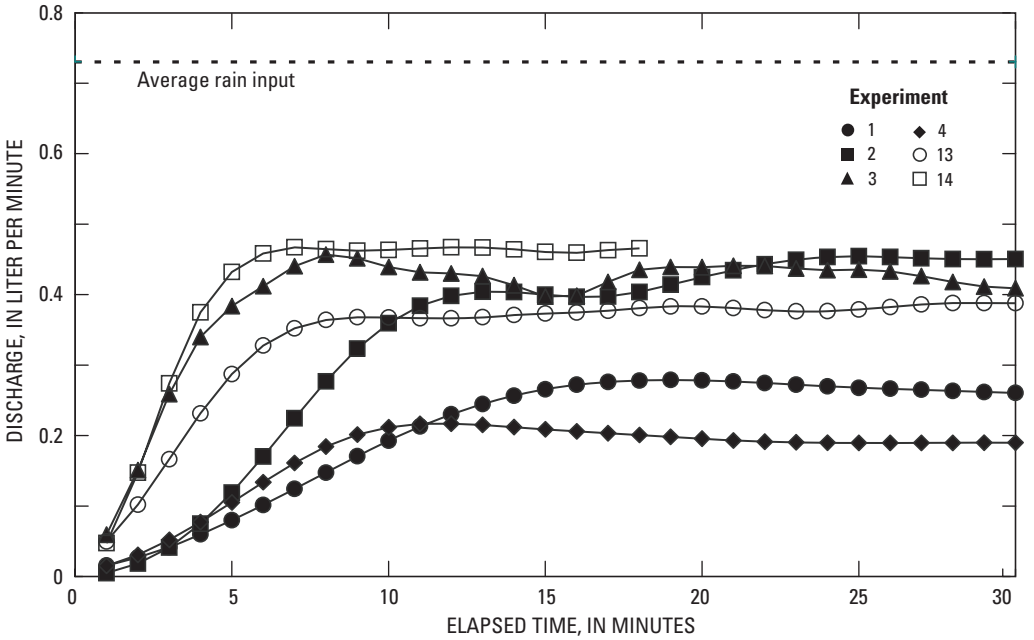

Figure 21. Smoothed discharge hydrographs for high-intensity nozzle GG20W at 69 kilopascals (10 pounds per square inch) and nozzle GG10W at 138 kilopascals (20 pounds per square inch).

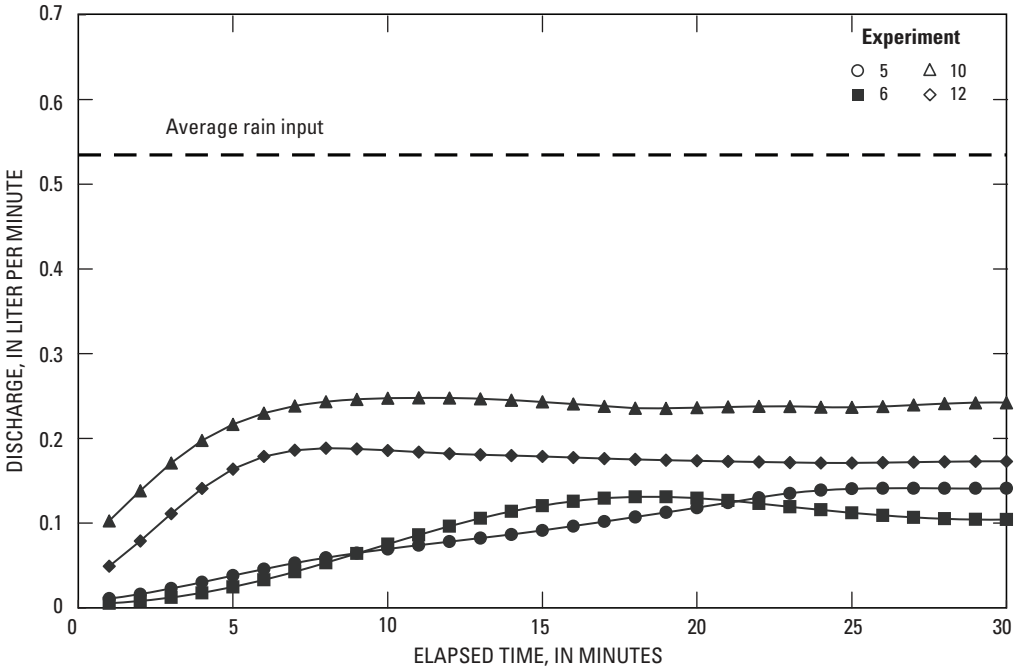

Figure 22. Smoothed discharge hydrographs for the medium-intensity nozzle GG10W at 34 kilopascals (5 pounds per square inch).

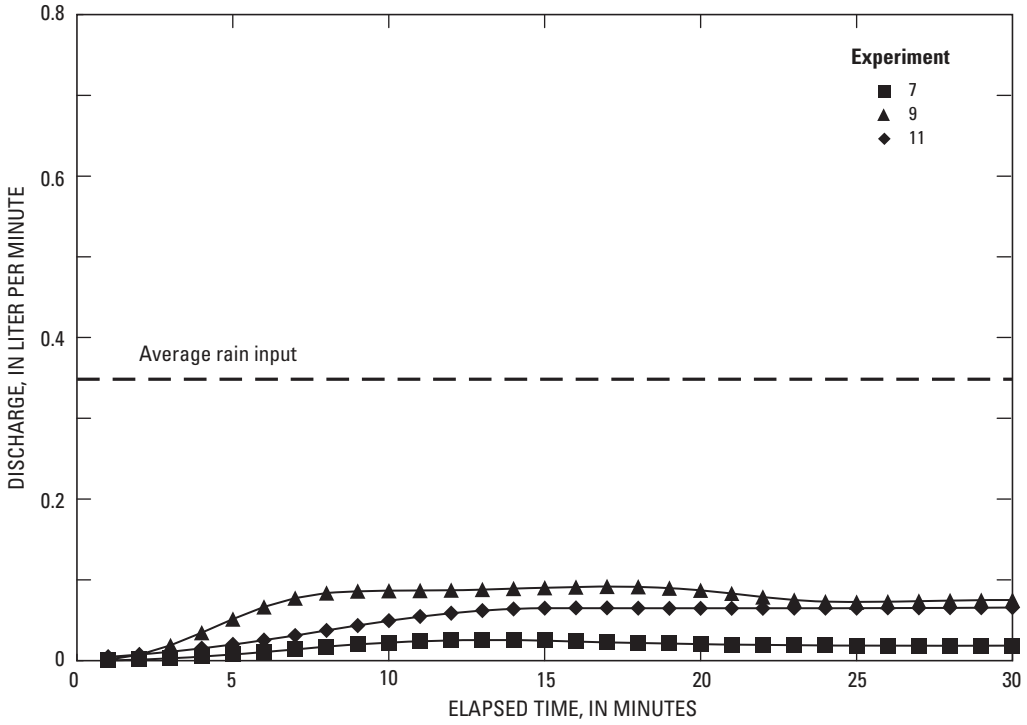

Figure 23. Smoothed discharge hydrographs for the low-intensity nozzle GG2.8W at 34 kilopascals (5 pounds per square inch).

largest (0.118) for the lowest rainfall intensity but ranged from 0.005 to 0.118. The perturbations associated with this temporal variability may represent second-order processes such as small debris dams forming and breaking, changing contributing area, connection of ponded areas along a flow path, connection of different flow paths, or the sudden infiltration of water into macropores.

We calculated the steady infiltration rate as the steady rainfall intensity minus the steady-state discharge. The field infiltration values reached a steady state much like those in the studies of Robichaud (2000) and Benavides-Solorio and MacDonald (2001). Their experiments use higher intensities (about 80 mm/h), so we cannot make a direct comparison with the runoff from our plots because the steady-state discharge is dependent on the rainfall intensity. However, one way of extrapolating to higher rainfall intensities is by using the model of Smith and Goodrich (2000). This model assumes an underlying continuous lognormal distribution of saturated hydraulic conductivity. Given that the steady infiltration rate theoretically approaches the effective saturated hydraulic conductivity of the soil, Smith and Goodrich (2000) have shown that the relation between rainfall intensity, I, and effective saturated hydraulic conductivity, K_{se}, can be described by:

$$\frac{K_{se}(I^*)}{\varepsilon_K} = \left[1 + \left(\frac{1}{I^*}\right)^p\right]^{\frac{-1}{p}} \quad (9)$$

where $I^* = I/\varepsilon_K$ is the rainfall intensity normalized by the mean value ε_K of the saturated hydraulic conductivity and p is defined as:

$$\rho = \frac{1.8}{CV_K^{0.85}} \quad (10)$$

where CV_K is the coefficient of variation in K_{se}. This model was fit by eye to the observed data and then extrapolated to higher values of rainfall intensity.

The steady infiltration rates measured for the soils in our study area differ from those measured in other burned areas in Colorado. Our study area had steady infiltration rates on the 1-m^2 scale at lower rainfall intensities similar to the steady infiltration rates (25–48 mm/h) measured by Benavides-Solorio and MacDonald (2001) in burned Ponderosa pine stands closest to our study area. For example, we calculated a steady infiltration rate of 20–36 mm/h for our GG20W nozzles. If these values are extrapolated to higher rainfall intensities using the Smith and Goodrich (2000) model, they are essentially the asymptotic values (22 and 26 mm/h), and it appears that on average, our steady infiltration rates are slightly lower than or the same as (fig. 24) than those recorded by Benavides-Solorio and MacDonald (2001). Benavides-Solorio and MacDonald indicate fairly minor differences between their steady runoff rates from burned and unburned areas. Martin and Moody (2001) using a different technique reported average steady infiltration rates (±95 percent confidence limits) of 26±15 mm/h (ponderosa pine), and 97±70

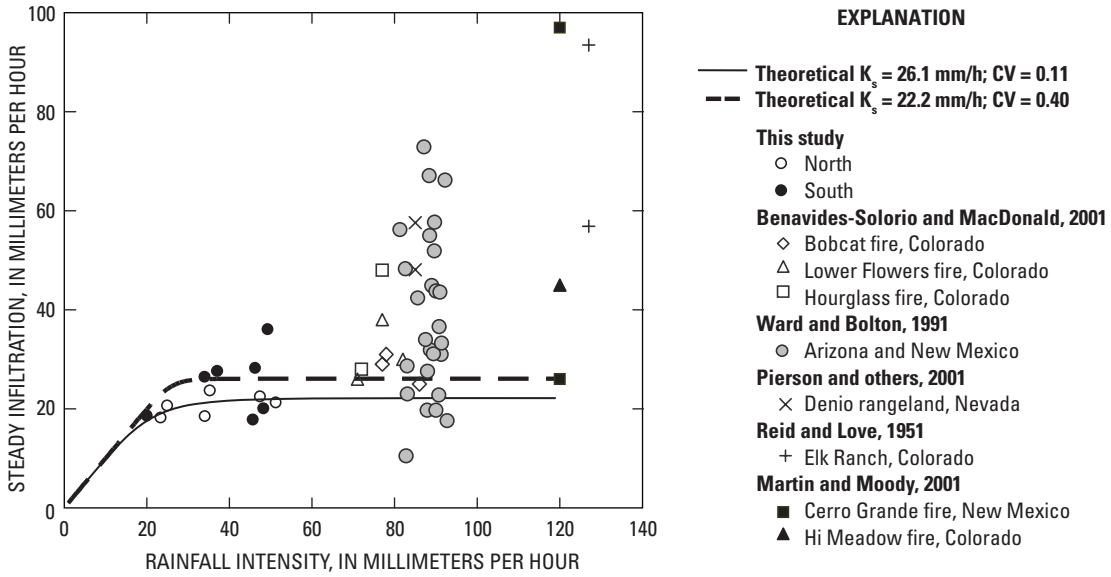

Figure 24. Steady-state infiltration rates as a function of steady rainfall intensity for burned and unburned plots in Colorado, New Mexico, and Nevada.

mm/h (mixed conifer) for two burned areas in New Mexico and rates of 45±16 mm/h for a burned area (ponderosa pine) in Colorado. Reid and Love (1951) reported steady infiltration rates of 51 to 90 mm/h for forested areas at a similar elevation as our study area. Overall, infiltration rates were largely in the range of 10 to 100 mm/h. Thus, despite the fact our study area was maybe not as severely burned as the other areas, the steady infiltration under high rainfall application was similar to data collected in burned areas elsewhere in Colorado and New Mexico and were in the range of 20–50 mm/h. However, the measurements in this study are among the lowest recorded values for infiltration rates during rainfall simulation in a several burned and unburned sites in Colorado and New Mexico (fig. 24). This may be because the ash layer at the soil surface was more intact (see "Research Site" section) than in the other studies.

One hypothesis we tested to explain plot runoff variability is that the infiltration rate is inversely proportional to the ash thickness. However, the infiltration rates measured in our rainfall simulation experiments were not correlated with the average ash thickness on the plots (fig. 25). The ash thickness was not uniform but spatially variable with some areas of bare soil. Plot S13 had a thick layer of ash (22 mm) but it also had three well-defined flow paths without ash (fig. 13 and table 8), which may have permitted greater infiltration. In contrast the ash thickness on plot S15 was less than S13, but plot S15 had less-defined flow paths (fig. 14), which contained some ash (fig. 14 and table 8) that may have absorbed water, thereby decreasing the infiltration rate. Plot N15 had the greatest average ash thickness (27 mm), less slope, finer soil (table 9), finer ash (table 9) that allowed the water to pond and run off, fewer well-defined flow paths, and a decrease in the infiltration rate relative to plot S15. Thus, the infiltration rate is probably a complex relation between rainfall intensity, slope, soil and ash particle size, ash thickness, and, important characteristics of the flow paths.

Differences between runoff for plots of different aspects were better detected at lower incident rainfall intensities. For example, when medium intensities (34–41 mm/h produced by nozzle GG10W and GG20W) were applied on the north plots (experiments 10 and 12), the plots produced a greater steady discharge (0.240 and 0.175 L/min, respectively) than the steady discharge (0.141 and 0.115 L/min) of the south plots (experiments 5 and 6 respectively). For experiments 10 and 12 on the north-facing soil, the hydrographs also rose more rapidly, but this may have been a function of the plots having been wet from an earlier experiment rather than a difference in capillary response of south-facing soils. Experiments using the GG2.8W nozzle indicate pronounced differences between the plots. No runoff was generated on plot S13 (experiment 8) and little was generated on S15 (experiment 7). Therefore, differences in north and south burned slopes are likely because of increased organic matter in north slope soils and distinct vegetation patterns on north and south slopes.

The rationale for using three rainfall intensities was to identify whether threshold rainfall for runoff could be measured for these burned plots. For three experiments (7, 8, and 11), the rainfall intensity was 19–20 mm/h. No observed runoff was generated for experiment 8 (20 mm/h) and only 0.020 and 0.065 L/min (table 13) were generated for experiments 7 (19 mm/h) and experiment 11 (20 mm/h). Thus, the work suggests that the observed rainfall threshold for these 1-m^2 plot experiments was about 20 mm/h (fig. 26), which is similar to thresholds (10–20 mm/h) identified in several field areas (Moody and Martin, 2001a; Kunze and Stednick, 2006; Moody and others, written commun., 2007).

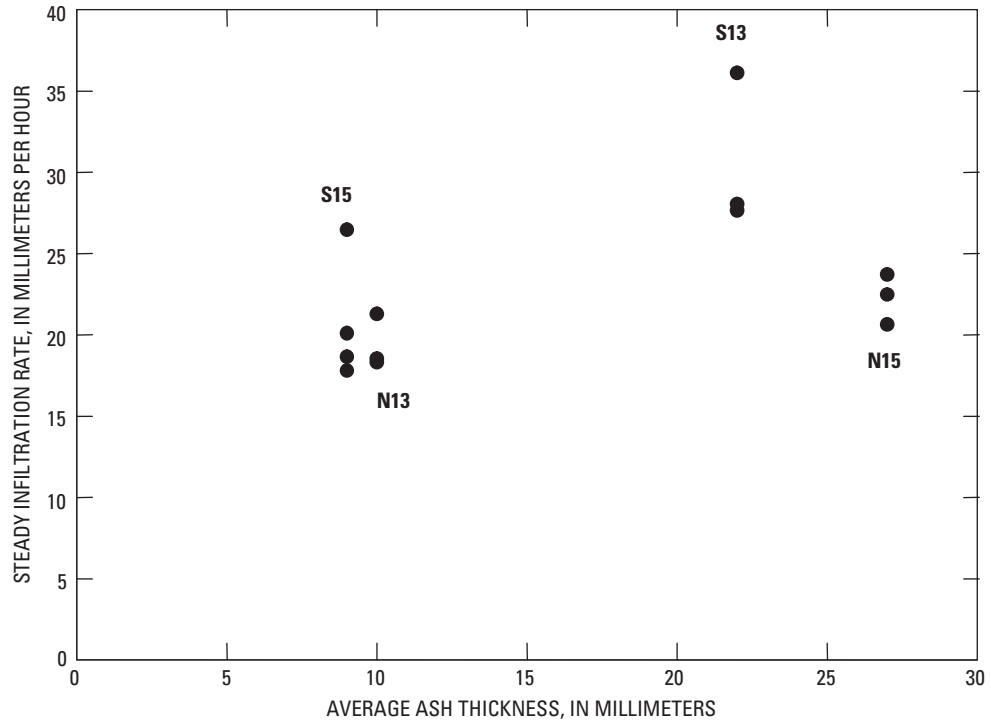

Figure 25. Correlation plot of steady-state infiltration rate relative to ash thickness.

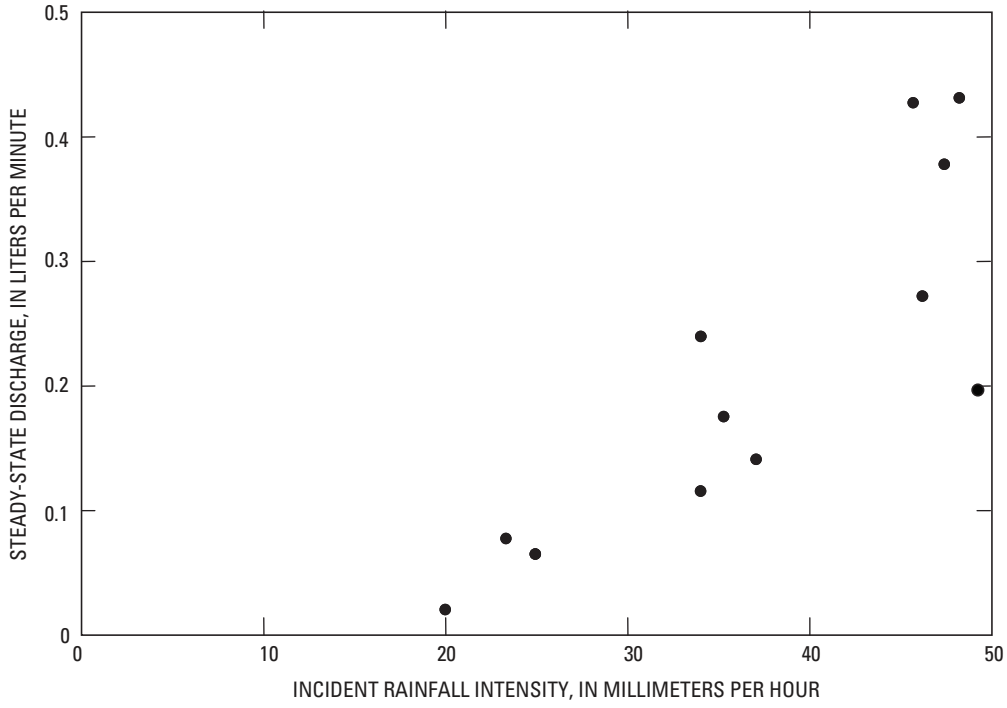

Figure 26. Plot of steady-state discharge as a function of incident rainfall intensity showing a threshold intensity at about 10–15 millimeters per hour.

Overland Flow Velocities and Flow Paths

Visual observations were recorded during the rising limb of the runoff hydrograph, and overland flow velocities were measured during the steady-state phase of the runoff hydrograph. The visual observations focused on identifying the condition of "ponding" where water was no longer infiltrating in an area (about 0.03 m in diameter), the depth of the water was accumulating, but the area had insufficient depth to produce runoff (tables 14 and 15). Flow velocities (table 16) ranged from 0.0028 m/s (experiment 7 on S15 with the lowest rainfall intensity of 19 mm/h) to 0.070 m/s (experiment 6 on S13 with a medium rainfall intensity of 34 mm/h). No velocity measurements were made for experiments 1–4 (on the south-facing plots) with the highest rainfall intensity (46–49 mm/h). The highest flow velocities for rainfall intensities of 47 and 51 mm/h (experiments 13 on N15 and experiment 14 on N15) were 0.042 and 0.064 m/s, respectively. In general, the flow paths were about 0.01 m wide with some as wide as 0.1 m, and a few flow depths were measured that ranged from 1 to 3 mm. We estimated the discharge from the flow paths as the product of 0.01 m (width) times 0.002 m (depth) times the average of all velocity measurements made in each flow path (table 16). The discharge from each contributing flow path was summed to give the total discharge for the flow-path network. For low-intensity rainfall, the total flow-path discharges (0.04 and 0.15 L/min for experiments 7 and 8, table 16) were essentially the same as the measured steady-state discharge

Table 14. Observations of runoff from north-facing plots during the rising limb of the hydrograph

[ponding, standing water covering an area greater than about 0.03 meter in diameter; the locations of ponding are a rough guide because flow paths were not straight; ~, approximate; --, no data; m, meter; min, minutes; times indicate when observations were made, not necessarily when the observed phenomena took place]

Elapsed time (min)	Location		Flow path	Observation
	x(m)	y(m)		
			Experiment 9; October 8, 2004; Plot N13	
1	--	--	--	surface got a little wet when tarp was removed; tarp leaked
2	0.20	–0.25	2	ponding
3	0.20	–0.25	2	runoff has begun all the way to the outlet on the collecting apron
	0.10	–0.35	1	connected to collecting apron
7	0.20	–0.05	2	connected to collecting apron
	0.10	–0.05	1	connected to collecting apron
9	0.48	–0.40	4	not fully connected
	0.90	–0.20	5	connected to collecting apron; has piece of tarp underneath
13	0.48	–0.40	4	still not connected; enters hole at x=0.52 m and y=0.40 m
	0.42	–0.60	3	pool of water
17–30	--	--	--	velocity measurements–see table 16
			Experiment 10; October 8, 2004; Plot N13	
1	0.10	–0.60	1 and 2	ponding where 1 and 2 meet
	0.42	–0.60	3	ponding
	0.48	–0.02	4	ponding
	0.90	–0.20	5	ponding
3	0.58	–0.72	6	new ponding downhill of root but not connected to collecting apron
4	0.90	–0.20	5	connected to collecting apron
5	0.10	–0.35	1	connected to collecting apron
	0.20	–0.25	2	connected to collecting apron
6	0.42	–0.60	3	connected to collecting apron but was not connected in experiment 9
7	0.58	–0.70	6	connected to collecting apron
9	0.48	–0.02	4	connected
	0.90	–0.20	5	connected
	--	--	3 and 4	these were not linked because of hole at x=0.52 m and y=0.40 m
11–30	--	--	--	velocity measurements–see table 16

Table 14. Observations of runoff from north-facing plots during the rising limb of the hydrograph.—Continued

[ponding, standing water covering an area greater than about 0.03 m in diameter; the locations of ponding are a rough guide because flow paths were not straight; ~, approximate; --, no data; m, meter; min, minutes; times indicate when observations were made, not necessarily when the observed phenomena took place]

Elapsed time (min)	Location		Flow path	Observation
	x(m)	y(m)		
			Experiment 11; October 8, 2004; Plot N15	
0	--	--	--	some mold on surface; plot had been covered with tarp
1	--	--	--	surface appeared to be more day than N13; some leaves collecting water
3	0.60	–0.60	1	connected
8	--	--	--	not much connection except near collecting apron
13	0.18	–0.38	2U	ponding
16	0.48	–0.78	2L	ponding and connected to collecting apron
20	0.28	–0.78	2L	connected to collecting apron
23	0.28	–0.68	2L	connected to 2L
24	--	--	--	flow has not established well enough to measure velocity because it would be hard to see when dye arrive
28	0.58	–0.53	--	area is connected between bones
			Experiment 12; October 8, 2004; Plot N15	
~2	0.40	–0.90	1 and 2L	both flow paths are contributing
~7	0.60	–0.58	1	is connected
	0.00	–0.90	--	entire area is wet
~9	0.00	–0.20	--	entire area is contributing
~12	--	--	--	about 50 percent of plot is ponded; area around skeleton and other higher areas are not ponded; uphill from skeleton is not ponded but wet
~13–25	--	--	--	velocity measurements–see table 16
			Experiment 13; October 9, 2004; Plot N15	
2	0.10	–0.1	2U	ponded
6	--	--	2 and 3	both flow paths are connected
8	--	--	1 and 5	both are active
14	--	--	--	entire lower part of plot is ponded
16	--	--	--	ridges are wet but not ponded
12–25	--	--	--	velocity measurements–see table 16
			Experiment 14; October 9, 2004; Plot N13	
2	--	–0.30	All	ponded
3–5	--	--	1 and 2	connected
6	--	--	3	connected
	--	--	6	connected
	0.68	–0.70	--	this area behaved differently than on October 8, 2004; split and went toward flow path 3
	--	--	5	connected
7	--	--	4	connect to flow path 5 and 6 (on October 8, 2004, flow path 4 was not connected to flow path 6
10–18	--	--	--	velocity measurements–see table 16
18	--	--	--	float in water tank stopped pump

Table 15. Observations of runoff from south-facing plots during the rising limb of the hydrograph.

[ponding, standing water covering an area greater than about 0.03 m in diameter; the locations of ponding are a rough guide because flow paths were not straight; ~, approximate; --, no data; m, meter; min, minutes; times indicate when observations were made, not necessarily when the observed phenomena took place]

Elapsed time (min)	Location				Flow path	Observation
	x(m)		y(m)			
Experiment 5; September 8, 2004; Plot S13						
7	0.1	0.2	–0.90	–1.00	1	ponded at the bottom and connected to collecting apron
	0.1	0.2	–0.55	–1.00	1	connected
	0.4	0.5	–0.30	–0.50	3	not connected but dye infiltrated at end of flow path
7–15	0.1	0.2	–0.30	–1.00	1	connect from lip of apron up to fungus; faster below y= -0.55 m
	0.6	0.7	–0.15	–0.70	2	not connected to apron; dye infiltrated at end of flow path
16–25	--	--	--	--	--	velocity measurements–see table 16
Experiment 6; September 8, 2004; Plot S15						
5	0.80	0.90	–0.50	–1.00	6	connected
7	0.40	0.50	–0.40	–0.50	4	connected but infiltrated at the end of flow path
8	0.60	0.70	–0.50	–1.00	5	infiltrated before reaching lip of collecting apron
10	0.90	1.00	–0.15	–1.00	6	connected to collecting apron
11.5	0.60	0.70	–0.50	–1.00	5	connected to collecting apron
12	0.02	0.05	–0.80	–0.90	7	connected into pond at end of flow path 1
15	0.10	0.20	–0.15	–0.50	2	connected to flow path 1
16	0.10	0.20	–0.05	–1.00	1	connected to collecting apron
17	0.30	0.40	–0.20	–1.00	3	connected to collecting apron
18–25	--	--	--	--	--	velocity measurements–see table 16
Experiment 7; September 9, 2004; Plot S15						
1	0.10	0.20	–0.05	–1.00	1	a bit moist
3	0.10	0.20	–0.20	–0.60	2	ponding
	0.60	0.70	–0.50	–1.00	5	ponding
	0.90	1.00	–0.15	–1.00	6	ponding
6	0.10	0.20	–0.20	–0.60	2	connected to 1 but neither 1 or 2 was connected to collecting apron
7.5	0.90	1.00	–0.40	–1.00	6	connected to collecting apron
10	0.10	0.20	–0.20	–0.40	2	this part connected but not to lower part of flow path
11	0.10	0.20	–0.80	–1.00	1	ponding at the base of this flow path connected to collecting apron
12	0.60	0.70	–0.50	–1.00	5	connected to collecting apron
	0.90	1.00	–0.10	–0.30	6	connected but moving slowly
13–28	--	--	--	--	--	velocity measurements–see table 16
29	0.30	0.40	–0.20	–1.00	3	ponded but discontinuous
Experiment 8; September 9, 2004; Plot S13						
2.5	--	--	--	--	--	no ponding but areas with rocks and fungus were getting wet faster
5	0.1	0.2	–0.90	–1.00	1	ponding started
7	0.1	0.2	–0.90	–1.00	1	ponded water was not connected to collecting apron (dye test)
11	0.6	0.7	–0.15	–0.70	2	not ponded and never ponded
17	0.1	0.2	–0.20	–0.50	1	slightly ponded but no connection with bottom
	0.1	0.2	–0.80	–0.90	1	pond has not reached lip of collecting apron
18–30						no velocity measurements because there was no observed runoff

Table 16. Flow velocities at selected locations during the steady-state discharge phase of the rainfall simulation experiments.

[m, meters; s, seconds; min, minutes; flow paths and shown in figures 14–17; width of flow paths were estimated to be 0.01 meter and flow depths were estimated to be 2 millimeters; these estimateds were used to estimate the discharge; SUM, is the sum of each average of measurements for separate flow paths; ~, approximate]

North plots			
Elapsed time (min)	**Flow path**	**Velocity (m/s)**	**Estimated discharge (L/min)**
Experiment 9; October 8, 2004; Plot N13			
~16–30	1	0.019	0.02
~16–30	2	0.034	0.04
~16–30	5	0.014	0.02
~16–30	1	0.022	0.03
SUM			0.08
Measured total			0.08
Experiment 10; October 8, 2004; Plot N13			
~10–30	1	0.014	0.02
~10–30	2	0.020	0.02
~10–30	5	0.023	0.03
~10–30	5	0.019	0.02
SUM			0.07
Measured total			0.24
Experiment 11; October 8, 2004; Plot N15			
flow not well established so dye could not be seen and no velocity measurements were made			
~13–25	2	0.015	0.02
~13–25	3	0.015	0.02
SUM			0.04
Measured total			0.18
Experiment 13; October 9, 2004; Plot N15			
12	2U	0.019	0.02
13	3	0.023	0.03
19	5	0.024	0.03
20	3	0.014	0.02
23	2L	0.042	0.05
24	2U	0.020	0.02
25	5	0.025	0.03
26	3	0.032	0.04
SUM			0.09
Measured total			0.38
Experiment 14; October 9, 2004; Plot N13			
10	1 and 2	0.064	0.08
12	1	0.016	0.02
18	2	0.038	0.05
SUM			0.08
Measured total			0.46

South plots			
Elapsed time (min)	**Flow path**	**Velocity (m/s)**	**Estimated discharge (L/min)**
Experiment 5; September 8, 2004; Plot S13			
~16–25	2	0.033	0.04
~16–25	2	0.050	0.06
~16–25	1	0.010	0.01
~16–25	1	0.042	0.05
SUM			0.08
Measured total			0.14
Experiment 6; September 8, 2004; Plot S13			
~17–25	1	0.020	0.02
~17–25	6	0.030	0.04
~17–25	5	0.025	0.03
~17–25	5	0.029	0.03
~17–25	1	0.026	0.03
~17–25	1	0.016	0.02
~17–25	**1**	**0.046**	**0.06**
~17–25	4	0.020	0.02
~17–25	4	0.070	0.08
SUM			0.15
Measured total			0.12
Experiment 7; September 9, 2004; Plot S15			
~12–28	1	0.003	0.003
~12–28	1	0.003	0.003
~12–28	6	0.021	0.03
~12–28	**5**	**0.005**	**0.01**
~12–28	1	0.007	0.01
SUM			0.04
Measured total			0.02
Experiment 8; September 9, 2004; Plot S13			
no observed discharge			

(0.020 and 0.15 L/min, table 13). For the medium and highest rainfall intensities, the flow-path discharges ranged from 11 to 57 percent of the measured discharge (except for experiment 6 where it was 129 percent). Thus, the contribution by the flow-path network does not provide enough discharge (except for low rainfall intensities) and water must flow from either the surface of the ash or along the ash/soil interface. Alternatively, the flow-estimation procedure is too crude and leads to underestimates of flow at higher discharge.

Suspended Sediment

Suspended sediment was collected only from experiments in the north-facing study area. Most of the material was very fine sand (0.063–0.125 mm) and silt and clay-sized particles (<0.063 mm, some of which were probably ash). Total concentrations ranged from 104 to 934 mg/L and were weakly correlated (fig. 27) with the measured discharge from the plots. Bedload sediment was not collected during the experiments.

Summary

Multiple rainfall intensities were used in rainfall-simulation experiments designed to investigate the infiltration and runoff from 1-m^2 plots on burned hillslopes covered by an ash layer of varying thickness. The 1-m^2 plots were on north- and south-facing hillslopes in an area burned by the Overland fire northwest of Boulder on the Front Range of Colorado.

The rainfall simulator was a nozzle-type system with a single nozzle. Different nozzles were used to produce different rainfall intensities and kinetic energies. The simulated rain was tested using a two-dimensional video disdrometer and differed from natural rain. The mean drop diameter was less than 2 mm, and drops were closer to a spheroidal shape than the oblate spheroidal shape observed for natural raindrops with diameters greater than 2 mm. Wide-angle, single-cone nozzles used in these experiments produced more spatially uniform rainfall intensity than regular single-cone nozzles. More variation was present in the upslope-downslope direction than in the cross-slope direction. The simulated rainfall did not have any significant temporal trends, but short-term temporal variability (change of rainfall with time) was about 2.3 mm/h/min and the greatest long-term (rain-gage array) variability was 0.31 mm/h/min. Measured rainfall intensities were greater than were predicted by calculations made using data from the nozzle manufacturer. However, the unit rainfall energy of the simulated rain was less than was predicted by empirical equations developed for rainfall in other settings. Two-dimensional video disdrometers were useful in examining drop characteristics but also have limitations when used to measure the characteristics of simulated rain. This instrument has a large error associated with small raindrops (less than 1 mm), which are typical of simulated raindrops produced by commercial full-cone nozzles.

The north- and south-facing study areas had bedrock outcrops (11 percent on the north and 31 percent on the south) on the upper slopes and soil on the lower slopes. Upper and lower slopes were covered by a nearly uniform layer of ash

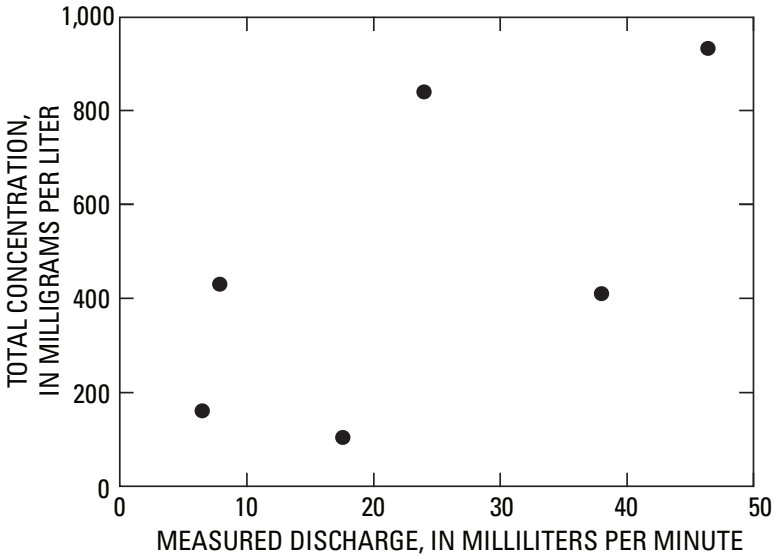

Figure 27. Correlation plot of total suspended-sediment concentration relative to measured discharge from the approximately 1-square meter plots.

(14 and 15 mm on the north and 10 and 15 mm on the south). The ash covering the experimental plots was thicker and finer grained (D_{50} = 0.30–0.40 mm) in the north-facing study area than in the south-facing study area (D_{50} = 0.75–1.50 mm). The bulk density of this ash was less than the density of water, but the particle density of the ash increased with decrease in particle size and ranged from 1,700 to 2,400 kg/m^3. This trend may reflect the inclusion of eolian transport of mineral material during and after a wildfire. The litter and duff layer remaining after the fire was thicker in the north-facing study area (32–37 mm) than in the south-facing study area (10 mm). The surface soil also was finer in the north-facing study area (D_{50} = 0.46–0.88 mm) than in the south-facing study area (D_{50} = 0.74–1.02 mm), and similar median diameters were measured within the plots for the underlying soil. The similarity of the particle size of the ash and the soil may reflect the interrelation between soils and vegetation on north- and south-facing slopes.

Infiltration rates were measured for several steady rainfall intensities ranging from 18 to 51 mm/h, which are typical of natural rainfall intensities. The steady-state infiltration rates were similar to the lowest infiltration rates measured by other studies in burned and unburned areas. All the measurements combined represent a relatively narrow range on infiltration rates (mostly 10–100 mm/h). One hypothesis for the lower values that we measured was the presence of a relatively intact and continuous layer of ash. However, infiltration rates were not inversely correlated with average ash thickness but probably depend on the rainfall intensity and the spatial variability of the ash, specifically the small areas with no ash that are superimposed on the major flow paths. For the low rainfall intensities (20–25 mm/h), little (0.020–0.065 L/min) or no discharge was observed, which suggests that all the rainfall infiltrated and the 20 mm/h may be a rainfall intensity threshold for these natural field conditions.

The theoretical flow-path characteristics were similar among the four experimental plots. Theoretically, each plot developed a 6th-order drainage network, but runoff was observed in only 2–4 of the flow paths during the rainfall simulation experiments. Initially, the runoff was unsteady and increased to a steady state within 7–26 minutes depending upon the antecedent soil moisture and rainfall intensities.

Table 17. Suspended-sediment concentration during steady-state discharge from north-facing plots.

[mm, millimeters; h, hours; L, liters; min, minutes; mg, milligrams; <, less than; >, greater than]

Elapsed time (min)	Incident rainfall intensity (mm/h)	Measured discharge (L/min)	Percentage of total sample in each size class							Total concentration (mg/L	Suspended-sediment discharge (mg/min)
			>2 mm	2–1 mm	1–0.500 mm	0.500–0.250 mm	0.250–0.125 mm	0.125–0.063 mm	<0.063 mm		
Experiment 9; October 8, 2004; Plot N13											
10–19	24	0.079	0	2.1	1.6	3.2	26.4	41.2	25.6	431	34
Experiment 10; October 8, 2004; Plot N13											
12–14	38	0.240	0.7	0.41	6.6	14.3	13.1	12.0	53.0	841	202
Experiment 11; October 8, 2004; Plot N15											
13–22	20	0.065	0.8	0.8	3.1	4.6	16.2	36.4	38.1	161	10
Experiment 12; October 8, 2004; Plot N15											
13–16	41	0.176	2.4	1.2	1.2	9.7	21.7	4.8	59	104	18
Experiment 13; October 9, 2004; Plot N15											
14–15	47	0.380	4.9	2.3	3.5	4.3	5.2	4.1	75.7	411	156
Experiment 14; October 9, 2004; Plot N13											
14–15	45	0.464	3.3	4.6	4.5	18.5	17.2	20.8	31.0	934	433

Acknowledgments

Many people contributed to this work. Deborah Martin helped in the field and initiated many interesting discussions. Wahab Sadeqi helped with field and laboratory work, and both he and Jennifer Schankel verified the data in this report. Dick Martin assisted us in putting together the pumping system and with other experimental equipment. Kyoko Ikeda trained us to use the 2DVD disdrometer and processed the raw disdrometer data for us. John Elliott made many helpful suggestions on developing the rainfall simulator. Thanks also to Ed Brandes for approving our use of this disdrometer, Jonathan Godt for conversations on capillary barriers, Robert Stallard for making available his spline program, Eric Schroder of the USDA Forest Service for helping set up our field work, and Sue Cannon for her guidance. Funding for David Kinner's work was provided by a USGS Mendenhall post-doctoral fellowship, the Central Region Geologic Hazards Team, and the Landslide Hazards Program Wildfire and Debris Flow Project.

References

Atlas, David, Srivastava, R.C., and Sekhon, R.S., 1973, Doppler characteristics of precipitation at vertical incidence: Reviews in Geophysics and Space Physics, v. 11, p. 1–35.

Bates, C.G., 1923, Physiological requirements of Rocky Mountain trees: Journal of Agricultural Research, v. 24, no. 2, p. 97–164.

Bates, C.G., 1924, Forest types in the central Rocky Mountains as affected by climate and soil: U.S. Department of Agriculture Bulletin no. 1233, 151 p.

Benavides-Solorio, J., and MacDonald, L.H., 2001, Post-fire runoff and erosion from simulated rainfall on small plots, Colorado Front Range: Hydrological Processes, v. 15, p. 2931–2952.

Betson, R.P., 1964, What is watershed runoff?: Journal of Geophysical Research, v. 69, no. 8, p. 1541–1552.

Birkeland, P.W., Shroba, R.R., Burns, S.F., Price, A.B., and Tonkin, P.J., 2003, Soils and geomorphology in mountains —An example from the Front Range of Colorado: Geomorphology, v. 55, p. 329–344.

Bolin, S.B., and Ward, T.J., 1987, Recovery of a New Mexico drainage basin from a forest fire: Forest Hydrology and Watershed Management, Proceedings of the Vancouver Symposium, IAHS Publication no. 167, p. 191–198.

Brandt, T.R., Moore, D.W., and Murray, K.E., 2003, A spatial database of bedding attitudes to accompany geologic map of the Boulder–Fort Collins–Greeley area, Colorado, by Roger B. Colton: U.S. Geological Survey Open-File Report 2003–24, *http://pubs.usgs.gov/of/2003/ofr-03-024/ofr-03-024_508v1.1.pdf*

Brigini, V.N., Chandrasekar, V., Hubbert, J., Gorgucci, E., Randeau, W.L., and Schoenhuber, M., 2003, Raindrop size distribution in different climatic regimes from disdrometer and dual-polarized radar analysis: Journal of Atmospheric Sciences, v. 60, p. 354–365.

Brown, L.C., and Foster, G.R., 1987, Storm erosivity using idealized intensity distributions: Transactions of the American Society of Agricultural Engineers, v. 30, p. 379–386.

Cannon, S.H., 2001, Debris-flow generation from recently burned watersheds: Environmental and Engineering Geoscience, v. 7, no. 4, p. 321–341.

Cannon, S.H., and Gartner, G.E., 2005, Wildfire-related debris flow from a hazards perspective: Chapter 15, *in* Hungr, O., and Jacob, M., eds., Debris flow hazards and related phenomena: Springer-Praxis Books in Geophysical Sciences, p. 321–344.

Cannon, S.H., Gartner, J.E., Rupert, M.G., and Michael, J.A., 2003, Emergency assessment of debris flow hazards from basins burned by the Grand Prix and Old Fires of 2003, Southern California: U.S. Geological Survey Open-File Report 2003–0475.

Cerdà, Artemi, 1998, Post-fire dynamics of erosional processes under Mediterranean climatic conditions: Zeitschrift für Geomorphologie Neue Folge, v. 42, no. 3, p. 373–398.

Cerdà, Artemi, Ibáñez, S., and Calvo, A., 1997, Design and operation of a small and portable rainfall simulator for rugged terrain: Soil Technology, v. 11, p. 163–170.

de Lima, J.L.M.P., Torfs, P.J.J.F., and Singh,V.P., 2002, A mathematical model for evaluating the effect of wind on downward-spraying rainfall simulators: Catena, v. 46, no. 4, p. 221–241.

Doerr, Stefan, Ferreira, A.J.D., Walsh, R.P.D., Shakesby, R.A., Leighton-Boyce, G., and Coelho, C.O.A., 2003, Soil water repellency as a potential parameter in rainfall runoff modeling Experimental evidence at point to catchment scales from Portugal: Hydrological Processes, v. 17, p. 363–377.

Dunne, Thomas, and Dietrich, W.E., 1980, Experimental study of Horton overland flow on tropical hillslopes: Zeitschrift für Geomorphologie Neue Folge, Supplementbaende, v. 3, p. 40–89.

Dunne, Thomas, Zhang, W., and Aubry, B.F., 1991, Effects of rainfall, vegetation and microtopography on infiltration and runoff: Water Resources Research, v. 27, no. 9, p. 2271–2285.

Eaton, E.C., 1935, Flood and erosion control problems and their solution: American Society of Civil Engineers Transactions, paper number 1950, v. 101, p. 1302–1362.

Emmett, W.E., 1970, The hydraulics of overland flow on hillslopes: U.S. Geological Survey Professional Paper 662–A, 68 p.

Esteves, Michel, Planchon, O., Lapetite J.M., Silvera, N., and Cadet, P., 2000, The 'EMIRE' large rainfall simulator—Design and field testing: Earth Surface Processes and Landforms, v. 25, p. 681–690.

Garbrecht, Jurgen, and Martz, L.W., 1997, The assignment of drainage directions over flat surfaces in raster digital elevation models: Journal of Hydrology, v. 193, no. 1–4, p. 204–213.

Gardner, W.H., 1986, Water content, *chap. 2 of* Klute, Arnold, Methods of Soil Analysis, Part 1, Physical and mineralogical methods: American Society of Agronomy, Inc., and Soil Science Society of America, Inc., Madison, Wisconsin, p. 493–544.

Gunn, Ross, and Kinzer, G., 1949, The terminal velocity of fall for water droplets in stagnant air: Journal of Meteorology v. 6, p. 243–248.

Guy, H. P., 1969, Laboratory theory and methods for sediment analysis: U.S. Geological Survey Techniques of Water-Resources Investigations, book 5, chap. C1, 58 p.

Håkanson, Lars, and Jansson, Mats, 1983, Principles of lake sedimentology: New York, Springer-Verlag, 316 p.

Helvey, J.D., 1980, Effects of a north central Washington wildfire on runoff and sediment production: Water Resources Bulletin, v. 16, n. 4, p. 627–634.

Imeson, A.C., Verstraten, J.M., van Mulligen, E.J., and Sevink, J., 1992, The effects of fire and water repellency on infiltration and runoff under Mediterranean type forest: Catena, v. 19, p. 345–361.

Jenson, S.K., and Domingue, J.O., 1988, Extracting topographic structure from digital elevation data for geographic-information system analysis: Photogrammetric Engineering and Remote Sensing, v. 54, no. 11, p. 1593–1600.

Kamphorst, A., 1987, A small rainfall simulator for the determination of soil erodibilty: Netherlands Journal of Agricultural Science, v. 35, p. 407–415.

Krammes, J.S., and Rice, R.M., 1963, Effect of fire on the San Dimas Experimental Forest: Arizona Watershed Symposium, Phoenix, Sept.18, 1963, Proceedings of the 7th Annual Meeting: Phoenix, Arizona Water Commission, p. 31–34.

Kruger, Anton, and Krajewski, W.F., 2002, Two-dimensional video disdrometer—A description: Journal of Atmospheric and Oceanic Technology, v. 19, p. 602–617.

Krumbein, W.C., 1934, Size frequency distributions of sediments: Journal of Sedimentary Petrology, v. 4, p. 65–77.

Kunze, M.D., and Stednick, J.D., 2006, Streamflow and sediment yield following the 2000 Bobcat Fire, Colorado: Hydrologic Processes, v. 208, p. 1661–1681.

Laschelles, Bruce, Favis-Mortlock, D.T., Parsons, A.J., and Guerra, A.J.T., 2000, Spatial and temporal variation in two rainfall simulators—Implications for spatially explicit rainfall experiments: Earth Surface Processes and Landforms, v. 25, p. 709–721.

Laws, O.J., 1941, Measurements of the fall-velocities of water-drops and raindrops: Transactions of the American Geophysics Union, v. 22, p. 709–721.

Lu, Ning, and Likos, W.J., 2004, Unsaturated soil mechanics: Hoboken, N.J., John Wiley and Sons, 556 p.

Martin, D.A., and Moody, J.A., 2001, Comparison of soil infiltration rates in burned and unburned mountainous watersheds: Hydrological Processes, v. 15, no. 15, p. 2893–2903.

McQueen, I.S., 1963, Development of a hand portable rainfall-simulator infiltrometer: U.S. Geological Survey Circular 482, 16 p.

Meyer, L.D., and Harmon, C., 1979, Multiple intensity rainfall simulator for erosion research on row side slope: Transactions of the American Society of Agricultural Engineers, v. 22, p. 100–103.

Moody, J.A., and Kinner, D.A., 2006, Spatial structure of stream and hillslope drainage structures following gully erosion after wildfire: Earth Surface Processes and Landforms, v. 31, 319–337.

Moody, J.A., and Martin, D.A., 2001a, Post-fire, rainfall intensity-peak discharge relations for three mountainous watersheds in the western USA: Hydrological Processes, v. 15, no. 15, p. 2981–2993.

Moody, J.A., and Martin, D.A., 2001b, Initial hydrologic and geomorphic response following a wildfire in the Colorado Front Range: Earth Surface Processes and Landforms v. 26, p. 1049–1070.

Morel-Seytoux, H.J., 1986, Influence of variability in hydraulic conductivity on hillslope infiltration, *in* Morel-Seytoux, H.J., and Warner, J.W., Proceedings of Sixth Annual AGU Front Range Branch Hydrology Days, April 15–17, 1986: Fort Collins, Colorado State University, Hydrology Days Publications, p. 153–170.

Mutchler, C.K., and Hermsmeier, L.F., 1965, Review of rainfall simulators: Transactions of the American Society of Agricultural Engineers, v. 9, p. 67–68.

Neary, D.G., Klopatek, C.C., DeBano, L.F., and Ffolliott, P.F., 1999, Fire effects on below ground sustainability—A review and synthesis: Forest Ecology and Management, v. 122, p. 51–71.

Niebling, W.H., Foster, G.R., Natterman, R.A., Nowlin, J.D., and Holbert, P.V., 1981, Laboratory and field testing of a programmable plot-sized rainfall simulator, *in* Erosion and Sediment Transport Measurement: IAHS Publication, no. 133, p. 405–414.

Paige, G.B., Stone, J.J., Smith, J.R., and Kennedy, J.R., 2003, The Walnut-Gulch rainfall simulator: a computer controlled variable intensity rainfall simulator: Applied Engineering in Agriculture, v. 20, no. 1, p. 25–31.

Parrett, Charles, 1987, Fire-related debris flows in the Beaver Creek drainage, Lewis and Clark County, Montana: U.S. Geological Survey Water-Supply Paper 2330, p. 57–67.

Parrett, Charles, Cannon, S.H., and Pierce, K.L., 2003, Wildfire-related floods and debris flows in Montana in 2001: U.S. Geological Survey Water-Resources Investigations Report 2003–4319, 22 p.

Pierson, F.B., Robichaud, P.R., and Spaeth, K.E., 2001, Spatial and temporal effects of wildfire on the hydrology of a steep rangeland watershed: Hydrological Processes, v. 15, p. 2905–2916.

Pruppacher, H.R., and Beard, K.V., 1970, A wind tunnel investigation of the internal circulation and shape of water drops falling at terminal velocity in air: Quarterly Journal of the Royal Meteorological Society, v. 96, p. 247–256.

Reid, E.H., and Love, L.D., 1951, Range-watershed conditions and recommendations for management, Elk Ridge and Lower Elk Ridge cattle allotments, Roosevelt National Forest, Colorado: U.S. Forest Service, Washington, D.C., 122 p.

Rivix LLC, 2001, RiverTools user's guide release, 2001: Boulder, Colorado, Research Systems, Inc., 202 p.

Robichaud, P.R., 2000, Fire effects on infiltration rates after prescribed fire in Northern Rocky Mountain forests, USA: Journal of Hydrology, v. 231–232, p. 220–229.

Römkens, M.J.M., Prasad, S.N., and Whisler, F.D., 1990, Surface sealing and infiltration, chapter 5 of Anderson, M.G., and Burt, T.P., eds., Process studies in hillslope hydrology: New York, John Wiley & Sons Ltd., p. 127–172.

Ross, Benjamin, 1990, The diversion capacity of capillary barriers: Water Resources Research, v. 26, no. 10, p. 2625–2629.

Rowe, P.B., 1948, Influence of woodland chaparral on water and soil in central California: Sacramento, California State Board of Forestry, 70 p.

Smith, R.E., and Goodrich, D.C., 2000, Model for rainfall excess patterns on randomly heterogeneous areas: Journal of Hydrologic Engineering, v. 5, p. 355–362.

Spraying Systems Company, 2005, Full Cone Nozzles, Catalog 60B Express, accessed July 6, 2005, at *http://service.spray.com/catalog/pdfmet/catalog60B/toc.pdf*

Sumner, M.E., and Stewart, B.A., eds., 1992, Soil Crusting—Chemical and physical processes: Boca Raton, Fla., CRC Press, Inc., 367 p.

Veenhuis, J.E., 2002, Effects of wildfire on the hydrology of Capulin and Rito de los Frijoles Canyons, Bandelier National Monument, New Mexico: U.S. Geological Survey Water-Resources Investigations Report 2002–4152, 39 p.

Ward, T.J., and Bolton, S.M., 1991, Hydrologic parameters for selected soils in Arizona and New Mexico determined by rainfall simulation—Technical completion report: Las Cruces, New Mexico Water Resources Institute, 79 p.

Wilcox, B.R., Wood, M.K., and Tromble, J.T., 1986, A hand portable single nozzle rainfall simulator designed for use on steep slopes: Journal of Range Management, v. 39, no. 4, p. 375–377.

Wohl, E.E., and Pearthtree, P.P., 1991, Debris flows as geomorphic agents in the Huachuca Mountains of southeastern Arizona: Geomorphology, v. 4, p. 273–292.